CRYSTALLIZATION ONSET AND POLYMORPHIC OCCURRENCE IN PURE SATURATED TRIACYLGLYCEROLS DURING COOLING FROM THE MELT

by

Xinyue Zhang

Submitted in partial fulfilment of the requirements
for the degree of Master of Science

at

Dalhousie University
Halifax, Nova Scotia
May 2023

TABLE OF CONTENTS

LIST OF TABLES

LIST OF FIGURES

ABSTRACT

The effect of cooling rate on crystallization onset temperature and polymorphic occurrence in four pure saturated triacylglycerols, tridodecanoate (LLL), trimyristate (MMM), tripalmitate (PPP) and tristearate (SSS) has been studied using differential scanning calorimetry (DSC), and X-ray diffraction under constant cooling rates.

In this study, differential scanning calorimetry (DSC) experiments were conducted to detect the crystallization onset temperatures under 9 different cooling rates between 2.5 C° /min and 25 C° /min in a random sequence. A MATLAB program was developed to automatically process the bulky DSC data files and calculate the onset, which is the first point that deviated from the heat flow baseline. Time-resolved small and wide-angle X-ray diffraction (SAXD, WAXD) measurements at a synchrotron allowed the identification of polymorphic forms at the onset temperature. X-ray data were fitted to a Voigt distribution to calculate mass fractions α and β'.

By analyzing an abundance of DSC thermograms, a first onset of crystallization was observed above the melting point of the α polymorph under 1-15 C° /min for LLL and 1-5 C° /min for MMM. Double peaks were observed in the DSC exotherms of LLL and MMM under slow cooling rates. As evidenced by the X-ray data, the β' polymorph crystallized first, followed by the second peak, corresponding to the formation of the α polymorph. However, this phenomenon was not observed at high cooling rates.

The second onset (α onset) of the heat flow signal was identified by fitting an extended Avrami (Weibull) model to the thermograms. A MATALB program was developed to process the data from the first onset until the end of the crystallization. The values of the eight parameters of the extended Avrami model were obtained for the 162 thermograms.

LIST OF ABBREVIATIONS AND SYMBOLS USED

Cp	specific heat capacity at a constant pressure (J/g C°)
CNPs	crystal nanoplatelets
DCL	double chain-length
DSC	differential scanning calorimetry
FA	fatty acid
FWHM	full width at half maximum
G	Gibbs energy (J or J/mol)
LLL	trilaurin
MMM	trimyristin
MDSC	modulated differential scanning calorimetry
PPP	tripalmitin
S	entropy (J/K or J/Kmol)
SAXD	small angle X-ray diffraction
SR-XRD	synchrotron radiation XRD
SSS	tristearin

TAGs	triglycerides
TCL	triple chain-length
WAXD	wide angle X-ray diffraction
XRD	X-ray diffraction
$\Delta\mu$	chemical potential
ΔH_m	melting enthalpy (J/mol)
T_m	melting temperature (˚C)
ΔG_v	phase transformation free energy change
ΔG_s	surface formation free energy change
ΔG_{hom}	the Gibbs free energy of homogeneous nucleation
S_e	surface area
γ	interfacial tension
r_c	critical nucleus size
D_{hom}^*	number density of the critical size clusters
k_b	Boltzmann constant (=$1.38*10^{-23}$J/K)

J_{hom}	nucleation rate
N_A	Avogadro constant (= $6.022*10^{23}$/mol)
$\dot{q}$	heat flow
λ	wavelength
ν	frequency
c	light speed
d	spacing between crystal lattice planes
θ	angle of incidence of the X-ray beam
CR	Cooling rate (C˚/min)

ACKNOWLEDGEMENTS

My sincere and hearty thanks and appreciations go firstly to my supervisor, Dr. Gianfranco Mazzanti, whose suggestions and encouragement have given me much insight into my studies. Studying under his guidance and supervision has been a great privilege and joy. Furthermore, I am honoured to benefit from his personality and diligence, which I will treasure my whole life.

I would also like to extend my thanks to Dr. Yim and Dr. Rousseau for their support with the experiments, which were critical to this research, and I am deeply appreciative of their assistance. I also want to thank my committee, Dr. Budge and Dr. Rousseau, for their guidance and assistance.

My research colleagues, Omar Al-Qatami, who work with me give me substantial support and help me in study and research. And also other former members of Dr.Mazzanti research group, this work would not have been finished without your previous efforts.

My deepest thanks are expressed to my parents, who gave me much encouragement and financial support respectively and for their endless love for me. My parents have made all the wonderful things happen in my life. Words cannot express how much I love you both.

CHAPTER 1. INTRODUCTION

1.1 Hypothesis and Objectives

Crystallization occurs in many fat-rich products, such as margarine and chocolate. During the initial processing stage of production, the relative rates of nucleation and growth determine the initial crystal size distribution, which determines the texture and other characteristics of the material. Isothermal crystallization has been extensively studied because the kinetic parameters dependent on temperature are fixed. Non-isothermal crystallization methods, however, provide information closer to the actual industrial processing, where the temperature changes with time, usually by following a cooling rate.

The use of thermal treatments, such as dynamic temperature variations or thermal thawing, greatly influences the crystallization and polymorphic transformation of lipids. Therefore, the occurrence of designed polymorphic forms may be controlled and monitored by tailoring the most efficient temperature programs. A very well-known case is the tempering of chocolate to obtain form V beta polymorph in cocoa butter.

Triacylglycerols are composed of fatty acids esterified onto a glycerol backbone. These triacylglycerols form lamellar structures which aggregate into nanoscopic size crystallites. Crystallites interact to form clusters. The clusters then form the fat crystal networks that provide macroscopic structure (Marangoni & Wesdorp, 2013).

To better understand the crystallization behaviour of triacylglycerols under non-isothermal conditions, the objectives of this thesis are:

1. Investigate the effect of cooling rate on the polymorphic type and onset temperature of pure saturated triacylglycerols (LLL, MMM, PPP, SSS)
2. Develop a method to detect the crystallization onset temperature for coexisting crystallization events (α, β' polymorphic forms).

In this method, it is assumed that LLL can crystallize in only two different polymorphic forms, with no presence of sub-modifications. The cooling process results in the nucleation and growth of β' crystals, which occurs at a rate that is dependent on the cooling temperature. As the temperature continues to decrease, the liquid material, with or without crystals, will eventually cross the melting point of α. At this point, there is a competition between the nucleation of β' and α in the remaining liquid. However, it eventually becomes more favorable to form α than β' from the remaining liquid, despite the fact that β' may act as a nucleation template.

CHAPTER 2. LITERATURE REVIEW

2.1 Lipids

Lipids are a group of organic compounds that include mostly fatty acids and sterols, and their derivatives. They are soluble in organic solvents. Triacylglycerols are composed of fatty acids esterified onto a glycerol backbone. Triacylglycerols do not interact appreciably with water, whereas polar lipids form hydrated structures. They are a significant source of cellular energy and function in living organisms. They also provide essential fatty-acid moieties that form the barrier separating the living cell from the outside world. Lipids are strongly associated to many diseases such as atherosclerosis and obesity. Lipids also play a vital role in pharmaceutical, cosmetics, and food industry. They are not only used for their nutritional value but also provide structural and organoleptic characteristics, which are important in processed food technology. (Small,1986). Fat and oils are a subgroup of lipids, and the terms are often used interchangeably. Oils are usually liquid at room temperature whereas fats are solid.

Triacylglycerols (TAGs) make up about 98% of most fats composition, while the remaining minor components are polar lipids such as phospholipids, glycolipids, sterols, diacylglycerols (DAG), monoacylglycerols (MAG), free fatty acids, and other trace ingredients (Bailey & Shahidi, 2005). From a nutritional point of view, triacylglycerols (often called triglycerides) are lipids of significant importance as they make up 95% of dietary fat (Barasi, 2003). In addition, there are fat-soluble micronutrients in the diet that must absorbed by the body tissues, thus they need the fat to be delivered. The physical properties of oils and fats are determined by the composition of triacylglycerols and

directly affect the texture, stability, flavor, aroma, and sensory and visual characteristics of foods (O'Brien, 2009).

Table 2-1 TAGs samples used in this research.

	Fatty Acid (FA)	Chain Length
LLL	lauric acid (dodecanoic acid)	12
MMM	myristic acid (tetradecanoic acid)	14
PPP	palmitic acid (hexadecanoic acid)	16
SSS	stearic acid (octadecanoic acid)	18

TAGs consist of three FAs esterified to a glycerol molecule. They can have multiple components with variations in FA chain length, branching, saturation, esterified positions of FAs, and the existence of double bonds (trans or cis). Different combinations of these FAs form different TAG molecular species, and the TAG molecular species composition of each oil is unique, forming complex TAG mixtures.

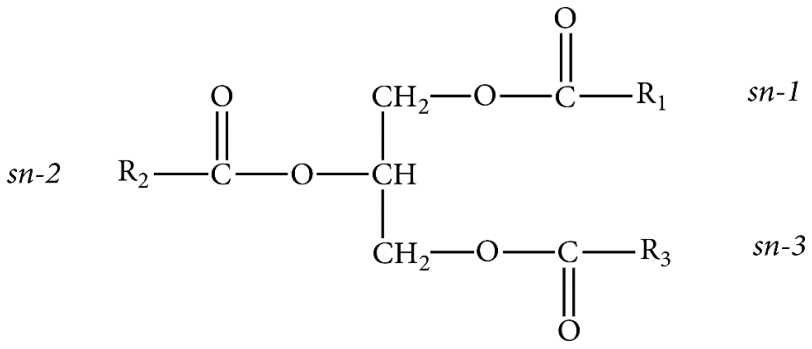

Figure 2-1 A general structure of saturated triacylglycerol molecules that are esterified by three fatty acids groups. The glycerol carbon atoms are stereospecifically numbered as sn-2 (center) and sn-1 and sn-3 (outer) (Zhang et al., 2018).

2.2 Crystallization

The understanding of crystallization of lipids is indispensable in the manufacture of products such as butter, chocolates, margarine, and shortenings. Pharmaceutical and cosmetics industries rely on crystallization of lipids to provide carrier structures for many of their products. Moreover, the study of fat crystallization contributes to the isolation of specific fat and lipid materials from animal and vegetable oil or fats (Sato, 2001). Controlling TAGs crystallization to get the desired polymorph and size distribution of the crystalline phase will lead to a desirable product quality. The crystallization behavior, including phase compositions, strongly depend upon heat and mass transfer conditions, which will ultimately affect mechanical strength, flow behavior, and sensory texture (Marangoni & Wesdorp, 2013).

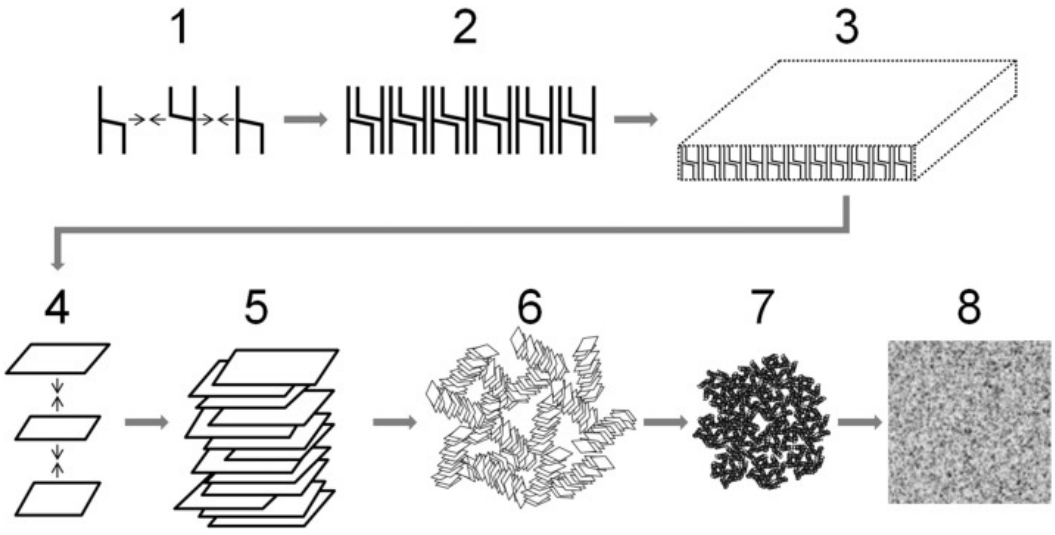

Figure 2-2 The structure hierarchy and the process of crystallization of TAG. Adapted from Marangoni and Wesdorp (2013).

Crystallization is a physical event that happens through nucleation and crystal growth. When the temperature decreasing until below the melting point of TAG, then the melt is under supersaturated condition. This also known as undercooling or supercooling,

represents the thermodynamic driving force for a change from liquid to solid (Marangoni & Wesdorp, 2013). This driving force accumulates to break the energy barrier for activating nucleation, molecules in the liquid state start to pack up to generate a stable crystal nucleus. After a stable nucleus is formed, the crystal starts the growth phase of crystallization. Additional units are rapidly integrated into the lattice, reducing the driving force of supersaturation. Unless kinetically constrained, this growth continues until the system reaches equilibrium, at which point the driving force for crystallization decreases to zero and the crystalline phase reaches its maximum volume (Hartel, 2013).

The structural hierarchy of a crystallized fat is shown in figure 1-2 and describes the microscopic procedure when the crystallization happens. The formation of stable cores is followed by orderly assembly into lamellae, after which the lamellae are combined to form crystal nanoplatelets (CNPs), and aggregated stacks of CNPs assemble randomly into crystallites, distinctive stable nano-sized crystallites develop different polymorphic forms according to the condition. During heat and mass transfer, these nanoscale crystallites aggregate into microstructural components, forming larger clusters until a macroscopic network of fat is formed.

2.2.1 Driving Force for Crystallization

There are two types of crystallizing systems in foods: from the melt and from a solution. Pure triacylglycerols (TAGs) are typical melt systems which have a constant melting point. Above this temperature, TAG is a liquid, and below it, TAG solidifies (Hartel, 2013). To create a driving force for crystallization, TAGs need to be cooled below the melting point, and the melt system becomes supersaturated, which is also known as

undercooling or supercooling under the melting point (Melin, 2005; Kashchiev, 2000; Kashchiev & van Rosmalen, 2003).

The fundamental thermodynamic driving force for the crystallization of a TAG in a mixture, TAG(i), is the difference in chemical potential of ($\Delta\mu_i$) between the liquid state (μ_i^L) and solid state (μ_i^S) (Himawan, 2006):

$$\Delta\mu_i = \mu_i^L - \mu_i^S \tag{2-1}$$

A driving force for crystallization is illustrated in Figure 2-3 (a) for liquids and (b) for solutions. T_m and T_s correspond to equilibrium conditions in the two phases. The liquid becomes supercooled when the temperature is reduced to T_c, and the solution phase becomes supersaturated.

In the case of fats composed of relatively similar components, crystallization can usually be considered as occurring in a pure melting system. Neglecting the differences in specific heat between liquid and solid, the driving force for crystallization can be expressed as a function of the degree of undercooling, thus

$$\Delta\mu_i = \frac{\Delta H_{mi}\Delta T}{T_{mi}} = \frac{\Delta H_{mi}(T_{mi} - T)}{T_{mi}} \tag{2-2}$$

Where ΔH_{mi} is the melting enthalpy (J/mol), T_{mi} is the melting temperature (K), and T is the onset temperature (K) of crystallization under isothermal conditions.

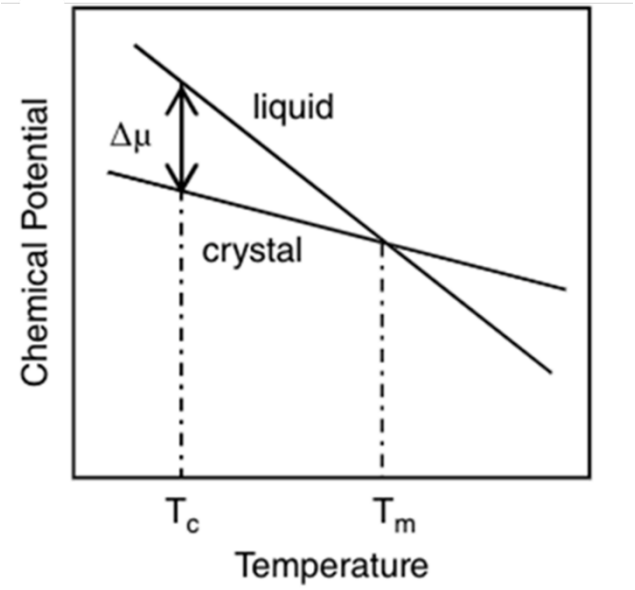

Figure 2-3 The driving force of Crystallization (Sato, 2018).

2.2.2 Nucleation

The nucleation process largely determines the crystal structure and size distribution in crystallization (Erdemir, 2009). When the system is below the melting point, a phase transition occurs in a part of the supercooled melt that is in a metastable state, resulting in the formation of nuclei (Hartel, 2001). After the crystal nucleus is formed, other molecules in the liquid layer in contact with it are continuously filled with supersaturated liquid around the crystal, causing it to grow continuously (Boistelle, 1988).

In the region a few degrees below the melting point, the molecules are in the metastable state and start to aggregate into small clusters. To form a stable nucleus, flexible molecules in the melt must adopt a specific conformation because the energy of interaction between the molecules is insufficient to overcome the Brownian effects

(Marangoni & Wesdorp, 2013). Undercooling increases as the temperature decreases, leading to the formation of stable nuclei of a critical size. As molecules assume lower energy states in the crystal lattice, a solid-liquid interface is created upon crystal formation, resulting in a positive contribution to the free energy of nucleation and a decrease in chemical potential differences. Embryos larger than the critical size continue to grow, while those smaller than the critical size may return to be separate liquid molecules (Hartel, 2001).

2.2.2.1 Nucleation Theories

The process of nucleation can occur in several different ways through primary and secondary mechanisms. Primary nucleation can occur either homogeneously or heterogeneously (Lacmann & Mayer, 1999; Hartel, 2001; Domingues, 2015; Mullin, 2001).

Homogeneous nucleation occurs when only biomolecular interactions between TAG molecules occur without the presence of any foreign particles. Homogeneous nucleation requires a fat that does not contain any solid substrate or contaminants. Usually, under high degrees of supercooling, which is about 30°C below the melting point, TAG molecules only interact with each other (Rogers, 2008).

Heterogeneous primary nucleation occurs when a foreign surface, such as molecules of different composition, reduce the free energy required for nucleation, resulting in much faster nucleation compared to homogeneous primary nucleation (Sato, 2018). Heterogeneous nucleation likely results from interactions between solid particles and supersaturated fluids, although the mechanisms are not fully understood. The ability of

external substances to catalyze nucleation is generally determined by the degree of lattice match between the solid surface and the nucleating species crystals. A higher lattice match increases the likelihood of surface-catalyzed heterogeneous nucleation. Additionally, it is interesting to note that heterogeneous nucleation sites have an aging effect on nucleation activity (Mullin, 2001). Multiple nucleation of material under the same conditions leads to the diffusion of nucleation ability. As a result, controlling lipid crystallization is challenging due to the variability of heterogeneous nucleation.

Although homogeneous nucleation theories can partially explain certain characteristics of nucleation kinetics, numerous studies have shown that nucleation in condensed systems is heterogeneous, with nuclei forming preferentially at certain interfaces (Turnbull, 1950). The existing crystals can be broken down into smaller stable nuclei due to secondary nucleation, which is the formation of a new nucleus in the presence of already-formed crystals (Lawler, 2008). This occurs when microscopic crystalline elements are detached from the surface of the crystal (Hartel, 2013; Lawler, 2008). Crystallization driving forces, which are supersaturation or supercooling, affect secondary nucleation, resulting in the formation of more stable nuclei at higher supersaturations. Certain circumstances can also result in it occurring under static conditions. The formation of secondary nuclei may occur in lipid systems due to the dissipation of heat and/or the concentration of species that are not crystallizing in certain regions of the lipid crystal. Some nucleation in emulsions is also influenced by secondary nucleation, as well as bulk solution seeding in some cases, such as when tempering chocolate. However, the exact mechanisms are unclear (Metin, 2001).

In classical nucleation theory, homogeneous primary nucleation occurs without external assistance of a crystal lattice. The formation of a stable nucleus requires the passage of a free-energy barrier. Based on the thermodynamic description by Gibbs in the 19th century, cluster formation requires a free energy change equal to the total of the phase transformation free energy change (ΔG_v) and the surface formation free energy change (ΔG_s) (Erdemir, 2009). Crystal surface free energy is always positive (ΔG_s) and related to the surface area (S_e) and interfacial tension (γ) between the crystal and the surrounding liquid. Surface free energy, ΔGs:

$$\Delta G_s = S_e \gamma \tag{2-7}$$

Volume free energy changes (ΔG_v) during phase transformation are negative since heat is released by transforming from the liquid state to the solid state and is proportional to volume (V_e) (Metin & Hartel, 2005).

Therefore, cluster growth depends on the competition between a decrease in ΔG_v and an increase in ΔG_s. At small radiuses, the positive surface free energy dominates, which leads to an increase in the total free energy change (Figure 2-3).

$$\Delta G_v = -\frac{\Delta H_{m,f} \Delta T}{T_f V_m} V_e \tag{2-8}$$

Where $\Delta H_{m,f}$ is the molar enthalpy of fusion, ΔT is the undercooling, V_m is the molar volume.

During nucleation, free energy reaches a maximum at the critical nucleus size (r_c), the minimum size for a stable nucleus (Figure 2-4). Clusters of molecules larger than this

critical size form stable nuclei that are able to irreversibly grow to large crystals, whereas clusters of molecules smaller than this critical size could decay into liquid.

The Gibbs free energy changes as a solid embryo form in the simple case of a pure substance and homogeneous nucleation in liquid can be address as

$$\Delta G_{hom} = \Delta G_v + \Delta G_s = -\frac{\Delta H_{m,f} \Delta T}{T_f V_m} V_e + \gamma S_e \tag{2-9}$$

Where V_e and S_e are the volume and surface, respectively, of the formed embryo.

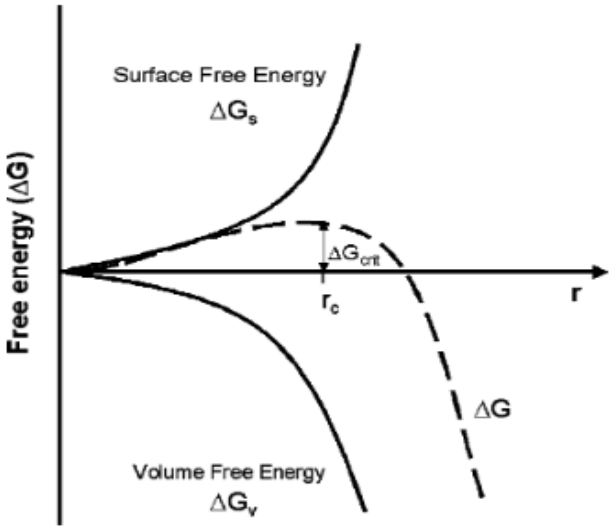

Figure 2-4 Free energy diagram for nucleation in classical nucleation theory (Erdemir, 2009) (Permission is granted).

Recent experimental and theoretical studies have shown that a two-step mechanism can be applied to both macromolecules and small organic molecules, suggesting that this mechanism accounts for the majority of crystallization from solutions (Erdemir, 2009). In the two-step model proposed, there is a prenucleation stage wherein clusters of sufficient size form first, then the cluster is reorganized into an ordered structure. This

also incorporates both monomeric and polymeric growth units during the transformation from clusters to crystal nuclei. (Kashchiev, 2000; Erdemir, 2009).

2.2.2.2 Nucleation Rate

As mentioned before, the Gibbs free energy of homogeneous nucleation, ΔG_{hom}, can be expressed as the sum of the decrease of free energy per unit volume related to the enthalpy of fusion, $-\Delta G_V$, and the increase of the total surface energy depends on interfacial energy and total surface of the crystal, ΔG_S. Assuming that the nuclei are spherical and substituting the radius (r) into the volume (V) and surface (S), the expression of the Gibbs energy can be written as:

$$\Delta G_{hom} = \frac{\Delta H_{m,f} \Delta T}{T_f V_m} V_e + \gamma S_e = \frac{4 \Delta H_{m,f} \Delta T \pi r^3}{3 T_f V_m} + 4\pi r^2 \gamma \tag{2-10}$$

When r reaches the critical size r^*, the Gibbs free energy ΔG_{hom} has reached maximum ΔG_{hom}^* At this point, the derivative $d\Delta G_{hom}/dr = 0$, thus

$$\frac{d\Delta G_{hom}}{dr} = 4\pi r^{*2} \Delta G_v + 8\pi r^* \gamma = 0 \tag{2-11}$$

Therefore

$$r^* = \frac{2\gamma}{\Delta G_v}$$

Substituted r* in the equation:

$$\Delta G^*_{hom} = \frac{16\pi\gamma^3}{3\Delta G_v^2} = \frac{16{T_f}^2{V_m}^2\pi\gamma^3}{3\Delta {H_{m,f}}^2\Delta T^2} \quad (2\text{-}12)$$

It is usually hypothesized that for a specific value of $\Delta\mu(=\Delta G_{hom})$, a cluster size distribution follows the Boltzmann distribution. Therefore, thus the number density of the critical size clusters (D_{hom}^*) can be expressed as:

$$D^*_{hom} = N_m e^{\frac{-\Delta G^*_{hom}}{k_b T}} \quad (2\text{-}13)$$

Where N_m the number of molecules per unit volume, and k_b is the Boltzmann constant ($=1.38\times10^{-23}$J/K).

Clusters can only form stable crystals above the critical size. Thus, the frequency of nucleus formation, which is the nucleation rate (J_{hom}), is proportional to the number density of the critical size clusters D_{hom}^*.

As a function of crystallization temperature T:

$$J_{hom} = \frac{N_A k_b T}{h_p} e^{\frac{-\Delta G^*_{hom}}{k_b T}} \quad (2\text{-}14)$$

Where N_A is Avogadro constant ($= 6.022\times10^{23}$/mol), k_b is the Boltzmann constant ($= 1.38\times10^{-23}$J/K), hp is Planck's constant ($= 6.626\times10^{-34}$J/s).

However, nucleation is also hindered by the requirement that molecules diffuse to the nucleus's site and adopt the proper conformation to its surface. The diffusion term indicates that as the melt or solution becomes more viscous, its diffusivity decreases at

lower temperatures. This configuration barrier can be included in the term $-\Delta G_{diff}^{*}$ (Himawan, 2006).

$$J_{hom} = \frac{N_A k_b T}{h_p} e^{\frac{-\Delta G_{hom}^{*}}{k_b T}} e^{\frac{-\Delta G_{diff}^{*}}{k_b T}} \quad (2\text{-}15)$$

2.2.2.3 Induction time

Nucleation theory states that a cluster size distribution must be established before nucleation can occur by clusters of the critical size. An induction time (τ_i) is required to build such a cluster size distribution. It is possible to describe the crystallization process under isothermal conditions by the τ_i, which is defined as the amount of time it takes for the first solid nuclei to emerge at T_{onset} under the influence of the thermal driving force.

The induction time is proportional to the difference between the melting temperature (T_m) and the onset crystallization temperature (T_{onset}), which is the degree of supersaturation (solution) or subcooling or undercooling (melt) (Marangoni, 2018). The theoretical homogeneous / heterogeneous nucleation rate is considered reciprocally proportional to the induction time (τ_i) in many nucleation studies (Himawan, 2006).

$$J \sim \frac{1}{\tau_i} \quad (2\text{-}16)$$

Where J is the nucleation rate under isothermal condition, τ_i is induction time.

2.2.2.4 Non-isothermal Nucleation

In the isothermal model, the experimental temperature drops instantaneously from the melting temperature to the set crystallization temperature, and the temperature is kept constant throughout the crystallization process, as illustrated in Figure 2-5 (a). It is also assumed that crystallization occurs only when the crystallization temperature is reached. This model is suitable for studying systems that are not limited by heat transfer. In reality, the heat conduction is limited, and the system in the experiment can only gradually reach the set temperature, not instantaneously, as illustrated in Figure 2-5 (b). These cases are called near isothermal, which can still be considered as being performed in the isothermal condition, however time zero should correspond to the time when the system temperature reaches the set temperature.

Commercially produced materials crystallize under non-isothermal conditions and the temperature varies during the crystallization, as illustrated in Figure 2-5 (c). Heat and mass transfer conditions determine the rate of nucleation and growth of the crystallization. Nucleation rate, in particular, strongly determines the polymorphic forms and the crystal size distribution of these materials, which will eventually impact their mechanical strength, flow behavior, and sensory properties (Sato, 2001; Hartel, 2001; Herrera, 2000). Therefore, it is essential to establish theoretical tools to model the nucleation behavior of these complex organic mixtures under non-isothermal conditions (Marangoni, 2005).

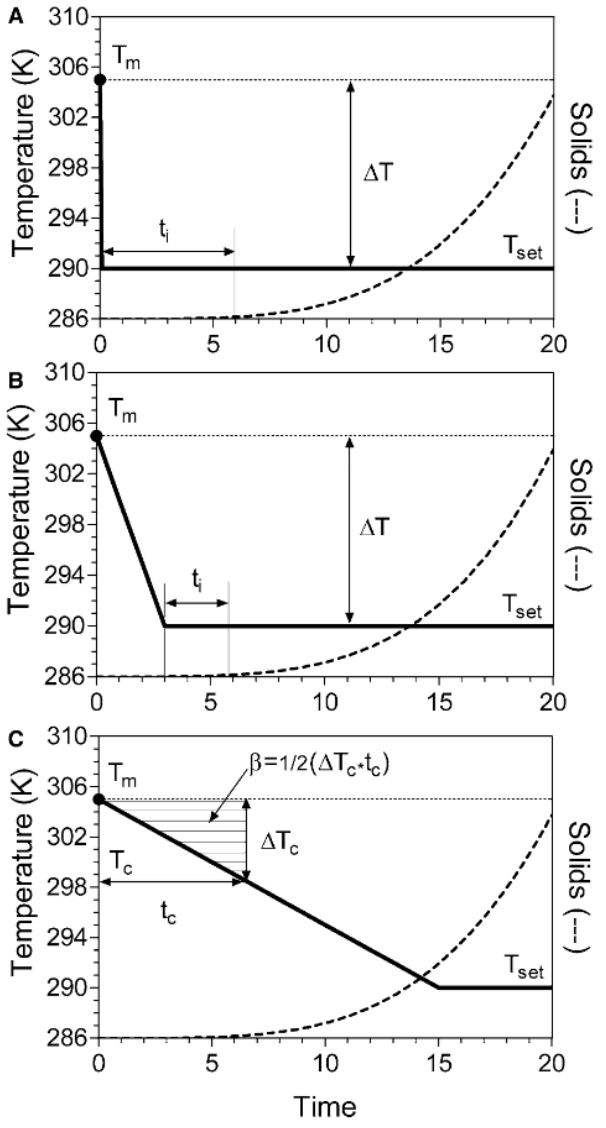

Figure 2-5 Temperature-time profile under isothermal(a), near-isothermal (b), and non-isothermal(c) (Marangoni, 2006a; 2006b) (Permission is granted).

As shown in figure 2-5, under non-isothermal conditions, since the temperature decreases over time, the driving force for nucleation is no longer the difference between the set temperature and the melting temperature, $\Delta T=T_m-T_{set}$. Rather, it is a time-dependent quantity so that the driving force for nucleation (subcooling) varies with the time it takes for the system to cool down from the melting temperature to the set

temperature, i.e., ΔT varies over time as the material crystallizes and changes composition.

Under non-isothermal conditions, the concepts of induction time and undercooling are different from that of isothermal conditions. Two possible ways to model this process are described as follows:

First, as proposed by Marangoni in 2006, all parameters need to be redefined and a new parameter should be added, the supercooling-time exposure (β^2) indicating the non-isothermal crystallization (Marangoni et al., 2006a).

$$\beta^2 = \frac{1}{2}\Delta T_c \cdot t_c \tag{2-17}$$

Where T_c is the crystallization temperate where the first nuclei appear, $T_c=T_m-T_c$.

Define a linear cooling rate as:

$$\phi = \frac{\Delta T}{\Delta t} = \frac{T_m - T_c}{t_c - 0} \tag{2-18}$$

Substituting the ϕ in Equation 2-17:

$$\beta^2 = \frac{\Delta T_c}{\sqrt{2\phi}} \tag{2-19}$$

According to the work of Marangoni et al. (2006), the nucleation rate of fat systems is related to the supercooling-time exposure as follows:

$$\frac{J}{J_{max}} = ke^{-k\sqrt{\beta}} = ke^{-k(\Delta T_c\sqrt{2\phi})} \quad (2\text{-}20)$$

Where J_{max} is the maximum nucleation rate.

The second method to model the non-isothermal nucleation is proposed by our research team (Al-Qatami, 2023).

2.2.3 Crystal Growth

After the formation of nuclei, they grow by absorbing other TAG molecules from the liquid phase. A TAG molecule can be incorporated into an existing crystal lattice if the molecule has the right conformation at the proper location. According to their conformation, molecules weakly attached to the crystal lattice may either integrate into the crystal lattice or return to the supersaturated liquid. Growth will continue as long as there is a driving force for crystallization. The growth of crystals stops when the solid and liquid have reached phase equilibrium, or the material is solidified completely (Hartel, 2001).

There are three kinetic processes during crystal growth: transportation, incorporation, and latent heat removal (Sato, 2018). Molecular rearrangement and reorientation happen at the crystal surface after molecules migrate from the liquid phase. As a result of the concentration gradient of the surrounding environment, the crystal is in a growth-promoting state and growth units are transferred to its surface. Depending on the degree of supersaturation, different amounts of growth units will attach to the surface of the crystal. The higher the degree of supersaturation, the more growth units will be attached.

A growth unit will diffuse on the surface after reaching the surface and will either become a part of the crystal once it reaches a kink or separate from it. Due to the need to transport the growth unit from the solution to the kink site, the rate of crystal growth in solution can be limited kinetically.

An incorporation occurs at the kink site of a crystal when growth units become part of it. There are several factors that affect this process, including density of kink site, temperature, growth unit conformation. To be incorporated into a crystal, a growth unit must possess the correct conformation to match all the other molecules in the crystal. At that point, heat is released during crystal growth, called latent heat. The local temperature near the growing surface increases when latent heat is released from the crystal surface, which decreases supercooling and supersaturation. The growth rate of crystals is reduced as a result. To maintain a constant growth rate under these conditions, it is necessary to remove this latent heat. The Avrami model is discussed in the section 2-5.

2.3 Polymorphism

Polymorphism of fat crystals arises from the different spatial relationships between molecular structures which then determine morphological characteristics (Small, 1986). Polymorphic modifications of fats determine the melting and solidification behaviors, and formation of fat crystals in bulk and emulsion states (Sato,1999). Molecules interact with each other and pack efficiently into a low energy configuration and arrangement in the crystalline state (Sato, 2005). Lipid crystals can have different molecular configurations. This is called polymorphism, which determines their density, melting points, melting enthalpy, specific heat, nanocrystal sizes.

2.3.1 Polymorphic Types and Sub-Cell Structures

There are three relationships that describe the structure of the TAG molecules in a crystal: subcell structure, glycerol backbone conformation and chain length structure. Subcell structures are defined as the lateral packing mode of zigzag hydrocarbon chains, used to determine molecular packing. Lipids have more than nine types of subcell structures. Figure 2-6 depicts three typical subcell structures. Subcell structures of the α, β', and β forms are hexagonal (H), orthorhombic perpendicular (O//), and triclinic parallel (T//).

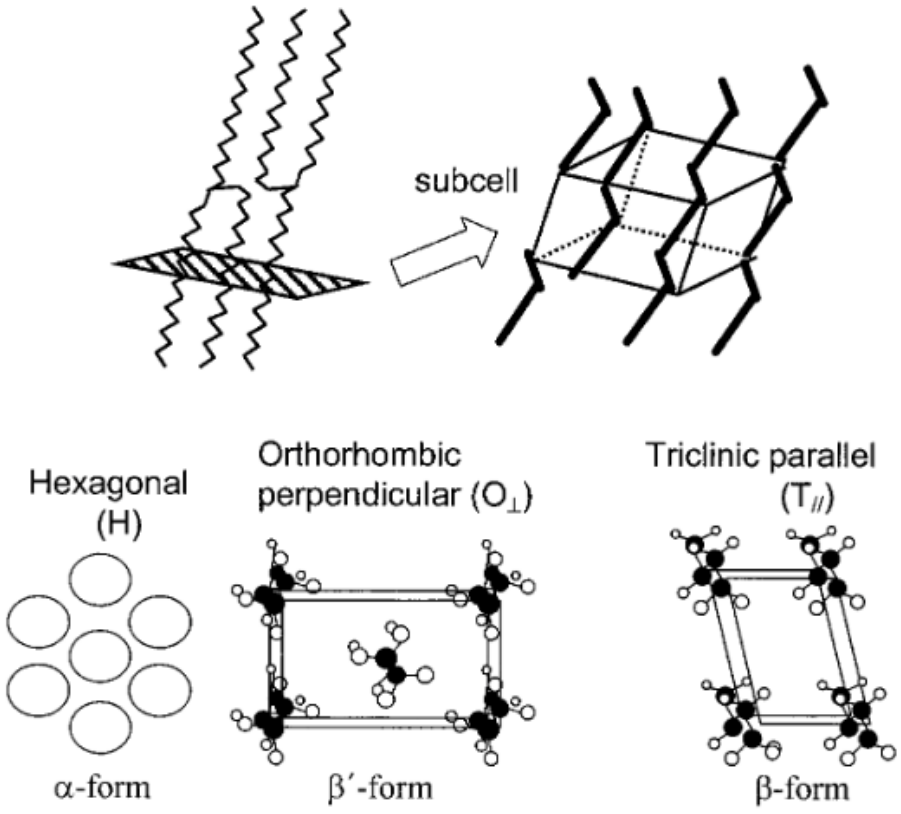

Figure 2-6 Typical subcell structures of TAG polymorphs (Sato, 2005).

The hexagonal subcell structure (H) of the α form has loose chain packing which allows the rotation of the carbon atoms. This results in disordered hydrocarbon chain

conformations which cause loss of specific chain-chain interactions. The β' form has a orthorhombic perpendicular subcell structure ($O_{\perp}$). This has rectangular two-dimensional lattices that are tightly packed and engaged in specific chain-chain interactions. The triclinic parallel subcell structure ($T_{//}$) of β has an oblique two-dimensional lattice and features tightly packed chains.

As the top part of Figure 2-7 shows, subcell parameters of hexagonal, orthorhombic perpendicular and triclinic parallel form planes that are at 0.41nm, two at 0.37 nm and 0.41 nm, and 0.46 nm and week patterns at 0.39 nm and 0.38 nm, respectively. These crystallographic planes generate characteristic wide-angle XRD patterns that allow their identification.

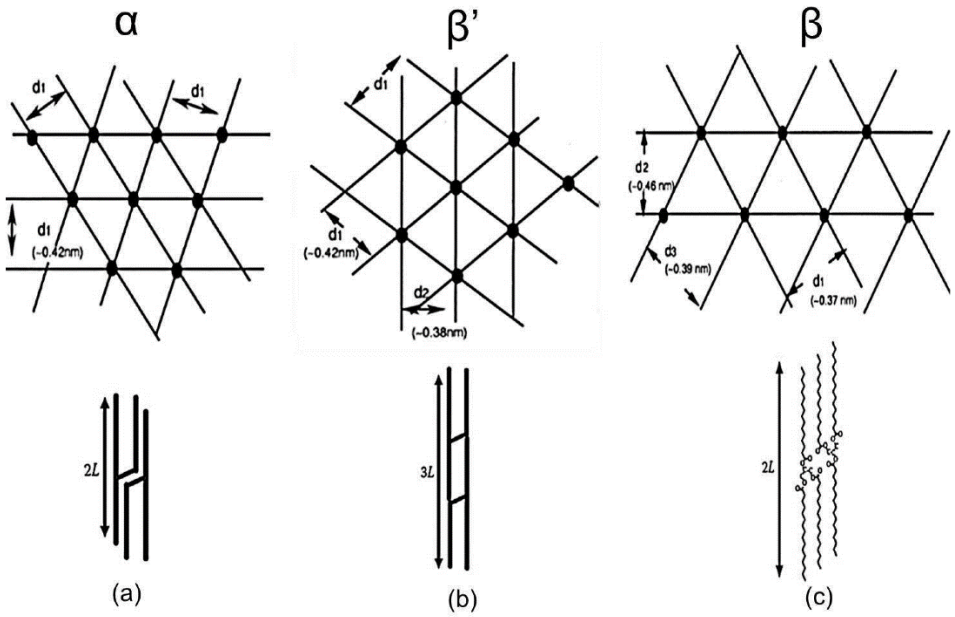

Figure 2-7 Spatial projections of the crystalline forms α, β 'and β (Marangoni & Wesdorp, 2013).

In TAG crystals, hydrocarbon chains are packed along a c-axis in a unit lamellar structure as shown in the bottom of Figure 2-7. One sublayer made up of a single fatty-acid chain is called a leaflet. TAGs in the crystal lattice can have a chair-like or a tuning

fork-like configuration which are characterized by the direction of the three acyl chains. Furthermore, a TAG can be arranged either in a double or in a triple chain-length structure. In a double chain-length (DCL) structure, TAG pairs contain overlapping fatty acids. However, in a triple chain-length (TCL)structure, there is no overlap (Hartel, 2001). Small angle X-ray diffraction patterns are used to identify these long spacings. The combination of SAXD and WAXD analysis is used to identify the crystal structure, hence the polymorphic form.

2.3.2 Thermal events associated with polymorphic transitions

The Gibbs energy difference between a liquid and the crystal of the polymorphic forms illustrate their thermodynamic stability. Polymorphic forms with higher Gibbs value are less stable and leading to a lower melting point. Hence, as Figure 2-8a shows, the least dense packing α form shows the highest Gibbs free energy value and middle for the β′ form, and smallest for the β form. The melting points increase sequentially ($T_{m\alpha} < T_{m\beta'} < T_{m\beta}$). It is primarily due to polymorphs with higher melting temperatures has a higher heat of fusion.

Polymorphism in lipids is monotropic (Figure 2-8b), all the polymorphs can form directly from the melt, yet the unstable forms with lower energy can only transform into more stable forms.

The rate of polymorphic transformation is determined by the length of the fatty acid. The longer the fatty acid chain, the slower the polymorphs are transformed (Sato, 2005). When a liquid fat is rapidly cooled, the α polymorph usually forms first, but it quickly transforms into the either β′ or β form due to its instability. Although the β′ polymorph

may persist for days, in most fats, it will eventually transform into the β polymorph, which is usually the most stable. However, polymorphic transformation depends on the molecular structure of the material, and the time and temperature profile applied on the material. For some TAGs, it can stay in β′ polymorph for a long period under a stable environment.

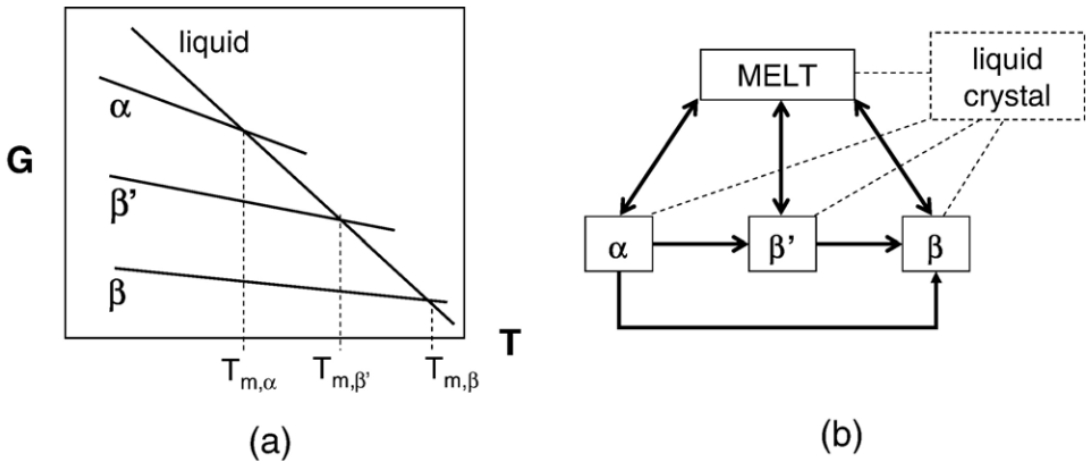

Figure 2-8 Monotropic Polymorphism of TAGs (Sato, 2001) (Permission is granted).

2.3.3 Polymorph-Dependent Nucleation Kinetics

Researchers have investigated a range of knowledge domains to manipulate the physical characteristics of fats subsequent to crystallization. These areas include understanding the molecular and crystal structures of fats, the impact of external factors on transformation mechanisms, the formation mechanisms of fat crystal networks, and the rheological and texture properties of fats. The external factors that affect crystallization can be categorized as dynamic temperature variation, additives, shear, ultrasonication, and emulsification (Sato et al. 2013). Smith et al. (2022) described how additives such as lecithin can modify the crystal structures of fats, while ultrasonic treatment can

enhance the plasticity and spread ability of fats (Rigolle et al., 2015；2016，Ueno et al., 2003；Martini et al., 2008). Shear (Mazzanti et al., 2003; 2011), emulsification (Arirna, 2007; 2009), and dynamic temperature variation(& Narine, 2010a, 2010b; Campos et al., 2002.; Cebula & Smith, 1991; Martini et al., 2001; Yoshikawa et al., 2015) can be used as the method to modify the physical properties of fats for various applications.

Dynamic thermal treatments, such as cooling and heating at specific rates, determine the proportion and presence of the polymorphic forms of TAGs, as well as the transformation between polymorphs. Studies have been conducted on the kinetic processes associated with lipid crystallization mechanisms when subjected to different cooling rates. These investigations were carried out to better understand how the crystallization behavior of lipid systems can be managed under both isothermal and non-isothermal conditions (Marangoni, 2006; Martini et al, 2002; Bouzidi & Narine, 2010).

According to the Ostwald step rule, in the crystallization of different polymorphic forms, the formation of metastable polymorphs happens firstly, followed by transformation into more stable forms (Ostwald 1987). This can be explained by the fact that the energy barrier of metastable forms is lower and easier to cross than the barrier of the stable forms.

However, studies of polymorphic forms and nucleation effects at different cooling and heating rates show that, as cooling rates for liquid decreased, crystals directly formed into more stable forms. This competitive polymorphic crystallization seems to violate the Ostwald rule (Bayés-García et al., 2013; 2015), as shown in Figure 2-9.

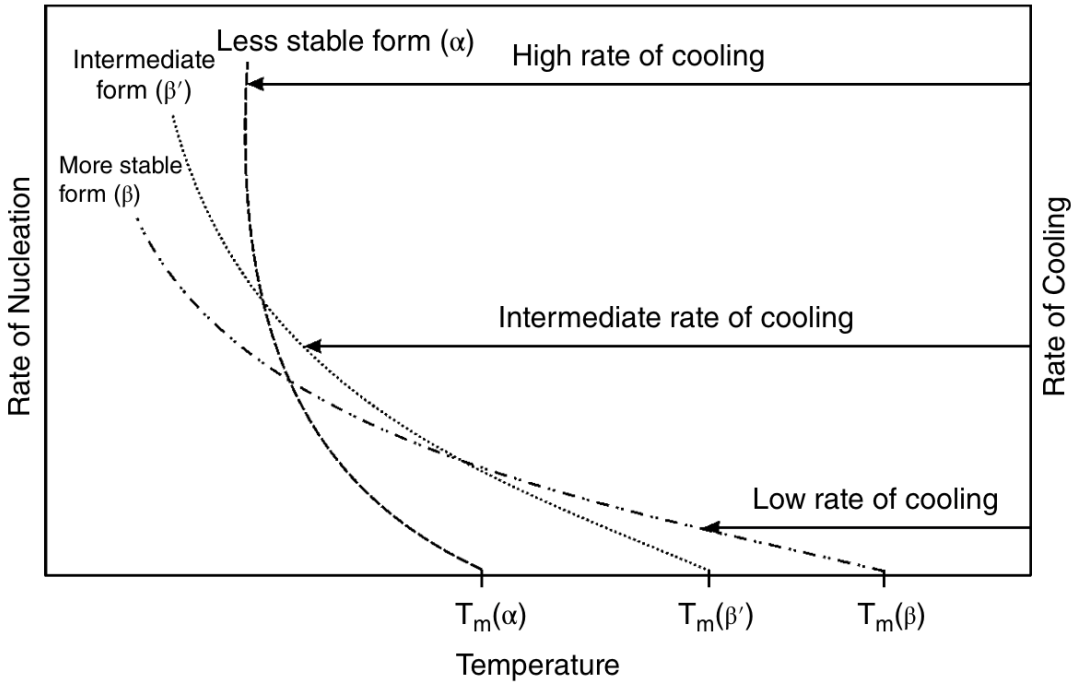

Figure 2-9 Rates of nucleation of polymorphic forms α, β' and β of TAGs under different cooling rates (Sato, 2018)

2.4 Experimental Methods for Investigating Fat Crystallization

2.4.1 Differential scanning calorimetry

Differential scanning calorimetry (DSC) is a powerful analytical technique used to investigate the thermal properties of materials by measuring the rate of heat flow while the sample is heated, cooled, or kept isothermal. The sample absorbs or releases heat as it is responds to the temperature and time profile in the DSC cell. From the thermal behavior of the material, it is possible to determine its specific heat, enthalpy, and phase transition temperatures. There are two main types of DSC instruments: heat-flux DSC and power-compensation DSC. Heat-flux DSC measures the temperature difference between the sample and the reference using two separate thermocouples, one in each

cell. As the temperature is ramped up or down, the difference in temperature between the sample and reference is recorded and plotted as a function of time or temperature. This type of plot is called DSC thermogram. Power-compensation DSC, also known as heat-balance DSC, operates on the principle of compensation of thermal effects. In this type of DSC, the temperature of the sample and reference is kept the same by adjusting the heating power applied to the sample and reference cells. The amount of power required to maintain the same temperature in both cells is measured and plotted as a function of time or temperature.

Many industries, such as materials science, pharmaceuticals, food science, and biotechnology, commonly use DSC for exploring the thermal stability, phase transitions, and other thermal characteristics of materials. For example, the endothermic peak detected in a thermogram through DSC represents the heat absorbed during the shift from solid to liquid states. This feature helps in determining the melting point of materials. DSC can also be utilized for measuring various thermal transitions like the alterations seen in heat capacity, enthalpy, and entropy. The measurement of heat capacity involves calculating the slope of a thermogram at a fixed heating or cooling rate, or an oscillatory temperature profile. Enthalpy changes are assessed through the area under the peaks in a DSC thermogram.

Several variants of DSC have been developed to meet specific needs. For example, modulated DSC (MDSC) applies a small sinusoidal temperature modulation to the sample and reference cells and analyzes the response of the system to obtain information about the kinetics and reversibility of thermal transitions (Syamala, 2018; Reading,

2006). High-pressure DSC is used to study materials under high-pressure conditions, and micro-DSC is used to analyze very small samples.

2.4.1.1 Heat flux Differential Scanning Calorimetry

During the same thermal treatment, Heat flux differential scanning calorimetry measures the temperature difference between a sample and a reference material within a common thermal enclosure. That thermal enclosure is the DSC cell. This temperature difference is used to calculate the amount of heat absorbed or released by the sample relative to the reference material, and to construct a thermogram of the sample's thermal behavior. The measured signal ΔT is converted to a heat flow rate using a temperature dependent proportionality factor:

$$\dot{q} = \frac{\Delta T}{K(T)} \tag{2-21}$$

Differential temperature sensors are constructed using different materials and geometry, which determines the proportionality factor K(T). Mathematical models are used to determine the relationships between temperatures and heat flow. Heat flow measurements are analyzed based on the lump heat capacity method in which thermal resistances and heat capacities are used to represent a thermal system. The diagram presented in Figure 1 represents a circuit that can be utilized to demonstrate the measurement of heat flow in a DSC. The calorimeter comprises a thermal resistance and a heat capacity, and each calorimeter is designated with the subscripts 's' or 'r' to distinguish the sample and reference calorimeters. The temperatures of the sample and reference calorimeters are denoted by T_s and T_r, respectively, while T_0 represents the temperature of the DSC enclosure. The measured heat flows for the sample and reference are q_s, q_r.

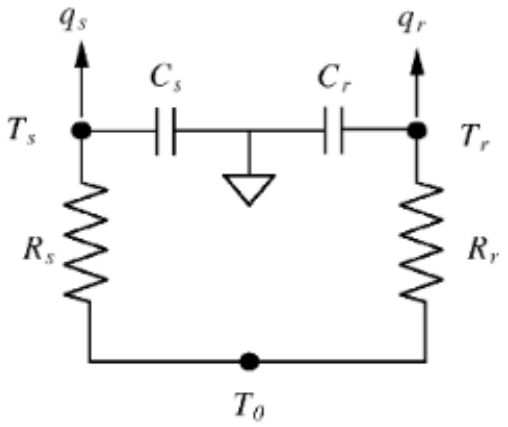

Figure 2-10 Heat flow measurement model of heat flux DSC (Danley, 2003)

The heat flow equation giving the difference between the sample and reference heat flows:

$$\dot{q} = -\frac{\Delta T}{R_r} + \Delta T_0 \left(\frac{1}{R_s} - \frac{1}{R_r}\right) + (C_r - C_s)\frac{dT_s}{dt} - C_r \frac{d\Delta T}{dt} \tag{2-22}$$

The first term represents the principal heat flow (conventional heat flow), the imbalance in thermal resistance and heat capacities between sample and reference calorimeters are the second and third terms, respectively. The fourth term is the difference of the heating rate between the thermometer of the sample and reference. The value of the thermal resistance thermal resistance and heat capacitance is calculated in the process of Tzero™ calibration (Danley, 2003).

In the calibration procedure, two identical constant heating rate experiments are conducted with an empty furnace first, and a pair of sapphire disks without pans at the sample and reference positions is performed next. The curves should be smooth and continuous. Resistance values should decrease with temperature as capacitance values

increase. Often, however, the two sides are not exactly the same and further adjustment is required.

Thermal contact resistance is the barrier to the heat flow of heat across the interface between two solid surfaces. There is a limited direct contact between two mating surfaces as a result of imperfections. Imperfect (non-intimate) contact between pan and sensor causes lag in heat flow which decreases the resolution.

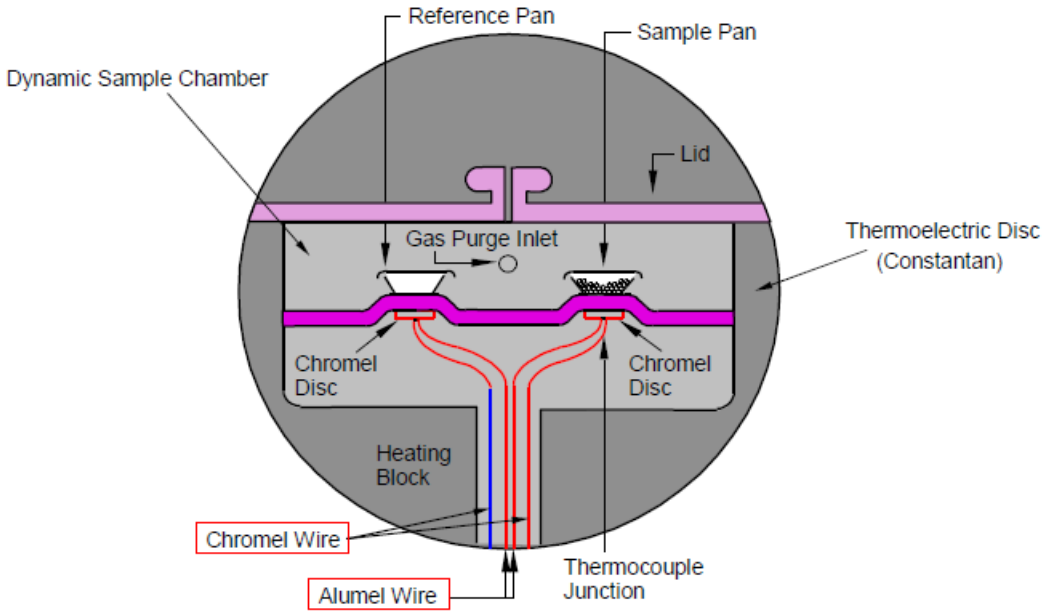

Figure 2-11 Heat Flux DSC Cell Schematic (Danley, 2003)

2.4.2 X-ray diffraction

X-ray diffraction (XRD) is one of the most commonly used methods to study the crystallization of a wide range of materials. X-rays are diffracted by crystalline solids because their wavelengths are comparable to atomic spacing. The arrangement of atoms scatters X-rays in different directions, and the scattered waves interfere with each other to create a diffraction pattern. A diffraction pattern is a series of points or peaks, each

peak produced by a specific set of planes within the crystal lattice. When waves interfere with each other, diffraction occurs. A wave's intensity is enhanced if its amplitudes are in phase; if they are out of phase, their intensity is decreased. A similar wavelength and periodicity of crystals can produce diffraction effects when waves interact with them. This interference occurs as sharp peaks when the atomic structure of the solid is ordered. There is a strong correlation between diffraction patterns and periodic atomic structures in materials. Diffraction at low angles is caused by periodicities with long repeated distances, whereas diffraction at high angles is caused by periodicities with short, repeated distances.

The position of the diffraction peak determines the shape and size of the unit cell, while the intensity of the diffraction peak determines the position and number of atoms within the cell. With atoms having diameters of the order of Ångströms (1 Å = 10^{-10} m), unit cells have dimensions of several Å (Stanjek & Häusler, 2004).

Like all electromagnetic waves, X-rays have a wavelength and a frequency, related by the equation:

$$\lambda = \frac{c}{\nu} \tag{2-23}$$

where λ is the wavelength, ν is the frequency, and c is the speed of light. X-rays have very short wavelengths (typically on the order of 0.1 to 1.0 nm), and very high frequencies (typically in the range of 10^{16} to 10^{19} Hz).

In crystals, monochromatic X-rays interact with layers of atoms/molecules and produce diffraction patterns determined by the arrangement of atoms. Molecular layers

in TAG crystals are segmented into characteristic distances called d-spacings (Figure 2-6, 2-7), which are characteristic of periodic layer arrangements.

Bragg's law describes the conditions for constructive interference of scattered X-rays from adjacent crystal lattice planes, resulting in strong diffraction peaks. The angle of incidence and wavelength are typically fixed in X-ray diffraction experiments. The crystal structure can be determined from the pattern of diffraction peaks and peak intensities as a function of scattering angle. The spacing between crystal lattice planes can then be calculated using Bragg's law. Bragg's law can be mathematically expressed as the condition that the path difference between the X-rays scattered from adjacent crystal lattice planes is equal to an integer multiple of the wavelength, nλ, resulting in the position of each diffraction spot in the pattern.

$$n\lambda = 2d \sin\theta \tag{2-24}$$

where λ is the wavelength of the X-rays, d is the spacing between crystal lattice planes, θ is the angle of incidence of the X-ray beam, and n is an integer that represents the order of diffraction. This equation can be derived from the principle of constructive interference, which states that waves that are in phase will interfere constructively and produce a bright spot, while waves that are out of phase will interfere destructively and produce a dark spot.

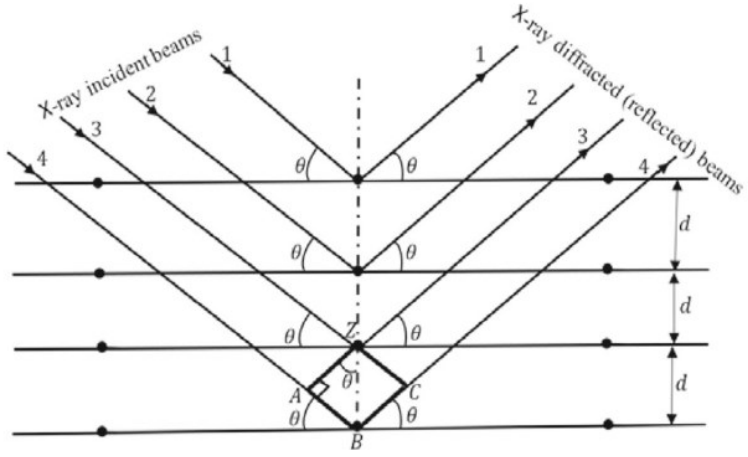

Figure 2-12 X-ray diffraction pattern Schematic, where nλ =AB+BC= 2AB(Ameh, 2019)

The intensity of X-rays that is scattered by a given sample must be measured as a function of the scattering angle 2θ, to obtain the full diffraction pattern of the crystal. The scattering vector q, which is independent from the wavelength, is defined as

$$q = \frac{2\pi}{d} \tag{2-26}$$

Therefore, the relationship between scattering angle(2θ) and scattering vector(q):

$$q = \frac{4\pi \sin\theta}{n\lambda} \tag{2-25}$$

2.4.2.1 Time resolved synchrotron radiation X-ray diffraction (SR-XRD)

A synchrotron X-ray is an X-ray produced by a synchrotron facility, which is a large particle accelerator that generates highly intense and bright beams of electromagnetic radiation. A map of beamlines is shown in Figure 2-11. Synchrotron X-rays are highly advantageous in comparison to other X-ray sources due to their increased brightness, tunability, and narrow bandwidth, which enables their utilization in various scientific

applications, including materials science, biology, and chemistry. As high energy electrons circulate around a synchrotron's storage ring at near-light speeds, they emit electromagnetic radiation, which is focused and directed towards samples for various scientific investigations.

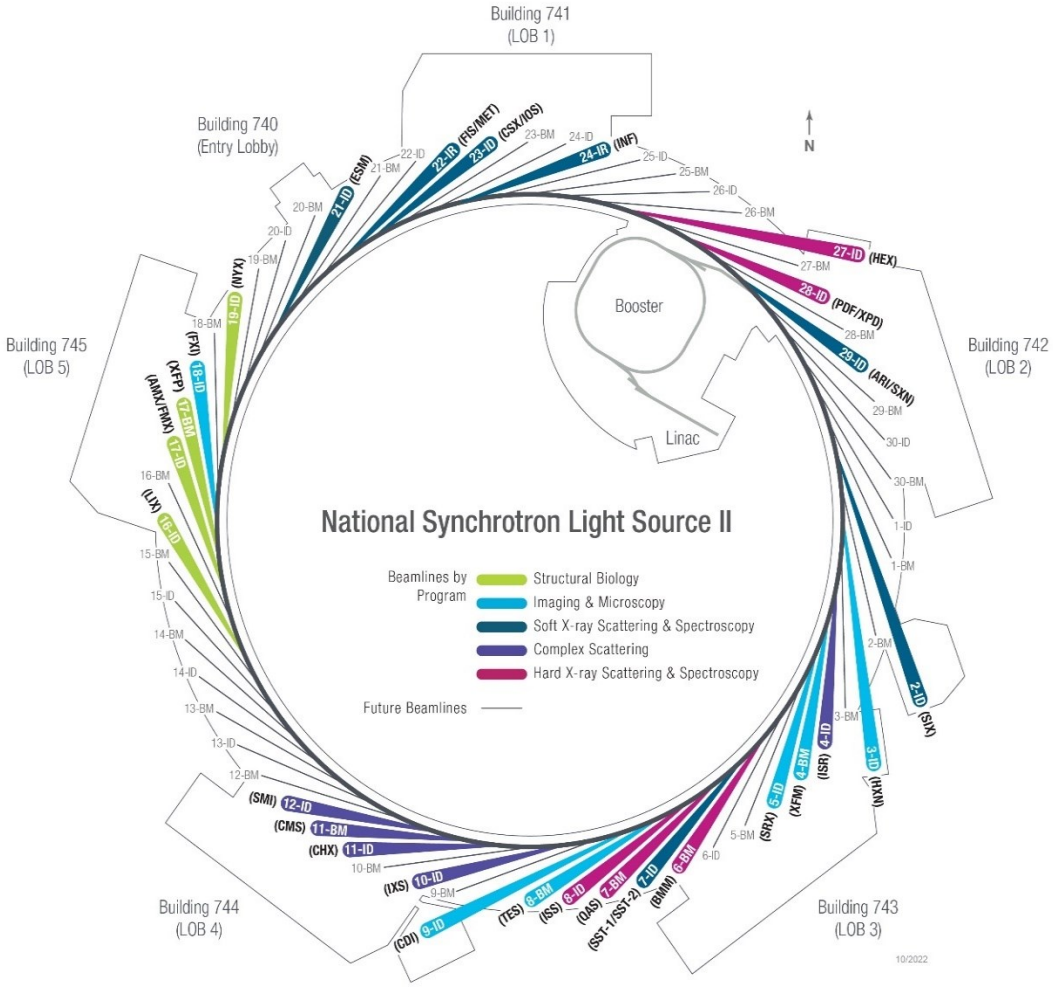

Figure 2-13 National Synchrotron Light Source II Beamline Map in Brookhaven National Laboratory (https://www.bnl.gov/nsls2/beamlines/map.php)

Research on fat crystallization using synchrotron X-rays has extensively studied polymorphism and polymorphic transformations, as well as in modeling crystal growth

kinetics (Bayés-García et al., 2011a, 2011b, 2013; Kellens et al., 1990; Kovalev & Ponomarev, 2019; Minato et al., 1997; Minato et al., 1996a, 1996b; Verstringe et al., 2014). This is because synchrotron X-rays have several unique properties that make them well-suited for studying the molecular structure of materials at the nanoscale, including fats and oils. One of the primary advantages of synchrotron X-rays is their ability to produce highly intense and focused beams of X-rays, which allows for precise measurements and analyses of the molecular structure of materials. This can be particularly useful for studying the crystallization process of fats, which involves the formation of complex crystalline structures at the molecular level.

Due to the complex and highly ordered molecular structures of fat crystals, synchrotron X-rays are well-suited for identifying and quantifying polymorphic forms of fats and oils, which cannot be characterized using other techniques. Small- and wide-angle X-ray scattering studies (SAXS/WAXS) are possible at most synchrotron radiation facilities through the use of specialized beamlines ((Bolze et al., 2018).

Pre-characterizing samples in the laboratory in advance is essential to making the best use of beam time at these facilities and to have the beam time proposal approved. Using a synchrotron radiation source, time-resolved synchrotron X-ray techniques determine structural changes over short periods of time in materials. Typically, a short pulse, lasting a few milliseconds, of synchrotron X-rays is introduced periodically and the scattering patterns are collected over time.

It is possible to obtain detailed information on the structural changes that occur during fat crystallization by using time-resolved synchrotron X-ray techniques under non-isothermal conditions. When a synchrotron source emits pulses of X-rays at short

intervals, a sample of fat can be heated at a controlled rate and then rapidly quenched at a low temperature through a time-resolved X-ray diffraction experiment. In addition to providing information on the crystal structure, X-rays also provide information about the orientation of the fat crystals.

2.5 Mathematical Modeling of Crystallization in Fat

2.5.1 Avrami Model

The Avrami model was first proposed by Avrami and was initially developed to describe the kinetics of solid-state transformations such as nucleation and growth of crystals (Avrami, 1939). The Avrami model has been widely used in materials science, metallurgy, and other fields to describe various phase transformations. The model is also known by the names of other researchers developed it as the same time. The mathematic form is the same as the Weibull distribution.

The Avrami model assumes that the transformation process occurs through nucleation and growth of new phases, with the rate of transformation depending on the number and size of the newly formed phases. Applied to the study of fat crystallization, the following equation expresses our version of the Avrami model:

$$\frac{SFC}{SFC_{max}} = 1 - e^{-\left(\frac{t}{b}\right)^{a}} \tag{2-27}$$

where:

(1/b) is the same as k, the rate constant for the transformation process, ‘a’ is the same as n, the Avrami exponent; t is the time of transformation; SFC is the solid fat content at a

particular time (%), SFC_{max} correspond to the maximum SFC achieved at a particular temperature (%). SFC could be percentage or fraction.

A crystallization event described by the equation occurs after a lag period, during which pre-nucleation is happening. Initially the crystallization is slow and its then followed by a rapid increase in crystal mass. As the crystallization gets closer to the end, it slows down until the material reaches equilibrium. The Avrami model assumes that the crystal growth process occurs through nucleation and growth of new crystal phases, with the rate of transformation depending on the number and size of the newly formed crystals. The transformation process can involve the growth of new crystals from a solution or melt, or the transformation of an existing crystal from one phase to another. The exponent 'a' is the sum of nucleation and growth modes. The instantaneous nucleation mode adds 0 to the exponent, whereas the periodic nucleation mode adds 1. The growth mode refers to the dimensions of growth. If the dimension is linear, adds 1 to the exponent, for surface adds 2, for volume adds 3. Therefore, the exponent should be between 1-4. In practice, the exponent falls between a small positive number, for example 0.1. and value larger than 5, and it is not an integer.

According to the model, the growth rate of the new phase depends only on temperature, and not on time. The model was developed for iso-thermal conditions, random nucleation in space, and linear growth kinetics. Growth bodies are assumed to remain at the same density (Marangoni & Wesdorp, 2013).

To implement the Avrami model in crystal growth studies, one typically measures the fraction of transformed material as a function of time during the transformation process. This data can then be fit into the Avrami equation to estimate the rate constant and the

Avrami exponent, which can provide insights into the mechanism of the transformation process. The Avrami model can also be used to predict the fraction of transformed material as a function of time for different growth conditions or crystal morphologies, which can be useful for optimizing crystal growth processes.

CHAPTER 3 EXPERIMENTAL METHODS

3.1 Materials

There are four pure monoacid triacylglycerols studied in this work. Trilaurin (LLL), Trimyristin (MMM), Tripalmitin (PPP) and Tristearin (SSS) samples were obtained from Fluka (via Sigma Aldrich) at more than 99% purity and were used without further purification.

3.2 Instruments and Methods

Note that on this thesis we use "°C" to refer to temperatures, whereas we use "C°" to refer to differences in temperature or rates associated with temperature, for example in specific heats or cooling rates.

3.2.1 X-ray diffraction

3.2.1.1 Experiment Procedures

The X-ray study was conducted using time-resolved in situ small-angle and wide-angle X-ray diffraction (SR-SAXD/WAXD) measurements with synchrotron radiation to identify each polymorphic form. Dr. Gianfranco Mazzanti and Elizabeth Mudge conducted the experiments (Anom, 2009). The synchrotron radiation XRD (SR-XRD) experiments were performed at the Exxon Mobil beamline X10A at the National Synchrotron Light Source (NSLS) in Upton, NY, USA. A Bruker 1500 two-dimensional CCD detector with a pixel size of 0.2004 mm was used to capture diffraction patterns with an exposure time of 5 seconds and an additional 5 seconds to read and "unwarp" the images.

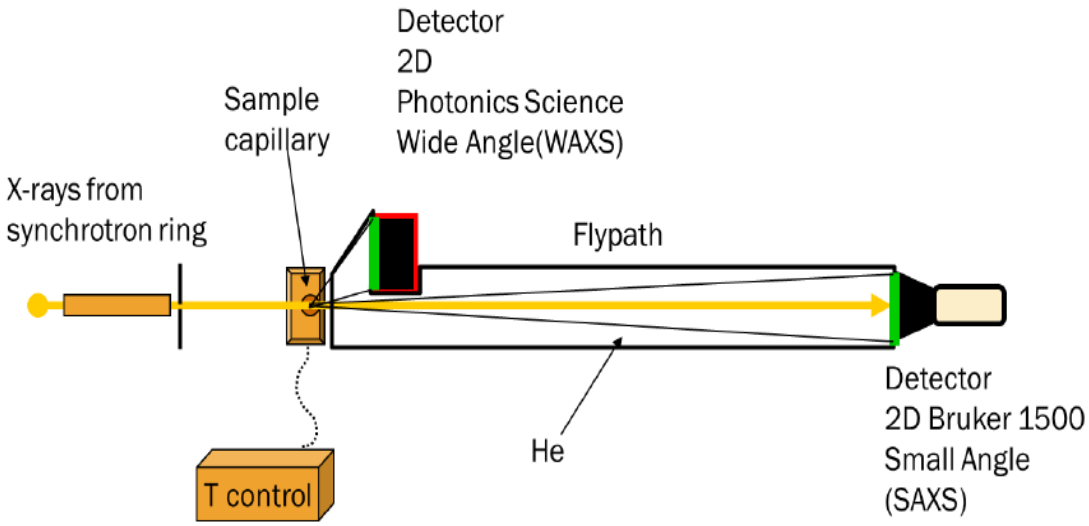

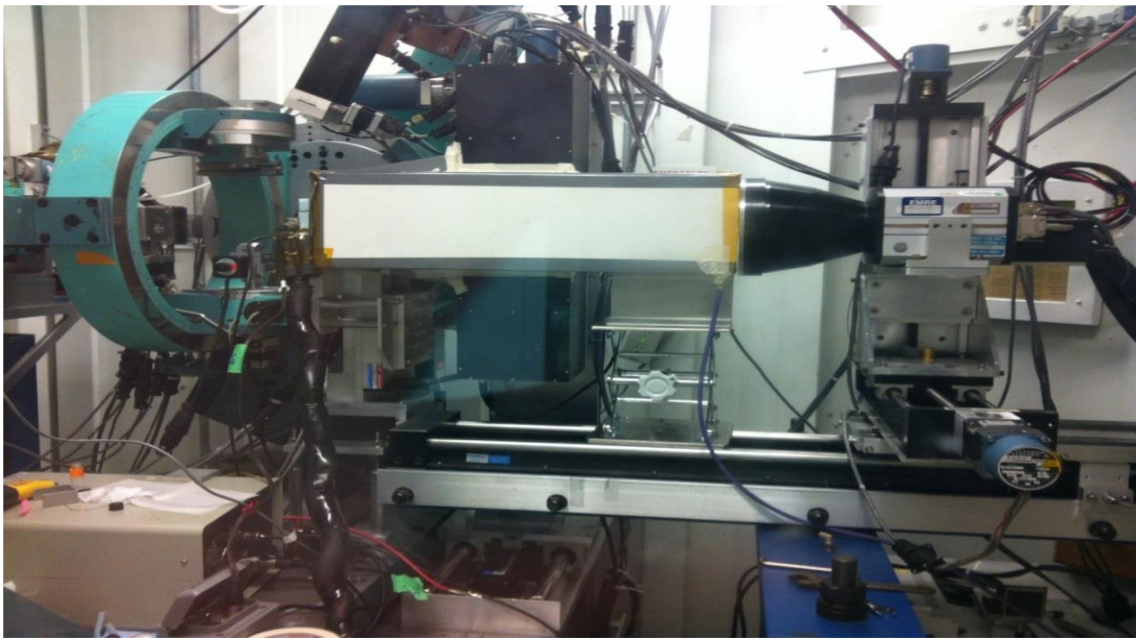

Figure 3-1 A schematic and a corresponding photo of setup for X-ray diffraction experiments performed at NSLS (Batchu, 2014).

Experiments were conducted with a wavelength of λ=1.09468Å. The small-angle X-ray diffraction (SAXD) detector was at a distance of 1014.6 mm from the capillary. Wide-angle X-ray diffraction (WAXD) measurements were performed with the detector

placed 136.8 mm away from the capillary. Silicon powder and aluminum oxide were used to calibrate the beam's energy, with a beam size of 0.5 x 0.5 mm. The instrumental resolution was 0.0027 $Å^{-1}$.

The sample was loaded into a 1.5 mm thin glass capillary. The capillary was placed in a temperature-controlled holder designed to be compatible with X-rays. To regulate the temperature of the sample in the capillary, an aluminum holder containing a group of Peltier elements was employed. A thermistor was used to monitor the temperature, and a window was provided to allow X-rays to pass through. The voltage applied to the Peltiers was calculated using a Proportional, Integral, Derivative (PID) algorithm to maintain a stable temperature in the capillary cell. A LabVIEW program was jointly developed by Dr. Gianfranco Mazzanti and Dr. Stefan Idziak, and then modified to regulate the temperature of the capillary cell and log its temperature and other operational parameters.

The program's graphical user interface (GUI) enables users to input a temperature profile. The set point temperature is calculated dynamically based on the temperature profile's stage and time and transmitted to the temperature controller. The LabVIEW program records each temperature cycle's time, actual temperature, and set point temperature in a log file, and sends the capillary cell temperature to another program that captures and saves diffraction patterns from one of the detectors.

The capillary was heated to 70 °C for 10 minutes before each experiment, cooled at a determined cooling rate to -10 °C, kept at that temperature for 5 minutes, and then heated back up to 70 °C at a rate of 5 C°/min. The experimenters explored seven different cooling rates, ranging from 1 C°/min to 20 C°/min.

3.2.1.2 X-ray Data Analysis

ImageJ with an XR2D plug-in was utilized to open the Bruker-Siemens (BS) images and generate radial plots. The XR2D plug-in within the program opened the images as a stack of 16-bit greyscale images measuring 512 X 512 pixels. The plug-in also allowed the definition of the analysis boundaries to use information from the pixels in the corners.

For consistency, the same region of interest (ROI) boundary was applied to each image stack, with x Left = 24.0, x Right = 497.0, y Up = 20.0, and y Down = 493.0, and was used in the radial analysis. Thus, only the pixels within the specified boundary were used for the image analysis. The diffraction patterns acquired in the experiment were circular or ring-like. To accurately determine peak positions, intensities, and FWHM, the image stack was centred prior to radial analysis by adjusting the boundary of analysis. The center of the diffraction pattern was estimated by defining a range of radii in pixels and fitting a circle to the scattering circle to determine its center and radius.

A radial plot (RP) displays integrated intensities around concentric circles as a function of distance from a point in the image. The sum of pixel values around a circle with a specified center point and radius is used to obtain integrated intensity values for the radial plots. These plots provide information on peak position, X-ray scattering intensity, and FWHM, and can be used to study the kinetics of a process over time. Incident beam intensity is monitored, and results are normalized using a macro developed by Dr. Gianfranco Mazzanti for ImageJ, named Normalized Radial Plots (NRP). Temperature and monitor plots over time are recorded, shown in the figure for LLL cooled at 10C°/min.

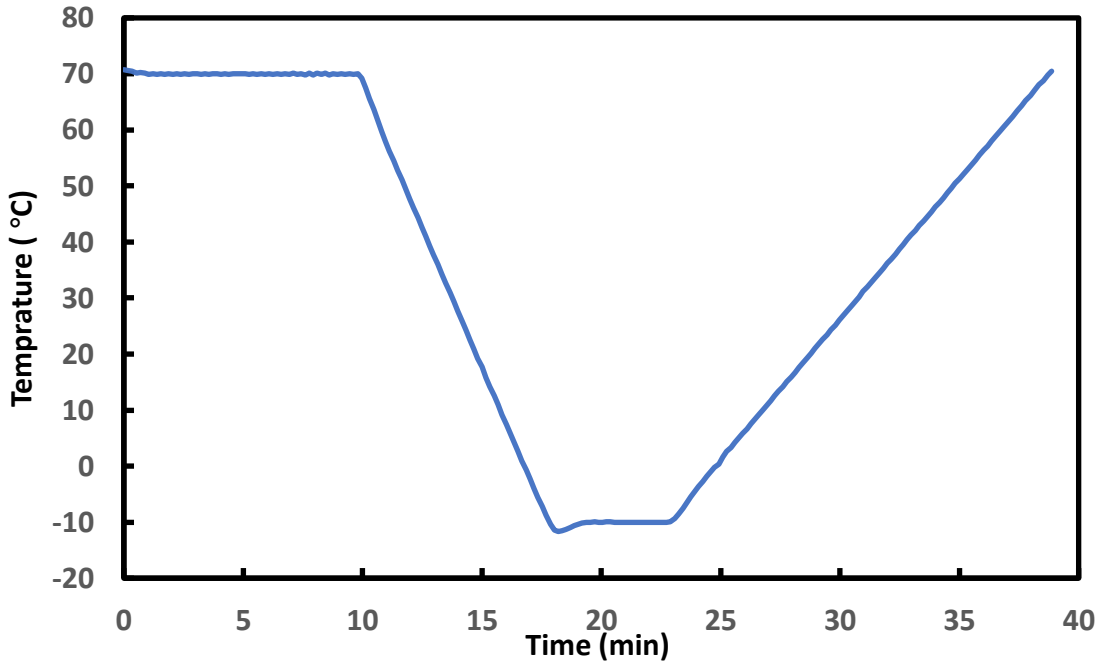

Figure 3-2 Temperature as a function of time showing cooling at 10 C°/min and heating at 5 C°/min for LLL.

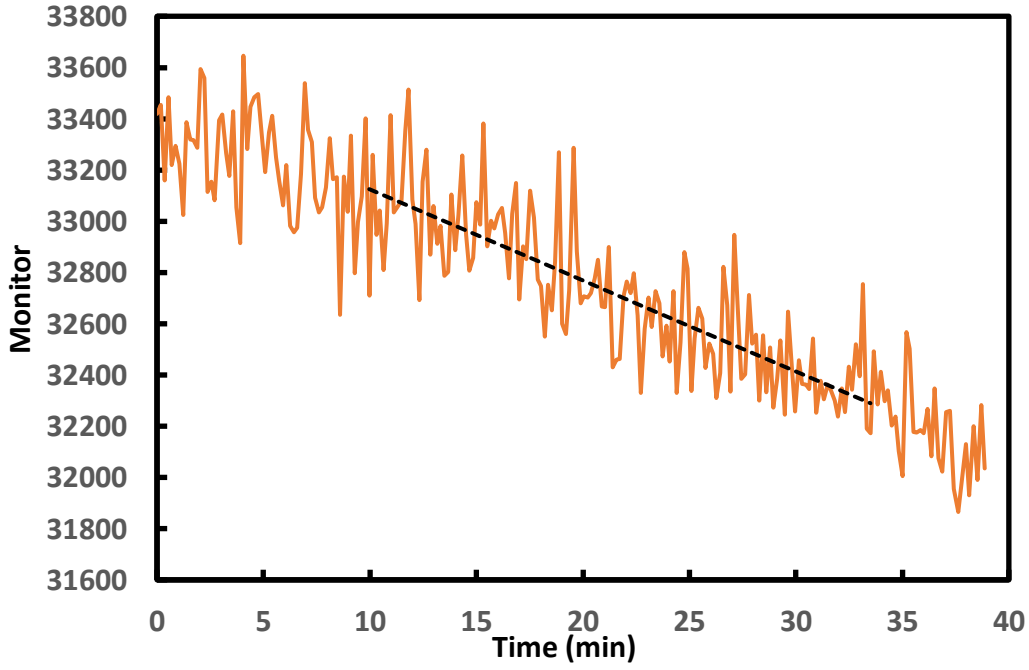

Figure 3-3 Monitor value as a function of time showing the decay of scattering intensity with time.

The assumption in this analysis is that each peak represents a different polymorphic form or crystal type in the samples. The extracted image text files were analyzed using Igor Pro9, a scientific data analysis software package produced by Wavemetrics Inc. for curve fitting and peak fitting. The program uses the Levenberg-Marquardt algorithm, which is a numerical method for minimizing non-linear functions in least-squares curve fitting and non-linear programming.

To detect hidden peaks that standard instruments may miss, the data underwent peak fitting to achieve a minimal degree of error and quantify each peak. This process involved fitting the data to a function that is a sum of functions, with each function representing one peak. To account for any slowly varying baseline that the peaks may sit on, a function representing its shape was included in the fitting process.

The fitting function used in this study was the Voigt function, which is a convolution of both Gaussian and Lorentzian functions (Limandr, 2008). While both distributions are continuous probability distributions and relate the probability of observing a value to an interval, the Lorentzian distribution does not diminish to zero as rapidly as the Gaussian distribution. Instead, its behaviour for large deviations is proportional to the inverse square of the deviation rather than exponentially related to the square of the deviation.

Gaussian distribution is a continuous probability distribution for a real-valued random variable. The tails of the distribution are asymptotic, meaning that the probability of observing values far from the mean becomes very small, but never quite reaches zero. The general form of its probability density function expressed as:

$$G(q;\sigma_q) = \frac{1}{\sigma_q\sqrt{2\pi}} e^{-\frac{1}{2}\left(\frac{q-q_o}{\sigma_q}\right)^2}$$

where q is the scattering vector, q_o is the peak position, and σ_q is a standard deviation proportional to the FWHM of the peak.

The Lorentzian distribution, also known as the Cauchy distribution, is a continuous probability distribution that is used in statistics and physics. It is defined by a single parameter, the location parameter (q_o), which specifies the location of the peak of the distribution. The Lorentzian distribution probability density function is expressed as:

$$L(q;\gamma_q) = \frac{1}{\pi}\left[\frac{\gamma_q}{(q-q_0)^2 + {\gamma_q}^2}\right] \quad (3\text{-}1)$$

where q is the scattering vector, q_o is the peak position, and γ_q is the scale parameter or the half-width at half-maximum (HWHM=FWHM/2).

The Voigt distribution is a continuous probability distribution that is commonly used in various scientific fields, including spectroscopy, crystallography, and materials science. It is a convolution of a Gaussian distribution and a Lorentzian distribution, and its probability density function (PDF) can be expressed as:

$$V(q;\sigma_q,\gamma_q) = \int_{-\infty}^{\infty} G(q';\sigma_q)L(q-q';\gamma_q)dq' \quad (3\text{-}2)$$

Therefore:

$$V(q;\sigma_q,\gamma_q) = \int_{-\infty}^{\infty} \frac{1}{\sigma_q\sqrt{2\pi}} \cdot \frac{\gamma_q}{\pi\left((q-q_0)^2+{\gamma_q}^2\right)} \cdot e^{-\frac{(q-q_0)^2}{2\cdot{\sigma_q}^2}}\, du \qquad (3\text{-}3)$$

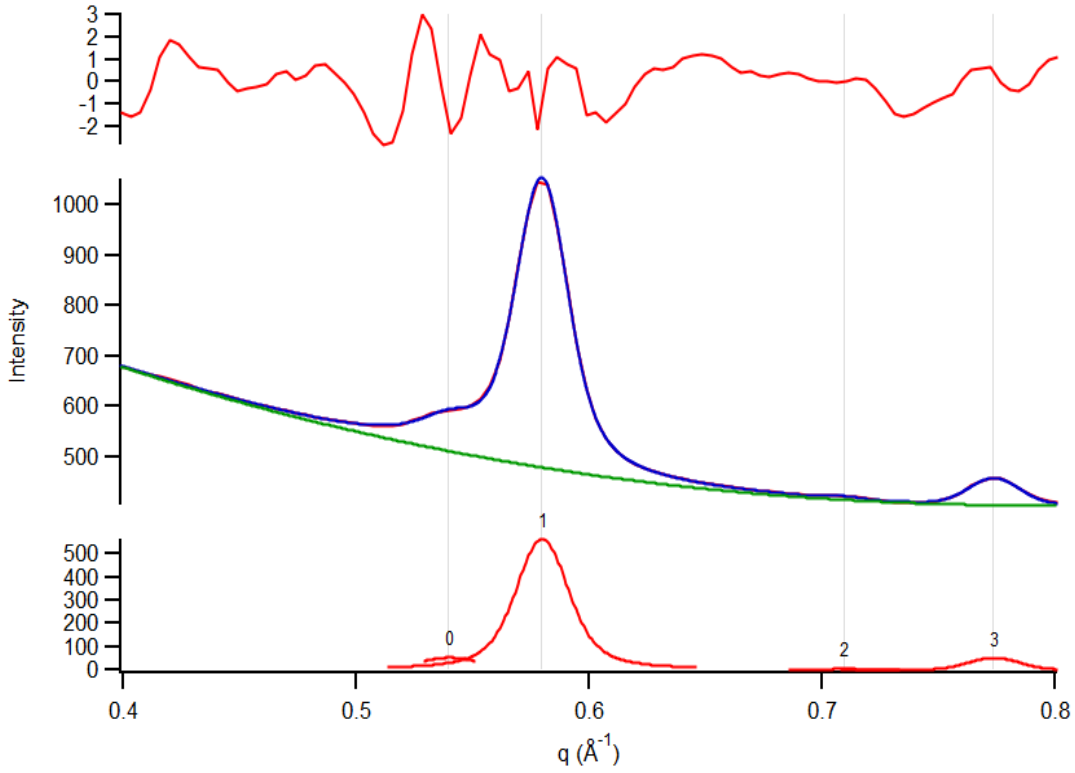

Figure 3-4 Intensity of XRD as a function of scattering vector q obtained at a cooling rate of 5 C°/min(left) and the functions fitted to peaks (003) and (004) from Igor using Voigt distribution. Top plot is the residual error, mid plot has the data and the fit, and bottom plot shows the individual peaks.

3.2.2 Differential Scanning Calorimetry (DSC)

3.2.2.1 Sample preparation and the instruments

To produce the sample for the DSC analysis, the samples were melted in an oven (Precision Thelco) at a temperature of 80°C until they melted and then were transferred into the pan. The samples were then encapsulated in two different kinds of hermetic aluminum pans and lids, the standard pan/lid set (DSC84005 compare to TA Instruments

900793/4.901) and the premium pan/lid set (DSC84012 compare to TA Instruments Tzero901683/4.901) which were obtained from DSC consumables, Inc. All the surfaces and apparatuses were cleaned by immersion in acetone, and the pans were handled with clean tweezers and placed on clean surfaces. Approximately 3-6 mg of melted sample were transferred into the sample pan using preheated disposable capillary tubes with a wire plunger (Drummond Scientific Company, Wiretrol® II, Cat. Number 5-000-2010, 5μL and 10μL). The lids were subsequently sealed onto the pans using the encapsulating press (TA Instruments, 900680.902). The sealed pan was then weighed using a microbalance (Cahn Instruments, C-33 Microbalance Model Number 13633-013)

In this work, two different Differential Scanning Calorimetry (DSC) instruments were utilized for thermal analysis: TA Instrument Q100, and TA Instrument Q2000 (TA Instruments, New Castle, DE, US). The experiments were mainly conducted using a TA Instrument differential scanning calorimeter DSC Q100 (V9.4 Build 287, Module DSC Standard Cell FC) connected to a Windows-based computer system. The device has a refrigerated cooling system (RCS), a Modulated DSC MDSC® option, a touch screen, and an auto-lid. A paired nitrogen cooling system provides the highest performance and greatest flexibility in cooling. It has a large range of temperature performance (-180°C ~ 550°C), and the greatest cooling rate capacity (up to 200C°/min).

The Q2000 is upgraded with advanced Tzero ® technology, and an optional Modulated DSC ® and 50-position autosampler. Additionally, the Q2000 includes Platinum™ software that schedules automatic tests to keep the DSC in top operating condition. The Tzero cell design of the Q2000 is optimized for heating and cooling. It features a heat flow sensor machined symmetrically from a single piece of durable, high-response

constantan and directly brazed to the silver heating block. This design ensures fast signal response, reproducible baselines, superior sensitivity and resolution, precise data, and unmatched ruggedness. The Tzero thermocouple, located symmetrically between the sample and reference sensor platforms, acts as an independent measurement and furnace control sensor. The matched chromel area thermocouples welded to the underside of each sensor platform provide independent sample and reference heat flow measurements, resulting in superior DSC and MDSC ® results.

The Q2000 also features an improved auto lid assembly that includes dual silver lids, a lifting/venting mechanism, and a dome-shaped heat shield. This design improves the thermal isolation of the cell, resulting in more accurate and reproducible measurements. Mass flow controllers and integrated gas switching allow for precise control of purge gas flow rates, with rates adjustable from 0-240 mL/min in 1 mL/min increments.

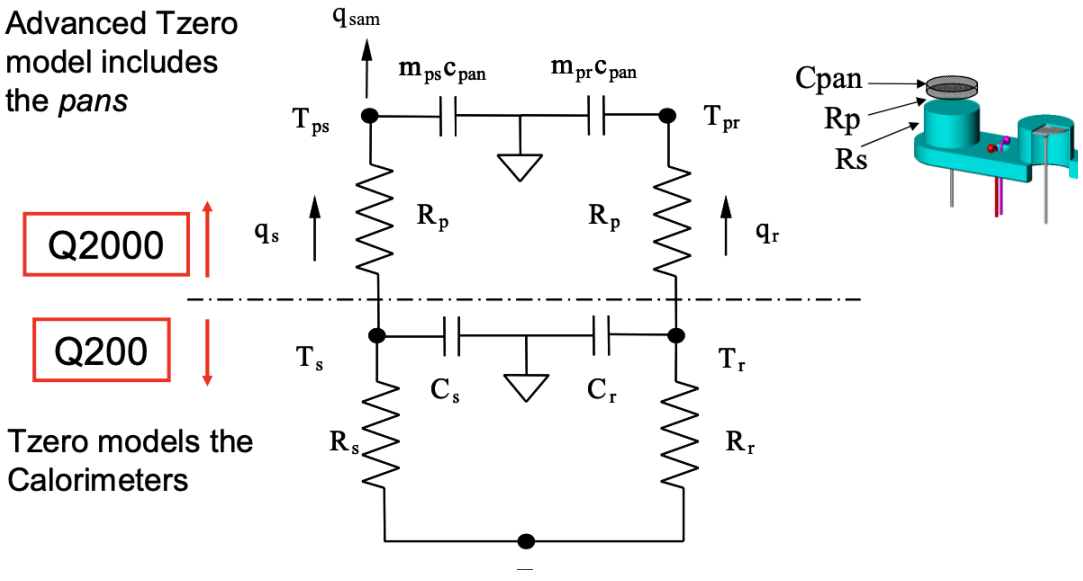

Figure 3-5 The different model used in DSC Q2000 and DSC Q200 (DSC Training Course)(http://www.nmt.edu/academics/mtls/faculty/mccoy/docs/dsc/ta_introduction_to_dsc2009.pdf#page=90&zoom=auto,-155,306)

The Q2000 experiments were conducted at Dr. Derick Rousseau lab (Toronto Metropolitan University) by Dr. Khakhanang Wijarnprecha (Yim). She prepared the pans and used the same DSC Method program as we used in Q100. The Methods are included in Appendix A.

3.2.2.1 Calibration and Procedures

For each DSC instrument, a calibration was performed before the analysis to ensure accurate and precise measurements. The DSC cell was cleaned by using a fibreglass brush, and dirt was removed with compressed air. To check for proper cleaning procedures and to ensure that there are no contaminants in the cell, an empty cell run was performed across a temperature range from -60 to 200 °C with a heating and cooling rate of 20 C°/min to eliminate any contaminants from previous experiments. If further cleaning was required, a cotton swab dipped in acetone was used to clean the cell, followed by another empty cell run to confirm the absence of contaminants. Cells that were still contaminated were burned out by heating them to 600 degrees Celsius with the lid open under airflow. In order to minimize the "first run effect" and to obtain a clean cell and a smooth baseline, an overnight cyclic empty cell test was performed.

Q Series™ Explorer Window, provided by TA Instrument, was utilized to set up, view, and control the experiment. The calibration process is carried out using DSC calibration Wizard in Q Series™ Explorer Window. Firstly, the heat flow measurement of the DSC is calibrated using the Sapphire standard by placing it in the DSC and running a heating cycle from the calibration software. The DSC should report a known heat flow value for

the Sapphire standard, usually 12.5 mW. If the reported heat flow value falls outside the acceptable range, the heat flow calibration factor in the software should be adjusted until the reported value matches the known heat flow value of the Sapphire standard.

To calibrate the temperature measurement of the DSC, the Indium standard is utilized by placing a small amount of it in the DSC and running a heating cycle from the calibration software. The DSC should indicate the melting point of Indium at 156.6°C. If the reported melting point is outside the acceptable range, the temperature calibration factor in the software should be adjusted until the reported value corresponds to the known melting point of Indium.

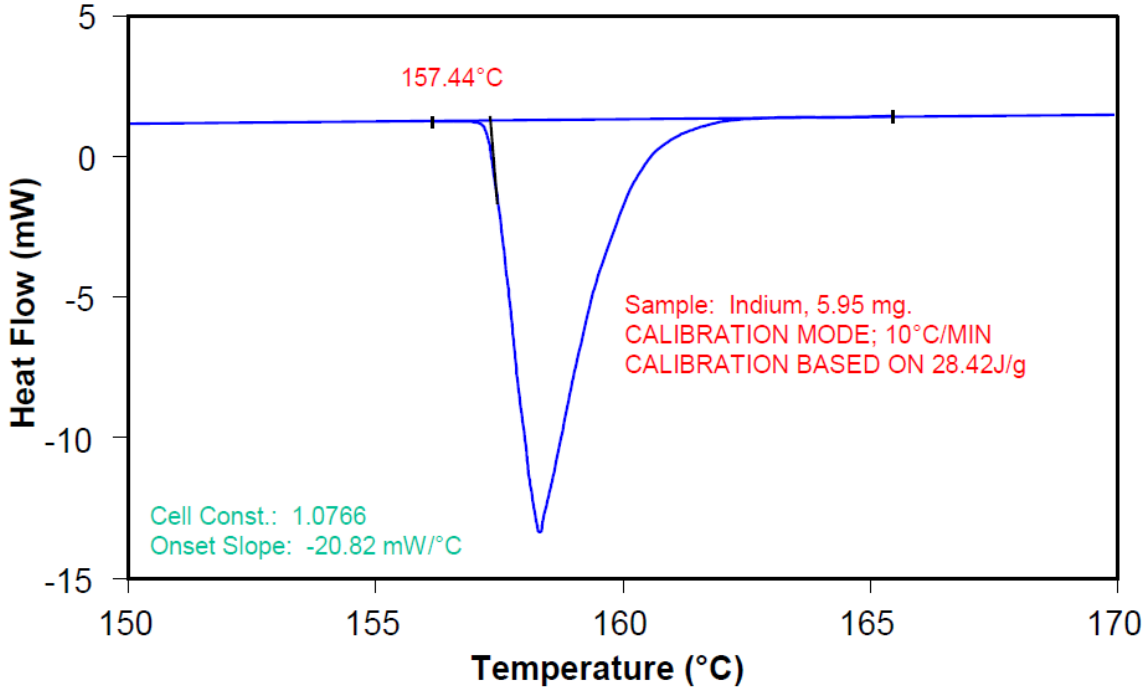

Figure 3-6 The third step of the calibration process: indium calibration (http://www.nmt.edu/academics/mtls/faculty/mccoy/docs/dsc/ta_introduction_to_dsc2009.pdf#page=90&zoom=auto,-155,306)

To conduct the experiment, the sample and reference pans were placed into the DSC cell. Prior to the experiment, the RCS and nitrogen gas were turned on for at least an hour to ensure a steady flange temperature reaches approximately -85 °C. The Method is programmed in Q Series™ Explorer; samples were first Isothermal for 7.00 min at 110 °C and then cooled down to -30 °C using 9 different cooling rates, 2.5 C°/min, 5.0 C°/min, 7.5 C°/min, 10.0 C°/min, 12.5 C°/min, 15.0 C°/min, 17.5 C°/min,, 20.0 C°/min,, and 25 C°/min,, and then heated to 110 °C at a heating rate of 10 C°/min, and held temperature for 7 minutes. SSS, however, was heated up to 120 °C because the melting point is above 70 °C.

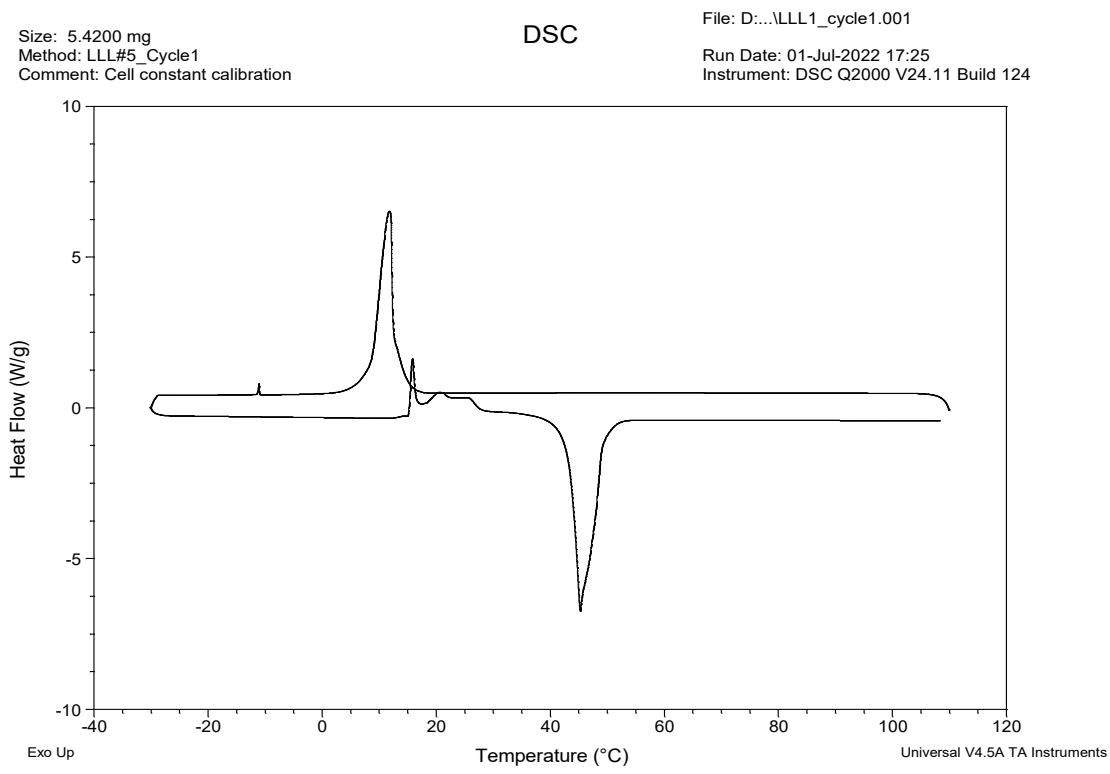

Figure 3-7 One cycle of LLL1_run1 in 15 C°/min, cooling rate and 10 C°/min, heating rate.

Three sample pans were prepared for each material, and each run consisted of 54 cycles, where each cycle included one heating ramp and one cooling ramp. Three runs were conducted for each sample pan, without taking the pan out to eliminate the pan position effect on the DSC Q100 signal. In summary, every sample pan performed 162 cooling and heating cycles, and three replicates were done for each material.

The sequence of cooling steps was randomized as shown in table 3-1. TA Instruments Analysis program was used to export the heat flow signal (W/g), temperature/time signal (C°/min), and first/second derivative of heat flow by using the option in the menu: View – Data table – Spreadsheets. A macro was written using TA instruments analysis software to generate the excel spreadsheet automatically.

Table 3-1 Method of cooling sequences of three LLL pans in the DSC experiment.

pans	LLL1			LLL2			LLL3		
Replicate	L1R1	L1R2	L1R3	L2R1	L2R2	L2R3	L3R1	L3R2	L3R3
	1	2	3	4	5	6	7	8	9
1	10	20	7.5	17.5	5	20	10	10	7.5
2	5	15	5	7.5	17.5	15	15	12.5	20
3	25	5	7.5	10	5	7.5	5	25	2.5
4	10	12.5	7.5	5	25	20	20	17.5	12.5
5	12.5	20	15	17.5	12.5	20	7.5	20	7.5
6	15	20	5	25	2.5	17.5	15	15	12.5
7	12.5	25	2.5	12.5	25	15	2.5	10	5
8	10	12.5	2.5	5	20	12.5	25	2.5	20
9	15	25	20	15	17.5	17.5	25	7.5	7.5
10	20	17.5	10	15	25	25	2.5	17.5	17.5
11	2.5	10	25	17.5	2.5	12.5	25	17.5	10
12	7.5	12.5	5	10	5	20	5	5	25
13	20	15	15	5	20	2.5	7.5	17.5	20
14	10	25	5	20	15	17.5	20	20	17.5
15	5	12.5	17.5	25	5	25	2.5	10	12.5
16	15	15	10	5	17.5	10	7.5	17.5	17.5
17	12.5	25	17.5	2.5	20	2.5	15	15	25
18	7.5	7.5	25	17.5	25	15	2.5	15	5
Time (hrs)	**12.49**	**10.79**	**13.73**	**12.62**	**12.91**	**12.02**	**14.53**	**11.77**	**12.24**
Total (hrs)	**37.01**			**37.55**			**38.54**		

3.2.2.2 DSC thermogram analysis

The TA Universal Analysis Software allows researchers to analyze the data obtained from these experiments. Some of the functions of TA Universal Analysis Software include reduce and manipulate raw data obtained from thermal analysis experiment; graphical representations of data, including temperature profiles, heat flow curves, interpret the data obtained from thermal analysis experiments to determine various material properties such as melting point, glass transition temperature, and thermal stability. It also includes the determination of onset point. This onset point, however, is relatively inaccurate because it is calculated as the intersection of the extension line from the liquid state and the tangent line of the crystallization process (shown in Figure 3-6). However, the onset temperature is actually the time/temperature at which the first point deviates from the heat flow baseline. Therefore, a MATLAB code was developed by the author to detect onset temperature. The full code is included in the Appendix B.

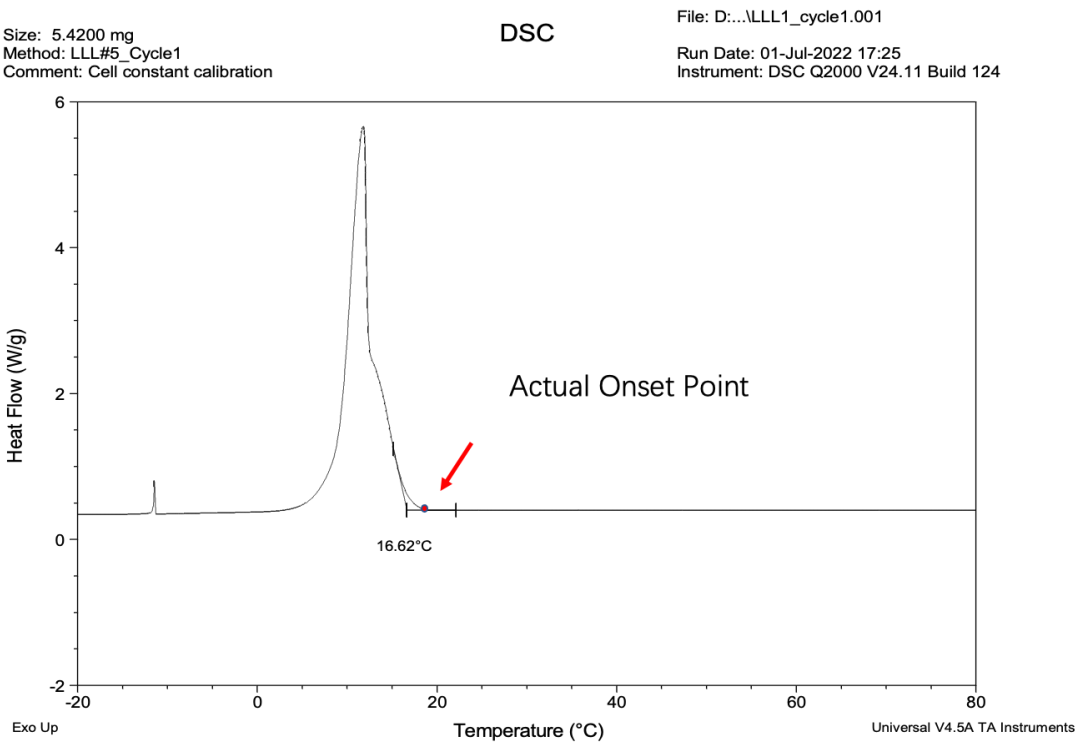

Figure 3-8 Onset point detection using TA Universal Analysis Software compared to the actual onset point

The MATLAB code is designed to analyze DSC data to obtain the onset temperatures of thermal events in a sample. The code takes an Excel file containing DSC data as input and provides output in the form of onset temperatures for each sheet in the Excel file.

The code starts by defining the temperature range for the TAG and the onset ranges for each sample. The onset ranges are determined by eye and are specific to each sample. The code then performs linear regression operations on the data and finds the slope and intercept of the linear fit. Next, the code identifies the onset temperature of the thermal event by searching for the point where the difference between the measured values and the linear fit exceeds a certain threshold, as shown in Figure 3-8. This threshold is calculated from the standard deviation of the difference between the measured values and the linear fit.

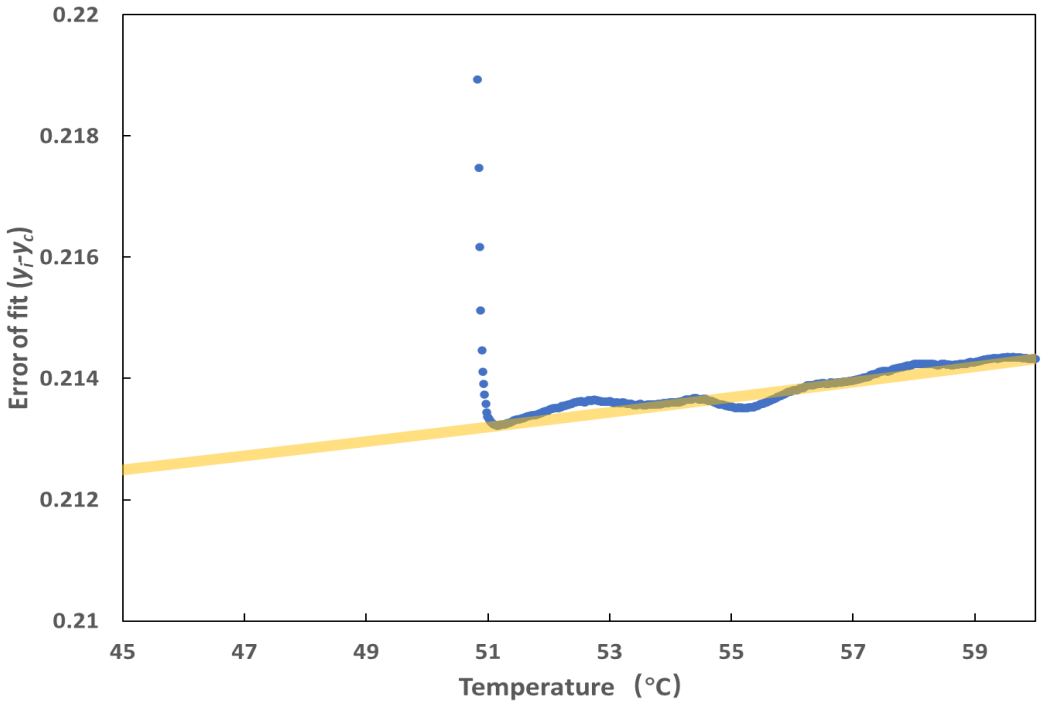

Figure 3-9 Plot of temperature verse error (blue) of linear fit (yellow) of the heat flow signal in the liquid state of SSS

The onset temperature is calculated based on the temperature range and onset range defined earlier. The code then outputs the onset temperature for each sheet in the Excel file. This MATLAB code automates the process of identifying the onset temperature of thermal events in DSC data, making it more efficient and less prone to human error. Figure 3-9 shows an example of the onset temperatures of LLL detected by the MATLAB code.

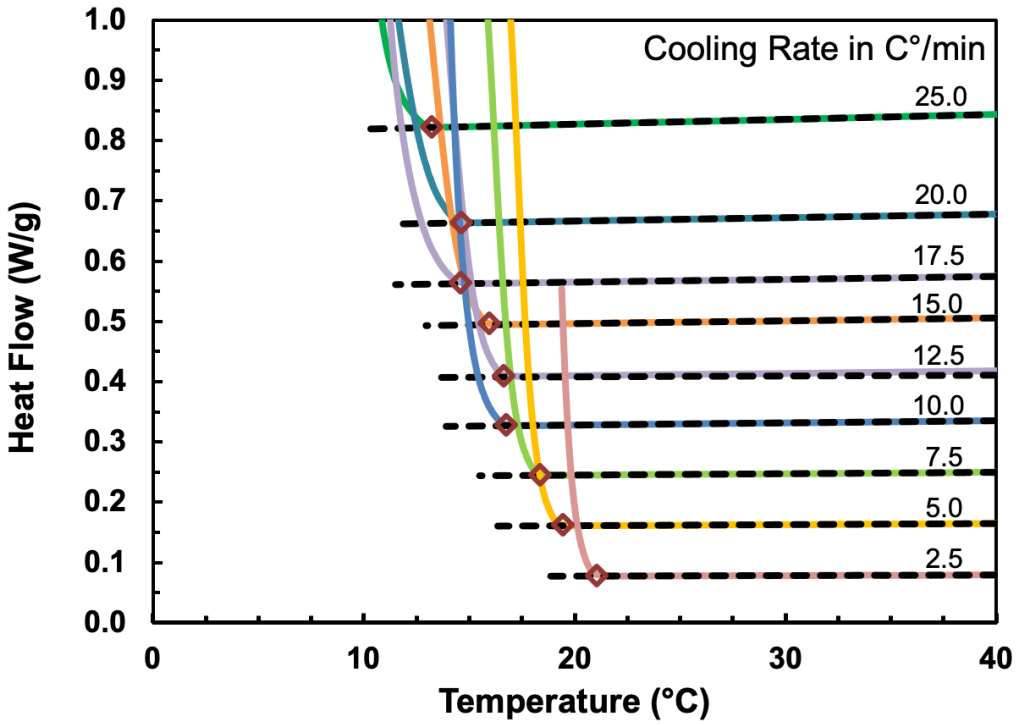

Figure 3-10 Onset temperature of LLL detected by the MATLAB code.

CHAPTER 4 RESULTS AND DISCUSSION – I EFFECT OF COOLING RATE ON THE ONSET TEMPERATURE IN PURE TRIACYLGLCERODES

4.1 Onset temperatures of crystallization

A differential scanning calorimetry (DSC) thermogram can be used to detect the onset of triacylglycerol (TAG) crystallization by estimating the temperature at which the exothermic peak starts.

Peak identification and interpretation were done after acquiring the DSC thermograms of the TAG samples. An exothermic peak indicates the crystallization of TAG, whereas an endothermic peak indicates the melting of TAG. The onset temperature is the temperature at which the exothermic peak begins to appear, since this is the temperature at which the TAG sample begins to crystallize. The composition of the sample, the cooling rate, and the presence of impurities can influence the onset temperature and the shape of the exothermic peak during TAG crystallization.

The analysis of DSC experimental results requires, first of all, that the instrument consistently controls the conditions across experiments. This is achieved by the programed method. To ensure accurate temperature and heat flow measurements, DSC instruments also need to be calibrated before each experiment.

Second, the sample should be homogeneous, and the sample mass should be within a narrow range. Samples should also be well encapsulated in a pan to prevent any contamination, and the mass of the reference pan and the empty sample pan should be chosen to have a no more than 0.5 mg mass difference.

Third, DSC thermograms should be corrected for baseline drift, which changes in instrument temperature or changes in heat flow in the reference plate can cause. It is necessary to identify and correct any artifacts or abnormalities before analyzing DSC data. Some unusual thermal events such as additional peaks, shoulders or changes in melting or phase transition temperature are often due to the presence of impurities in the samples. To determine if such events are anomalies or artificially caused, it is important to verify whether the thermogram baseline fluctuates during non-standard thermal events.

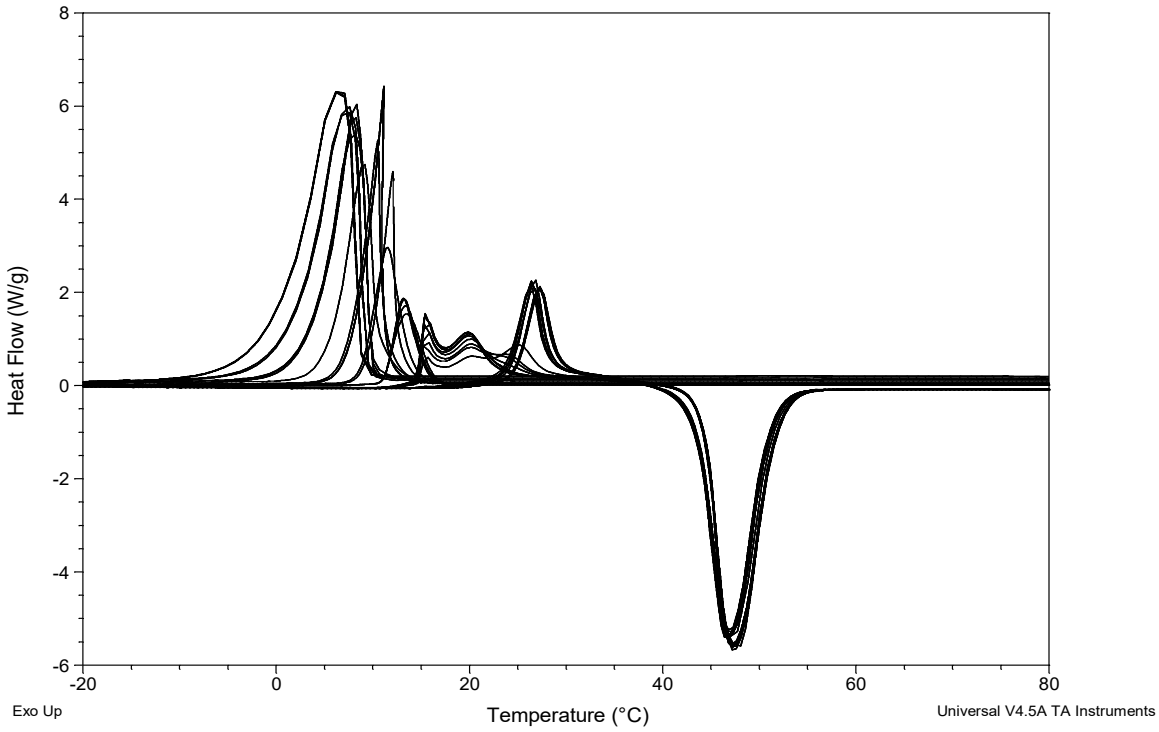

Figure 4-1 DSC thermograms showing the heat flow (Exo-up, W/g) as function of temperature (°C) for LLL cooled at the different cooling rates and followed by heating at 10 C°/min.

The MATLAB code was developed to process thermal analysis data in a more efficient and accurate way. The script reads data from an Excel file and performs linear regression and onset analysis on each sheet. Each sheet's name is written uniformly, with the first three characters representing the cooling rate and the last number representing the replicates. The variable sheet name contains the names of each sheet in the file, and the script loops over each sheet.

For each sheet, the script reads the data from the sheet using the 'xlsread' function and extracts the temperature, time, and heat flow data. The script then performs linear regression on a subset of the data with temperatures between a specific lower and upper temperature. This temperature range for the linear regression should include the onset temperature, thus, it should be maintained within a range of around 10 °C. The difference between the observed and predicted heat flow is calculated using the slope and intercept obtained from the linear regression. After the differences have been calculated, the standard deviation is used to identify the onset temperature of the thermal event.

The standard deviations obtained from experiments at fast cooling rates were larger than those for slow cooling rates. Therefore, when the onset temperatures were determined, the larger standard deviations produced more uncertainty in the onsets at fast cooling rates.

Since the stability of the heat flow signal is related to the temperature control system of the instrument, the faster the cooling rate is, the more difficult it is to maintain the temperature control of the system. Hence, the frequency of its fluctuation is more remarkable, which means that the heat flow signal of the liquid state will deviate

sometimes before the actual onset, resulting in different fitting errors in different time periods.

The onset temperature was defined in this work as the first temperature point where the heat flow is more than 10 × sigma above the predicted heat flow based on the linear regression model. In cases where the sigma is less than $n \times 10^{-05}$, the threshold for identifying the onset temperature is increased to n × sigma; n depended on the cooling rate. A matrix of cooling rate (CR), replicate number (REP), onset temperature sequence number (onset_index), onset temperature (onset_temp), heat flow at the onset temperature (hf(onset_index)), and standard deviation of the difference (sigma) is generated by the code.

In the left panel of Figure 4-2 the onset temperatures from one pan of LLL are shown as blue crosses to illustrate the variability of these estimates. The right panel shows the results of calculated deviation used to identify the onset temperature. Note that the scale was been expanded by $\sim 10^3$ illustrating the challenge of detecting the onset temperature. The blue line are the deviations, and the red diamonds are the onset temperatures. It took many iterations to define reasonable regions to estimate the onsets.

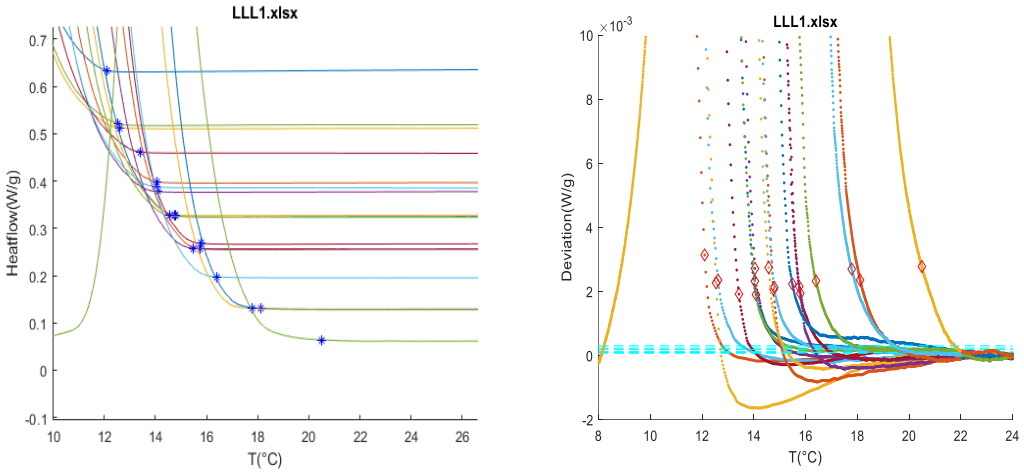

Figure 4-2 Two output figures from MATLAB code: DSC thermogram of LLL with the detected result onset temperature(left), the calculated deviation between fitting and original data as a criterion to detect onset temperature(right).

4.1.1 Onset temperature of pure triacylglycerols

Figure 4-3 (a) for LLL (b) for MMM and Figure 4-4 (a) for PPP and (b) for SSS show the onset temperature of the crystallization of the pure triacylglycerols at cooling rates (2.5, 5, 7.5, 10, 12.5, 15, 17.5, 20 and 25 C°/min); three replicated pans were made for the same pan type and similar weight (sample and pan ±1 mg). Each point represents an onset temperature detected using the MATLAB program.

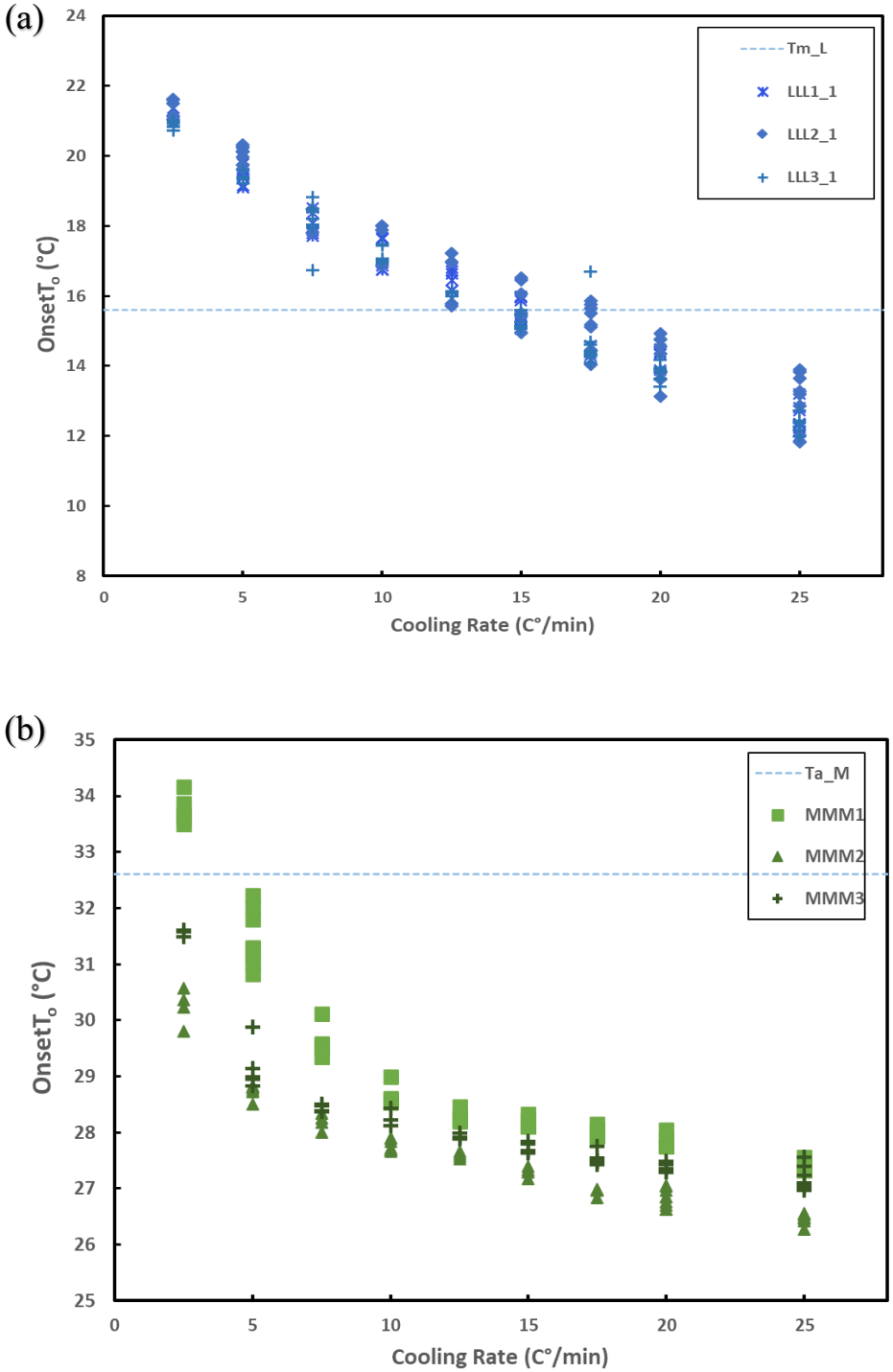

Figure 4-3 Onset temperatures plotted as a function of cooling rate of four pure triacylglycerols: LLL(a), MMM(b); three replicated pans using the same type of pan and instrument are included in this figure

The onset temperatures for PPP and SSS in Figure 4-4 show a linear relationship between onset temperature and cooling rate. The difference between the average value of onset temperature of 25 C°/min and 2.5 C°/min is 1.86 ± 0.13°C for PPP and 1.78 ± 0.17 °C for SSS. These differences are 8.01 ± 1.43 for LLL and 5.49 ± 1.66 for MMM. The variation of PPP and SSS under each cooling rate is relatively minor compared to LLL and MMM, which means that the smaller the triacylglycerol molecule is, the more it is affected by the cooling rates.

There is another notable difference between the trends of the onset temperatures of LLL and MMM and the trends of PPP and SSS. The onset temperatures of PPP and SSS in figure 4-4 are below the melting point of the α polymorph for all cooling rates, that ranged from 2.5-25 C°/min. However, for LLL and MMM shown in Figure 4-3, the crystallization event at slower cooling rates starts at a temperature higher than the melting point of the α polymorph. It is therefore reasonable to consider that LLL and MMM form another polymorph instead of α. However, this hypothesis needs to be supported by other evidence, such as non-isothermal X-ray experiments that can be used to investigate and identify polymorphic forms.

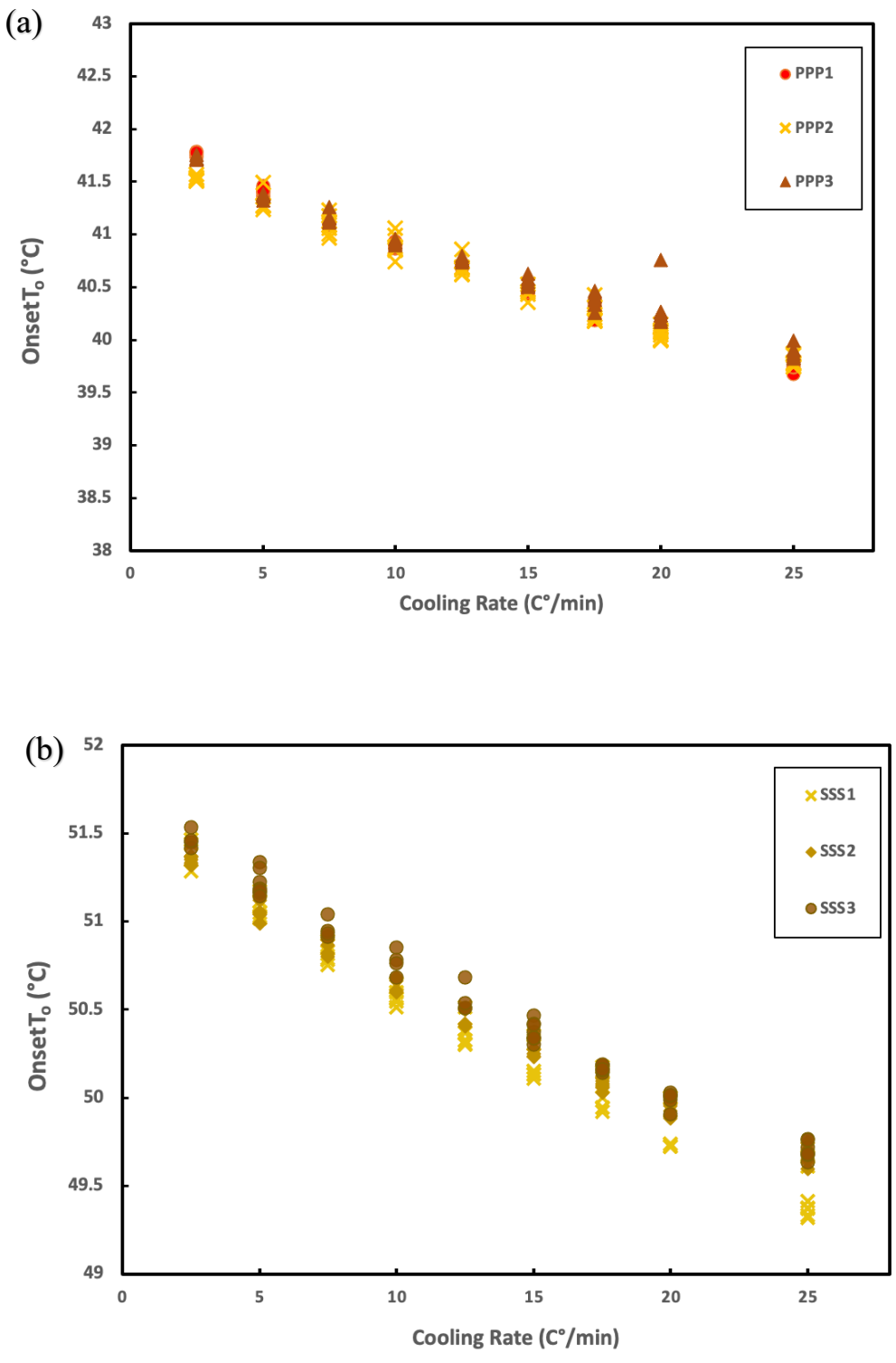

Figure 4-4 Onset temperature plotted as a function of cooling rate of four pure triacylglycerols: PPP(a), SSS(b); three replicated pans using the same type of pan and instrument are included in this figure.

Table 4-1 The average and standard deviation values of onset temperatures of the crystallization in LLL, MMM, PPP, and SSS. And the total number of measurements from the three pans are shown in the table.

	Cooling Rate (C°/min)	*25.0*	*20.0*	*17.5*	*15.0*	*12.5*	*10.0*	*7.5*	*5.0*	*2.5*
LLL	*Average(°C)*	9.87	11.06	11.66	12.60	13.02	13.75	14.74	15.77	17.88
	σ(°C)	0.91	1.01	0.44	0.60	0.31	0.41	0.65	0.63	1.10
	measurements	21	21	21	20	15	15	15	20	14
MMM	*Average(°C)*	26.63	27.23	27.52	27.82	27.97	28.16	28.77	28.76	32.12
	σ(°C)	0.57	0.42	0.43	0.38	0.29	0.43	0.66	0.40	1.56
	measurements	21	21	21	20	15	15	15	17	14
PPP	*Average(°C)*	39.81	40.15	40.29	40.49	40.72	40.91	41.12	41.38	41.67
	σ(°C)	0.07	0.16	0.09	0.06	0.07	0.07	0.08	0.07	0.11
	measurements	20	21	21	20	15	15	15	20	14
SSS	*Average(°C)*	49.61	49.91	50.10	50.29	50.43	50.65	50.87	51.12	51.39
	σ(°C)	0.15	0.11	0.08	0.10	0.11	0.09	0.07	0.10	0.07
	measurements	21	21	21	20	15	15	15	20	14

4.2 Comparative summary of onset temperatures of crystallization events

By comparing the tendency of the onset temperature of the four pure triacylglycerols, it is possible to interpret the behaviour of nucleation and reveal the relationship between cooling rate and polymorphism, as well as the effect of the size of the pure triacylglycerol molecule. As shown in Figure 4-5, there is an inverse relationship between the onset temperature and the cooling rate. As the cooling rate increases, the onset temperature decreases. The onset temperature, which depends on the nucleation rate, changes in a consistent and predictable manner. Since PPP and SSS seem to form the same polymorph over a cooling rate range of 2.5-25 C°/min, the time required decreases linearly for this polymorph as the cooling rate increases.

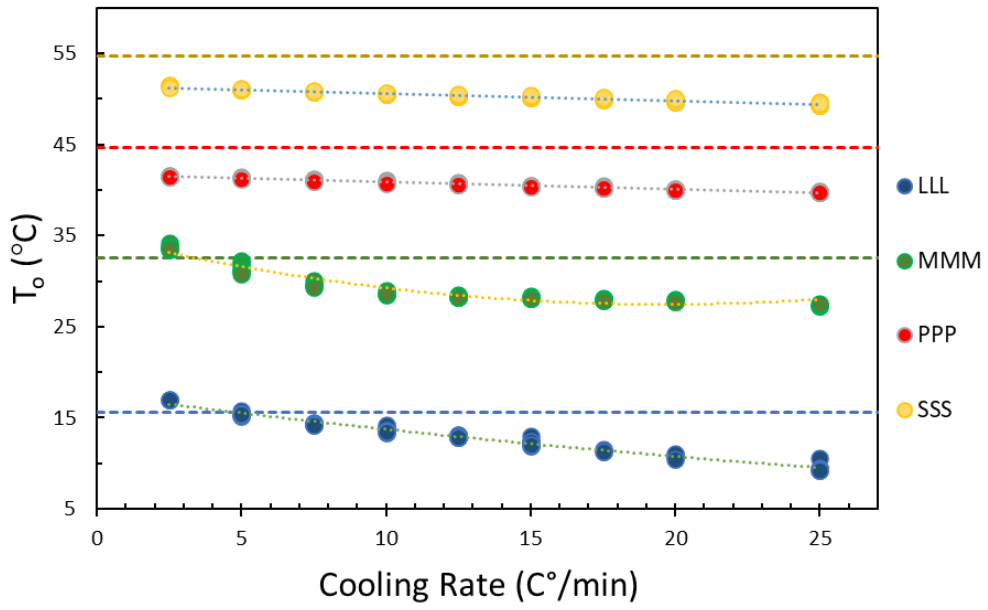

Figure 4-5 The plot of onset temperature with respect to cooling rate (C°/min) of LLL, MMM, PPP and SSS, and the dotted line represents the experimental melting point of α polymorph of each pure material.

For LLL, an almost linear relationship is seen between the cooling rate and onset temperature. However, the slope of pan 1 of LLL, for instance, is 0.306 ± 0.007, which is much steeper compared to PPP (0.080 ± 0.002) and SSS (0.082 ± 0.002). The values are summarized in the Table 4-2 and Table 4-3. These differences may be due to the formation of α in PPP and SSS, while for LLL the first polymorph is β'. We calculated the difference between the onset temperature and the melting temperature of α and β' polymorphs, ΔT_α and $\Delta T_{\beta'}$, the undercooling of α and β', which are proportional to the driving force of the crystallization. In Figures 4-6 and 4-7, the variables $-\Delta T_\alpha$ and $-\Delta T_{\beta'}$ is plotted as the function of the cooling rate.

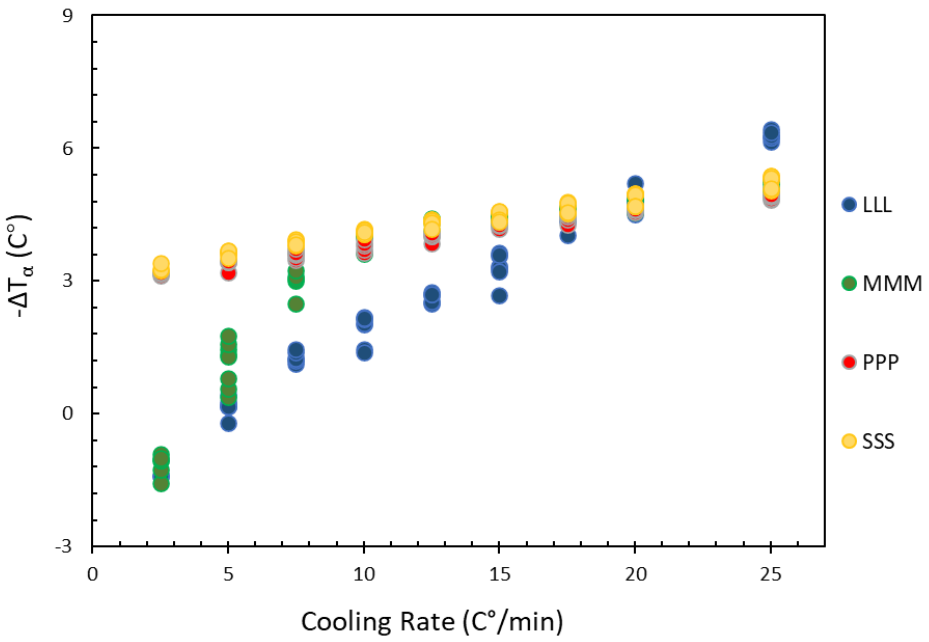

Figure 4-6 $-\Delta T_\alpha$ the difference between the onset temperature and the experimental melting temperature ($T_o - T_\alpha$) of the pure samples as a function of cooling rate.

Table 4-2 Linear fitting parameter of $-\Delta T_{\alpha}$ as function of cooling rate. Se stands for standard error.

	LLL	MMM	PPP	SSS	MMM (25-10)	MMM (10-2.5)
Slope k	0.306	0.265	0.080	0.082	0.076	0.686
Se_k	0.007	0.021	0.002	0.002	0.005	0.037
Intercept b	-1.308	0.028	3.010	3.248	3.275	-2.530
Se_b	0.109	0.292	0.027	0.033	0.079	0.238
Se_y	0.363	1.013	0.090	0.106	0.122	0.481
R^2	0.971	0.749	0.975	0.965	0.887	0.941

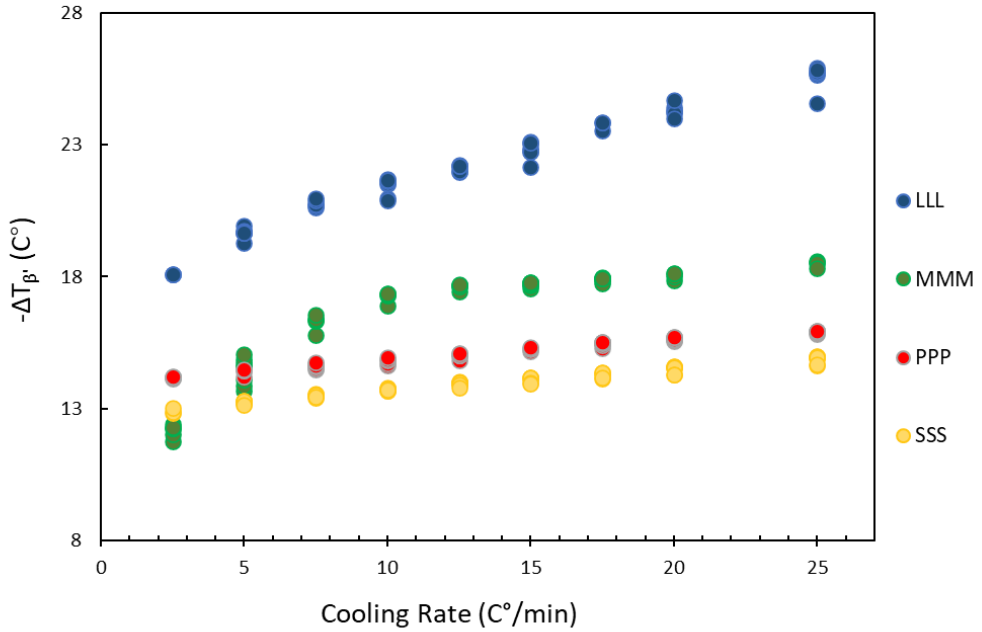

Figure 4-7 $-\Delta T_{\beta'}$ the difference between the onset temperature and the experimental melting temperature ($T_o - T_{\beta'}$) of the pure samples as a function of cooling rate.

Table 4-3 Linear fitting parameter of $-\Delta T_{\beta'}$ as function of cooling rate

	LLL	MMM	PPP	SSS	MMM (25-10)	MMM (10-2.5)
b	18.192	13.328	14.010	12.848	16.575	10.770
Se_b	0.109	0.292	0.027	0.033	0.079	0.238

The slope of the LLL series data points in Figure 4-7 is much larger than that of PPP and SSS, whereas the slopes of PPP, SSS, and part of the MMM data (cooling rate from 10 to 25 C°/min) are similar. On the other hand, the LLL data and MMM data in Figure 4-7 have larger slope at cooling rates from 2.5 C°/min to 10 C°/min. LLL and MMM then form similar polymorphs at cooling rates from 2.5 C°/min to 10 C°/min. While the polymorph formed by MMM for cooling rates between 10 C°/min to 25 C°/min is similar to PPP and SSS. In order to determine what polymorphic states, form under our experimental conditions and whether there is a phase transition, it is necessary to analyze the X-ray data and compare them with DSC thermograms.

Figures 5-8 depict the enthalpy values of LLL, MMM, PPP, and SSS as a function of the cooling rate. It is noteworthy that only LLL exhibits a distinct trend, whereas the enthalpies of MMM, PPP, and SSS remain relatively unaffected by variations in the cooling rate. These observations emphasize the unique behavior of LLL in response to the cooling rate, suggesting a potentially different underlying mechanism compared to MMM, PPP, and SSS.

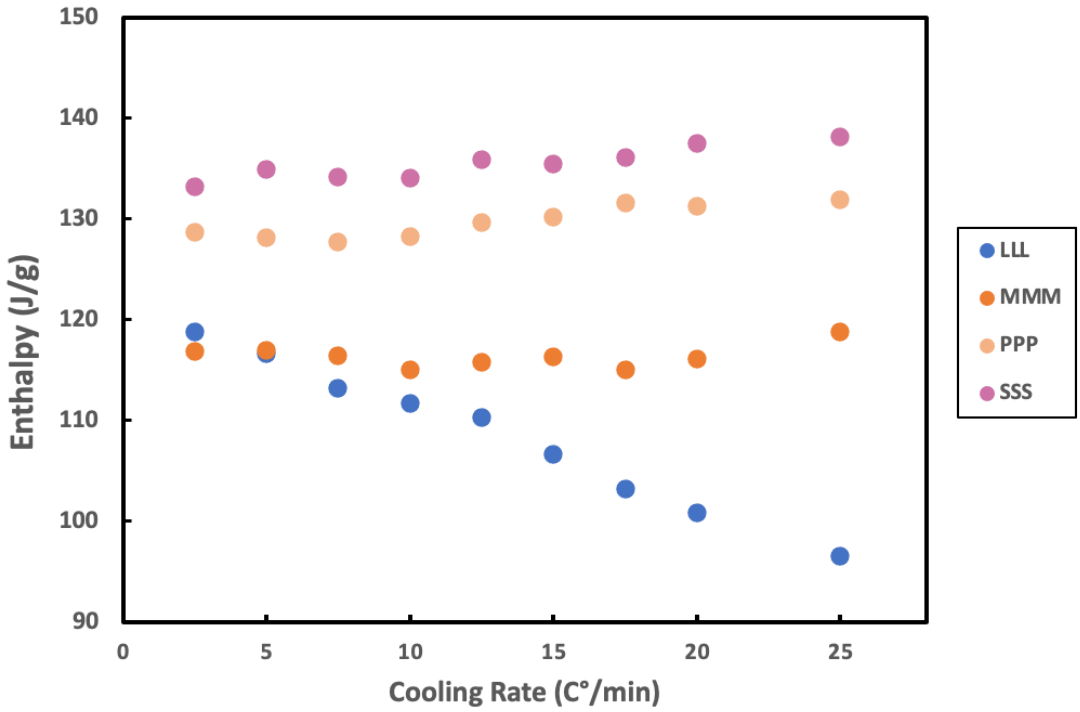

Figure 4-8 The enthalpy value of LLL, MMM, PPP, and SSS is plotted as a function of cooling rate

4.3 Instrumental impact on the onset temperatures of crystallization events

To verify the consistency and accuracy of the onset temperature data, we conducted a comparative study of LLL using DSC Q2000 and a premium hematic aluminum pan. The experiments conducted with different samples/containers/instruments provide varying ranges of estimated onset temperatures. One important aspect is the contact surface between the pan and the cell post. When heat flows across different surfaces, the thermal contact resistance changes. Heat flows to and from the sample are more accurately calculated using DSC Q2000 because its software accounts for sensor and pan imbalance effects, which is the mass difference between the reference pan and

the sample pan. DSC Q2000 calculates smaller thermal effects than Q100 due to the software explained in section 3.2.2.1. Moreover, premium hermetic aluminum pans are more uniformly manufactured and made from thicker material than regular hermetic aluminum sample pans, resulting in improved consistency.

Figure 4-9 shows three sets of onset temperatures data, with their means and confidence intervals obtained from LLL encapsulated in the premium hermetic pan performed in DSC Q2000, the premium hermetic pan performed in DSC Q100, and the standard hermetic pan performed in DSC Q100. Although they have different numerical values, the trend has not changed but has shifted vertically. That is, although the values of the onset temperature estimated by different equipment may vary, they follow the same trend with respect to the cooling rate.

Heat flux DSC uses a furnace that controls the temperature of the sample and reference pans. The temperature difference between the sample and reference pans is measured as a function of time or temperature. The temperature of the furnace or block is typically controlled using a feedback loop, in which the temperature controller adjusts the power to the heater to maintain a constant temperature. The temperature controller receives input from a temperature sensor, which is located near the sample and reference pans to measure the actual temperature. A pan with good thermal conductivity will help transfer heat in and out of the sample efficiently, while a pan with low thermal mass will allow for rapid temperature changes. The higher the thermal conductivity of the material and the lower the thermal mass will reduce experimental error.

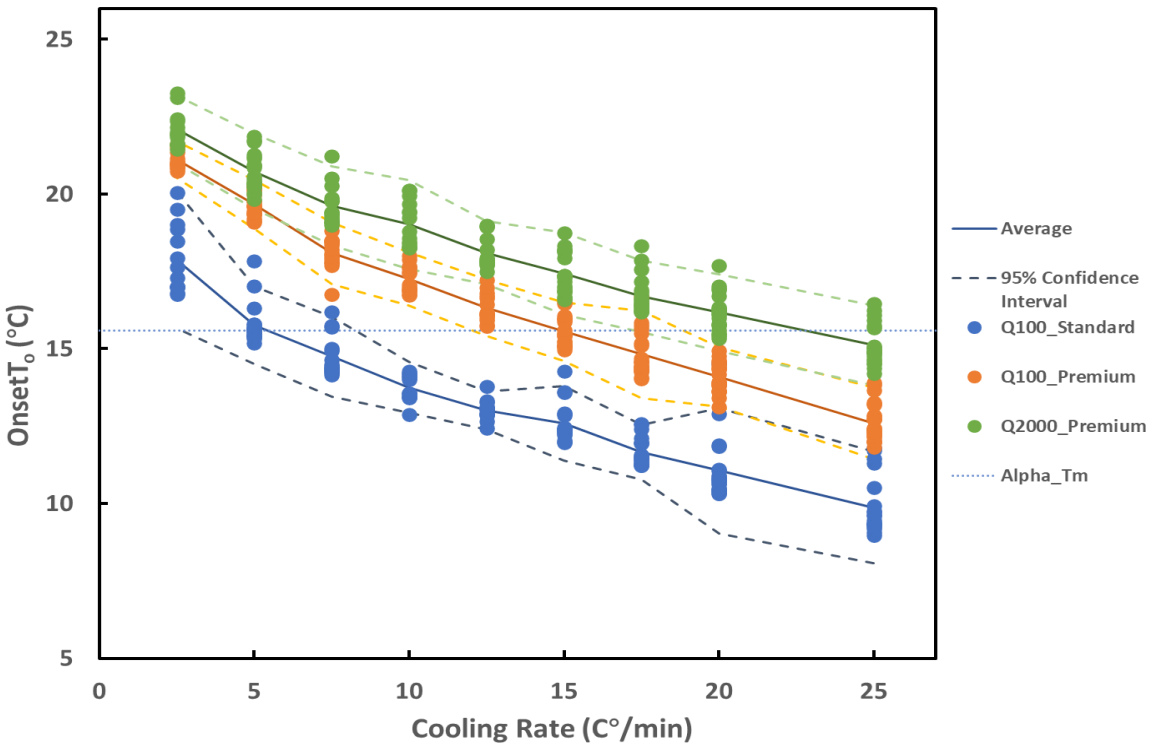

Figure 4-9 Comparison of the onset temperature data of LLL conducted in DSC Q100/Q2000, using the premium/standard hematic aluminum pan.

Another comparison of the effect of using different types of pans was performed for the MMM and its results are illustrated in Figure 4-10. The data were compared using a Tzero pan at cooling rates ranging from 1 C°/min to 20 C°/min, and both sets of data showed the same pattern. For the noticeable difference between the data at 2.5 C°/min and 5 C°/min cooling rates, there is a possibility that the difference is due to the pan position, or that the cooling rate interval is at a critical value for the two polymorphs. More experiments are needed to verify or explore this hypothesis.

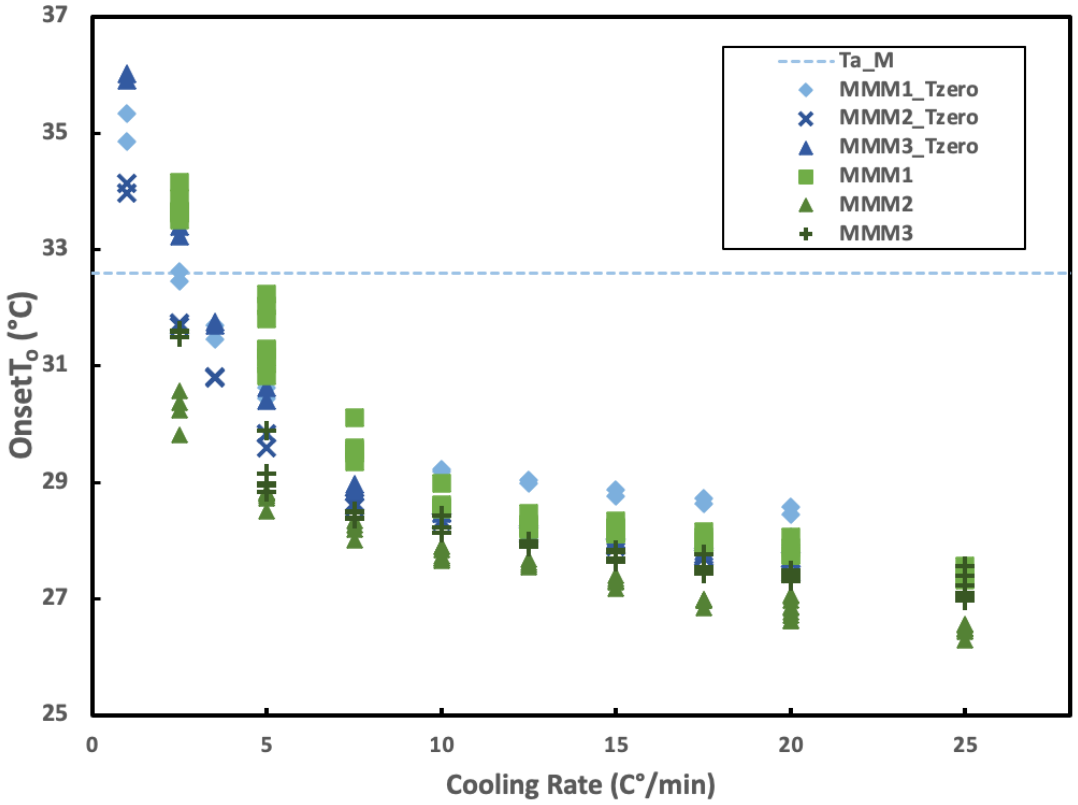

Figure 4-10 Comparison of the onset temperature data of MMM conducted in DSC using the Tzero/standard hermetic aluminum pan.

CHAPTER 5 RESULTS AND DISCUSSION– II POLYMORPH IDENTIFICATION USING X-RAY AND DSC THERMOGRAM OF LLL AND MMM

5.1 DSC thermogram analysis

Differential Scanning Calorimetry (DSC) thermograms provide information about the thermal behaviour of a sample as a function of temperature or time. Heat absorption and exothermic events, such as melting points, related to phase changes, are detected by DSC by measuring the heat flow into or out of samples as they heat or cool. The enthalpy changes associated with a phase change are measured by the integral value of the heat absorption or exothermic peaks. Therefore, DSC can be used to study crystallization kinetics. A crystallization peak can provide insight into the phase change by analyzing its shape and position.

Table 5-1 The melting enthalpy value and the melting temperature of LLL, MMM, PPP, SSS and their polymorphic form (Marangoni & Wesdorp, 2013)

	α		**β'**		**β**	
	ΔH_m (kJ/mol)	T_m (°C)	ΔH_m (kJ/mol)	T_m (°C)	ΔH_m (kJ/mol)	T_m (°C)
LLL	69.8	15.6	86	35.1	122.2	45.7
MMM	81.9	32.6	106	45.9	146.8	57.1
PPP	95.8	44.7	126.5	55.7	171.3	65.9
SSS	108.5	54.7	156.5	64.3	194.2	72.5

Figure 5-1 and Figure 5-2 show the DSC crystallization thermograms and the following reheating at 10 C°/min. During the cooling process, there is a sudden release of heat as the sample crystallizes. The peak on the crystallization thermogram corresponded to the energy released during the crystallization process. The peak area

is proportional to the degree of crystallization and the peak crest temperature corresponds to the temperature at which the maximum crystallization rate. Figure 5-1 shows that the crystallization peaks of LLL for cooling rates from 2.5-17.5 C°/min have very irregular shapes. A shoulder appears as a smaller peak that is located adjacent to a larger peak, which indicates that there must be more than one polymorph, and that a coexisting crystallization event happened. In the previous chapter, a conjecture was proposed through the analysis of the crystallization onset temperature: LLL may first crystallize β' polymorph instead of α polymorph during the cooling process because the initial temperature of crystallization is higher than the melting point of α polymorph. The position and shape of the of the crystallization peaks after these onsets provide additional indirect evidence for this conjecture.

Although there is no apparent shoulder or bump on the crystallization peak for cooling rate 20 and 25 C°/min, it does not mean that the coexisting crystallization event does not occur. It is possible that it happens too rapidly or in such a small proportion that the DSC thermogram is unable to capture it. Therefore, we need X-ray experiments to verify the polymorph formation sequence and the formation ratio under the same non-isothermal conditions.

The reheating thermogram shows the heating of the sample to its original temperature at a constant rate after crystallization. The peaks on the reheating temperature graph represent the energy absorbed or released during the reheating process. When a pure solid triacylglycerol is heated, it may recrystallize into a more stable polymorph. During heating a metastable polymorph, it may melt and the liquid will recrystallized into a more stable polymorph. The metastable polymorph may also transition directly

in a solid state, although this is more difficult. The exact nature of the crystallization behavior will depend on the specific polymorphic form of the triacylglycerol. Since triacylglycerols exhibit multiple polymorphic forms, then the heating process may result in several transitions from one polymorphic form to another. Triacylglycerols exhibit different melting or crystallization behaviour depending on its crystal structure. Multiple melting-recrystallization peaks can be observed in DSC thermograms at different temperatures, each of which corresponds to a different polymorph. Because the enthalpy of fusion is higher in a more stable polymorph, the melting peak of a more stable polymorph is always more prominent than the melting peak of a metastable polymorph.

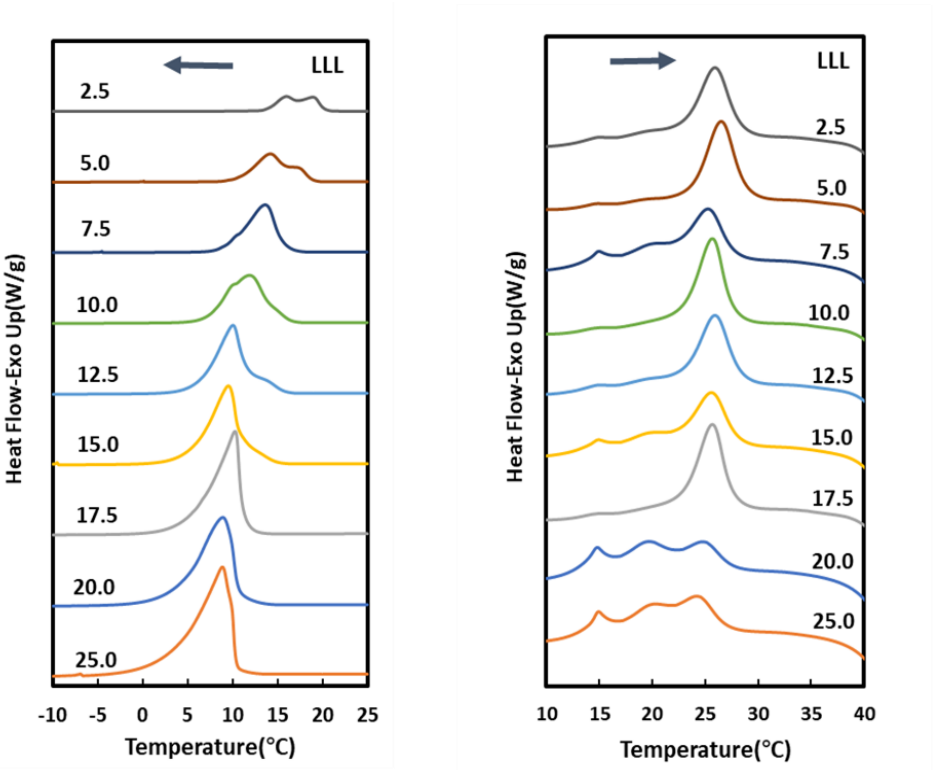

Figure 5-1 DSC crystallization thermograms (left) and the subsequent reheating (right) in 10 C° /min of LLL, with the label representing the cooling rate (C° /min)

The MMM thermogram in Figure 5-2 reveals a single crystallization event occurring between the temperature range of 7.5 C°/min, to 25C°/min. During the reheating process, melting and over-crystallization were observed at all cooling rates, with the degree of over-crystallization being relatively minor at 2.5 C°/min, and 5 C°/min, cooling rates. However, a recrystallization process was observed immediately after cooling at a rate of 2.5 C°/min, at approximately 45 °C, with a similar process observed at 5 C°/min, but to a lesser extent. The behavior observed in both the crystallization and reheating peak is identical in the cooling rate from 7.5 C°/min to 25 C°/min. However, reducing the rate of temperature change to 2.5 C°/min, resulted in an earlier crystallization event and the detection of a double peak. Although there was no clear double peak observed in the thermogram at a cooling rate of 5 C°/min, the subsequent melting curve differed from those obtained at other cooling rates. These observations suggest that two different crystal structures may have formed during the crystallization process, leading to distinct behavior during the melting process. Additional experiments can be conducted to analyze the crystal structures and properties of the sample at different cooling rates to further understand the impact of cooling rates on the crystal behavior of the sample.

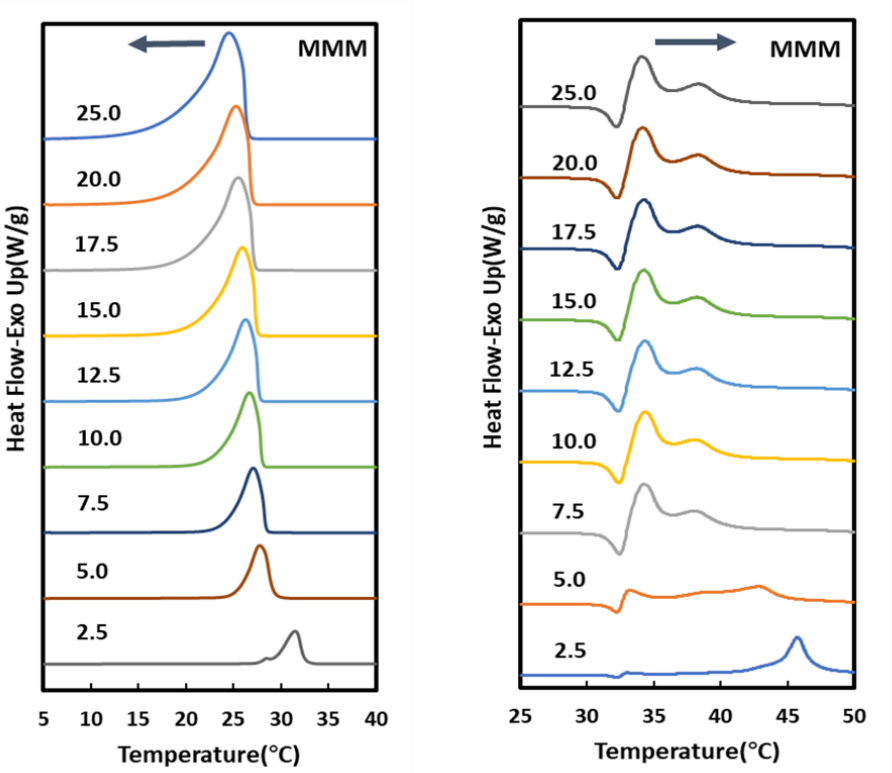

Figure 5-2 DSC crystallization exo-up thermograms (left) and the subsequent reheating (right) in 10 C° /min of MMM, with the label representing the cooling rate (C° /min)

In a thermogram, the heat flow rate is calculated by taking the derivative of the heat flow signal with respect to time. It provides information about how quickly the temperature of the sample is changing at any given time. This is because the DSC estimates the heat flow from the difference in temperature between the reference and the sample. The heat flow rate is very useful to identify any thermal events that may not be easily visible in the raw thermogram. By analyzing the rate at which the temperature changes, it is possible to detect small changes in the sample's thermal behavior that may not be apparent from the heat flow signal alone.

In Figure 5-3 and 5-4 the derivates of heat flow with respect to temperature are plotted as a function to temperature for different cooling rates. Between 17.5 and 25 C° /min,

there is no clear shoulder or bump observed on the crystallization peak in the thermogram. However, on the differential plot, there is a noticeable bump at around 10 °C, indicating an abrupt turn in the heat flow rate. This suggests the possibility that two polymorphs could have grown together within this cooling rate range. This phenomenon could be caused by the competition between the two polymorphs during crystallization, resulting in the growth of two different crystal structures.

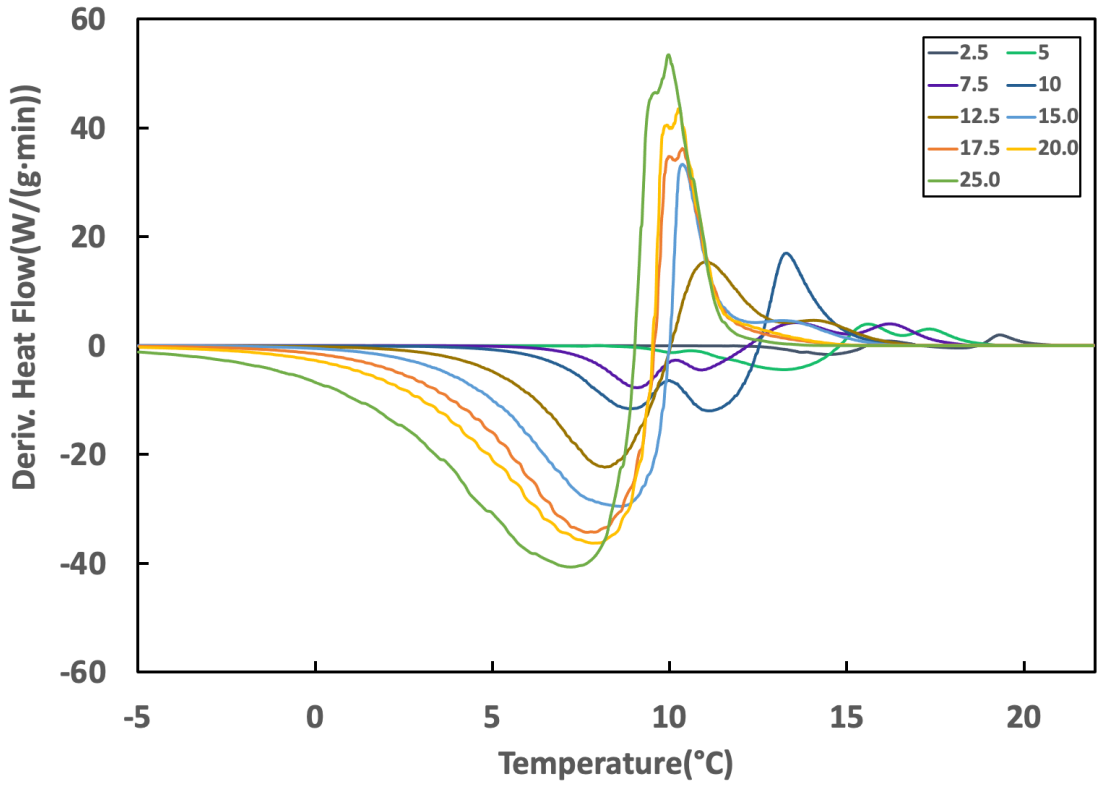

Figure 5-3 The derivative of heat flow with respect to time (W/(g·min)) versus temperature (°C) from LLL under nine cooling rates

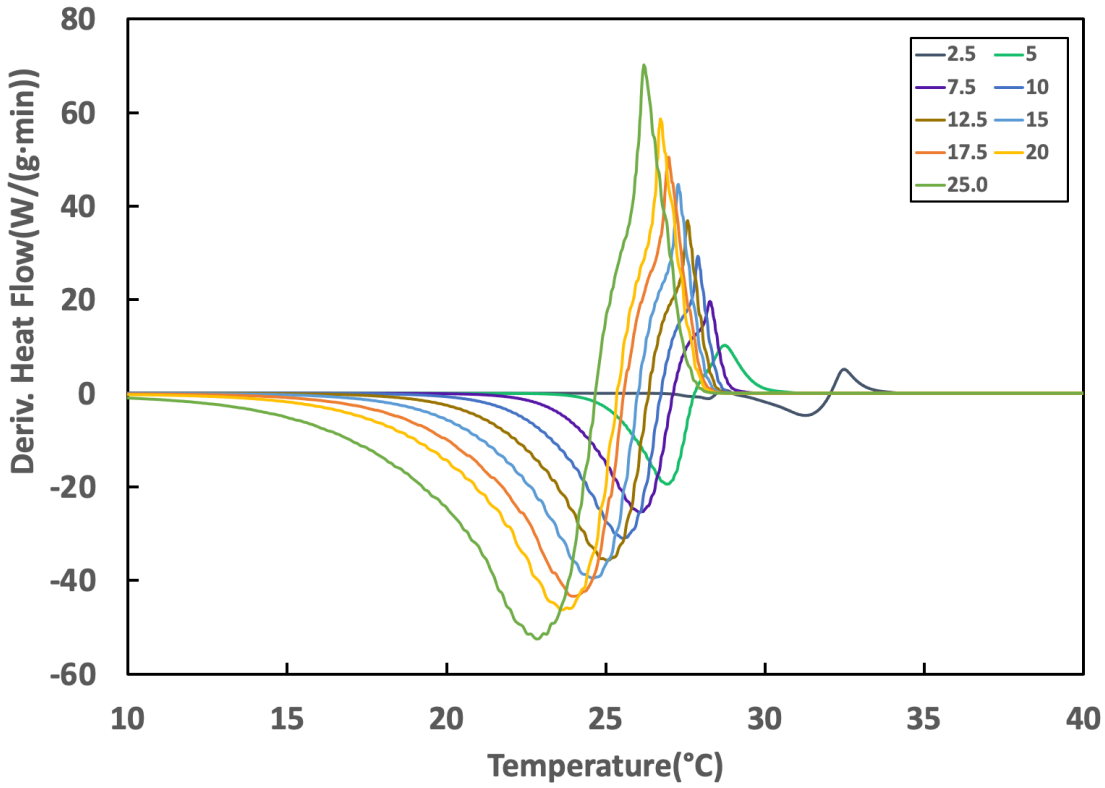

Figure 5-4 The derivative of heat flow with respect to time (W/(g·min)) versus temperature (°C) for MMM under nine cooling rates

5.2 X-ray (SAXD and WAXD) analysis

X-ray diffraction patterns are commonly used to identify the polymorphic forms of a material and to distinguish between ambiguous cases of polymorph identity. To identify the polymorphic forms during cooling at different rates, X-ray diffraction patterns were obtained and analyzed. After analyzing the collected data, it was possible to assign each peak to a specific polymorphic form, from previous experience and literature. This process was further verified by WAXD analysis, which provided additional evidence to support the identified forms. The combination of SAXD and

WAXD analysis allowed for a comprehensive understanding of the polymorphic forms present in the samples during cooling and melting.

The three basic polymorphs of the material were identified and distinguished by their distinct wide-angle diffraction patterns. Specifically, the α-phase exhibited a single strong peak corresponding to a d-spacing of 0.42 nm. The β' -phase showed two strong peaks corresponding to d-spacings of 0.42 and 0.38 nm, while the β-phase showed three peaks corresponding to d-spacings of 0.46, 0.39, and 0.38 nm. The process of obtaining standard dynamic small-angle and wide-angle X-ray diffraction patterns required capturing a sequence of 2D diffraction patterns obtained at fixed time intervals while the sample went from the liquid phase to the conclusion of the cooling process. Figures 5-5 and 5-6 depict the intensity of X-ray as a function of X-ray scattering vector, as the temperature is decreased. The crystal phase formation of LLL can be observed from SAXD and WAXD, respectively, during the cooling process at a rate of 20 C°/min, and 15 C°/min. The observation was carried out from the initial cooling phase in the liquid state until the end of cooling. Both cooling rates demonstrate a consistent pattern of the emergence of the β' phase preceding that of α formation in LLL. Additionally, the WAXS pattern confirmed the formation of both α and β' phases during the cooling process, and the formation of the β' phase first, followed by the formation of the α phase.

Table 5-1 Lamellar distance (nm) and short spacing (nm)of LLL and MMM determined by x-ray diffraction (Takeuchi et al, 2003)

	LLL			MMM		
	α	β'	β	α	β'	β
LD (nm)	3.5	3.2	3.1	4.1	3.7	3.6
SS (nm)	0.42	0.42	0.46	0.42	0.42	0.46
		0.38	0.39		0.38	0.39
			0.38			0.38

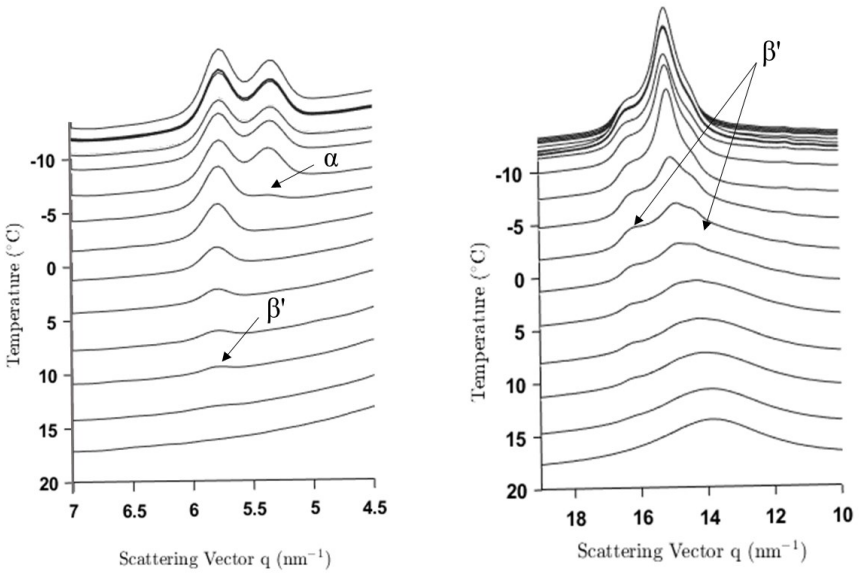

Figure 5-5 X-ray diffraction intensity as a function of scattering vector at different temperatures for LLL during cooling at 20 C° /min from the melt at 70 °C to -10 °C. The left panel shows the SAXD from the (003) plane of the long spacing. The WAXD from the short spacings is shown on the right. The β' and α characteristic peaks are indicated by the arrows, showing β' appearing before α.

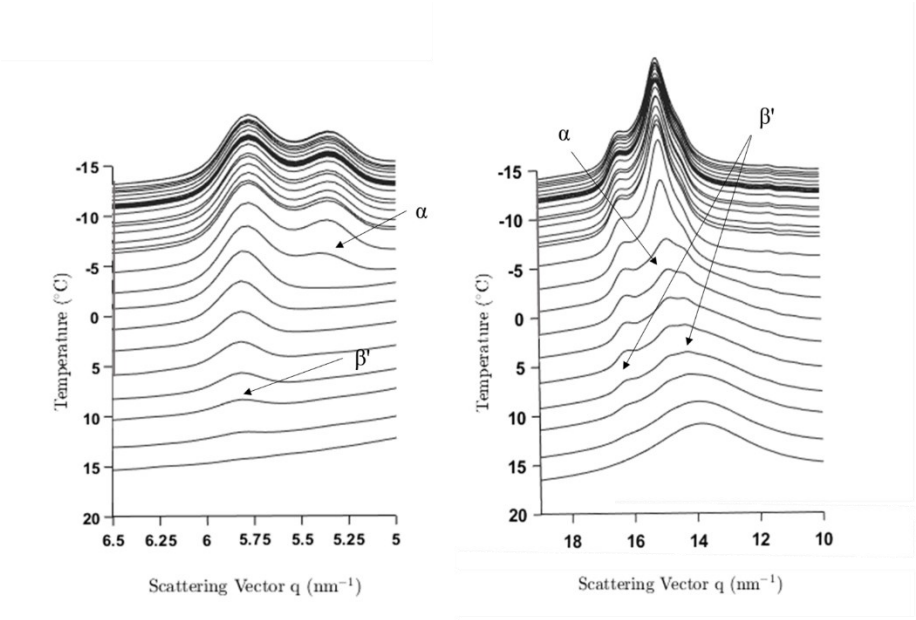

Figure 5-6 X-ray diffraction intensity as a function of scattering vector at different temperatures for LLL during cooling at 15 C° /min from the melt. The left panel shows the SAXD from the (003) plane of the long spacing. The WAXD from the short spacings is shown on the right. The β' polymorph appears before the α polymorph.

Figures 5-7 and 5-8 illustrate the SAXD and WAXD patterns of MMM during the crystallization process, cooled at rates of 20 C°/min and 15 C°/min, respectively. As observed in LLL, the crystallization of MMM also started with the formation of the β' polymorph followed by the α polymorph. This finding not only sheds light on the commonality between the two materials but also provides insights into the fundamental mechanisms of polymorphic transitions during crystallization.

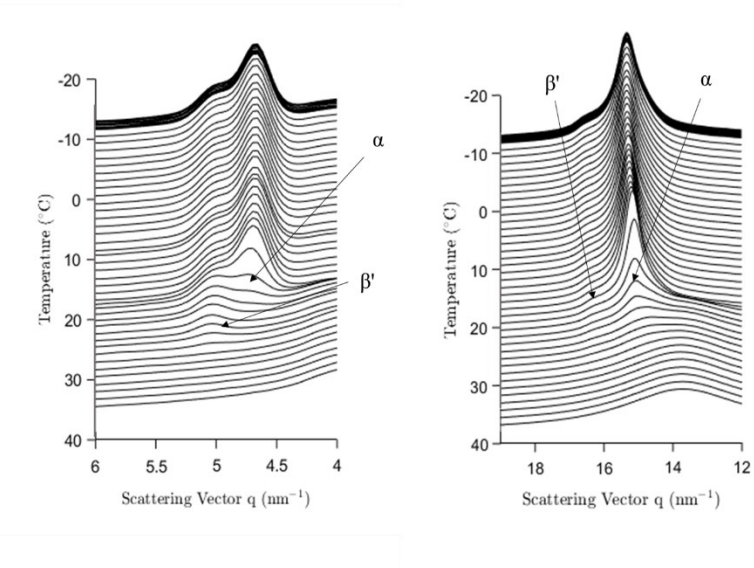

Figure 5-7 X-ray diffraction intensity as a function of scattering vector at different temperatures for MMM during cooling at 10 C° /min from the melt at 70 °C down to -10°C. The left panel shows the SAXD from the (003) plane of the long spacing. The WAXD from the short spacings is shown on the right. The β' polymorph appears before the α polymorph.

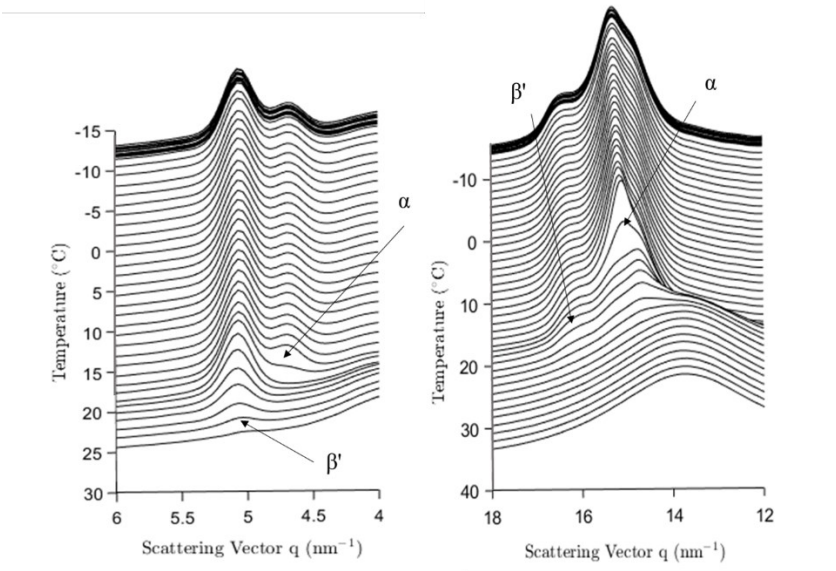

Figure 5-8 X-ray diffraction intensity as a function of scattering vector at different temperatures for MMM during cooling at 7.5 C°/min from the melt at 70 °C down to -10°C. The left panel shows the SAXD from the (003) plane of the long spacing. The

WAXD from the short spacings is shown on the right. The β' polymorph appears before the α polymorph.

At fast cooling rates (ranging from 20C°/min to 5C°/min) in Figures 5-9 and 5-10 for both LLL and MMM, the α and β' polymorphs were present at the end of the cooling process. According to Table 5-2, the peak position is determined by fitting in Igor. The average value of the first peak and second peak position in the (003) reflection, under all cooling rates, was found to be 3.49 ± 0.026 and 3.25 ± 0.007, respectively. The average value of the first peak and second peak position in the (004) reflection, under all cooling rates, was found to be 3.54 ± 0.008 and 3.25 ± 0.005, respectively. By combining the literature values of the lamella distance of α and β' in LLL in Table 5-1 (Takeuchi et al, 2003), it can be confirmed that the first peak belongs to α and the second peak belongs to β'.

A similar result was observed in MMM, where the α polymorph was found at higher cooling rates (20 C°/min and 15 C°/min), and both the α and β' polymorphs were detected at intermediate rates (between 10 C°/min and 2.5 C°/min). The percentage of generated β' polymorph in MMM exhibits a decreasing trend with an increasing cooling rate. This also supports the results from the DSC thermograms.

In general, when a substance is rapidly cooled, a metastable polymorph tends to form first, which can be either the α or β' polymorph. This metastable polymorph can then transition to a more stable one. This happens even though the difference in Gibbs energy between the crystal and the liquid, which is ultimately the driving force, is smaller for a metastable polymorph than for the stable polymorph. The reason is that the resistance for formation, i.e. the activation energy barrier, is much lower for the metastable polymorph. In this study, however, the behavior of LLL was found to

deviate from this expected sequence of polymorphic transition. According to energy considerations, the α polymorph, with its lower surface energy and enthalpy of crystallization, should crystallize first.

While cooling, β' crystals are nucleated and grown by liquid molecules, and the rate of this process is dependent on the temperature of the cooling rate. As the temperature decreases, the liquid will reach the melting point of α, whether or not it contains crystals. In the remaining liquid, there is a competitive process between the nucleation of β' and α. Despite the fact that β' can act as a nucleation template, it eventually becomes more favorable for α to form from the remaining liquid.

This phenomenon has been observed in several studies. For instance, Takeguchi et al. (2020) examined the crystallization of saturated monoacid TAGs and found that they initially formed unstable polymorphs, specifically the α or β' forms, which then transformed into the more stable β form through solid-solid transformations. Additionally, Sato (2018) noted that when the cooling rate applied to neat liquid samples decreased, the competitive polymorphic crystallization favored the formation of more stable forms with higher melting temperatures. Conversely, higher cooling rates resulted in the occurrence of less stable polymorphic forms with lower melting temperatures.

Table 5-2 d-spacings in (nm) obtained from the peak position fitting by Igor under different cooling rate of LLL of (003) and (004) reflection

CR	20.0	15.0	10.0	7.5	5.0	2.5
α (003)	3.522	3.513	3.492	3.489	3.455	3.437
β' (003)	3.265	3.262	3.251	3.252	3.250	3.248
α (004)	3.528	3.528	3.542	3.541	3.544	3.547
β' (004)	3.259	3.250	3.247	3.248	3.246	3.243

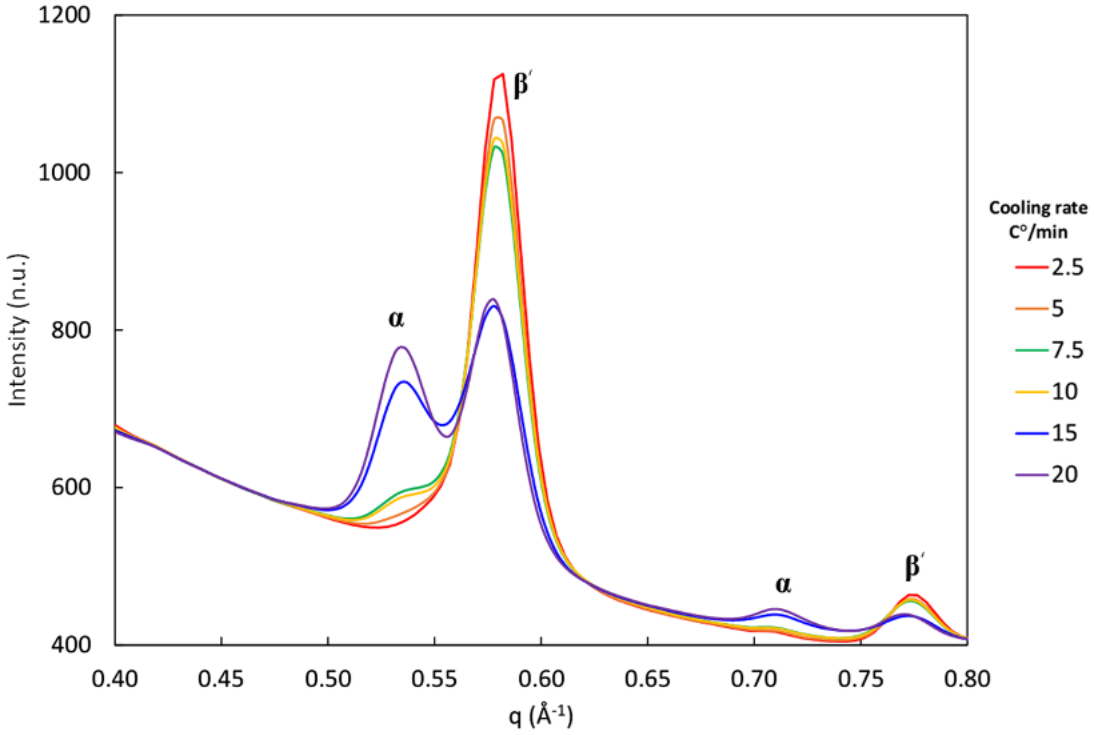

Figure 5-9 X-ray diffraction intensity for the (003) and (004) reflections, as a function of scattering vector q ($Å^{-1}$), of LLL at the end of cooling (-10 °C). LLL was crystallized in a capillary from the melt using different cooling rates.

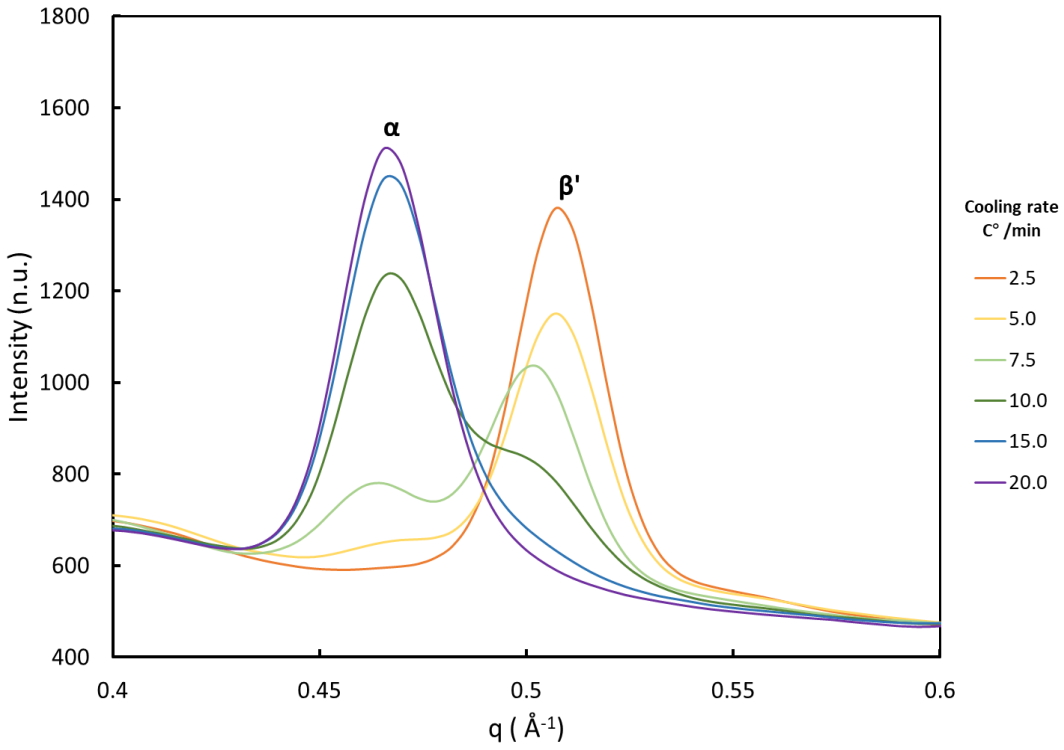

Figure 5-10 X-ray diffraction intensity for the (003) reflections, as a function of scattering vector q ($Å^{-1}$), from MMM at the end of cooling (-10 °C). MMM was crystallized in a capillary from the melt using different cooling rates.

CHAPTER 6 RESULTS AND DISCUSSION– III MATHEMATICAL METHOD TO LOCATE THE SECOND ONSET IN A COEXISTING CRYSTALLIZATION EVENT

6.1 Area fraction

This study identified the phases present by analyzing the d-spacings obtained from X-ray data during the isothermal hold at -10 °C. Only α and β' forms were detected at the end of crystallization. It was assumed that the sample was completely crystalline, and no polymorphic transitions were observed during the holding time at -10 °C.

In a crystal lattice, atoms are arranged in a repeating pattern that creates a series of parallel planes known as lattice planes. The (001), (002), (003), and (004) planes are a group of parallel planes within a crystal lattice that differ only in their interplanar distances. The (001) planes are perpendicular to the crystal surface that has the end of the alkyl chains, i.e. the methyl ($-CH_3$) groups. The length of the TAG molecules and their tilt with respect to that plane determine the interplanar distance between repeating atoms. The (002), (003), and (004) planes are parallel to (001). The interplanar distance is characteristic for each type of plane and depends on composition and polymorphism. As expressed in Bragg's law, the distance between the (002) and (003) planes, however, is always 1/2 and 1/3 of the distance between the (001) plane, respectively. The distance between (004) planes 1/4 of the distance between the (001) planes. This analysis focused on data from the (003) and (004) reflections as the (003) plane is typically well-resolved in X-ray diffraction patterns of TAGs and can provide a strong and distinct diffraction peak, which makes it easy to identify and measure. Additionally, using (004) planes can help confirm the

interplanar distance. Therefore, the X-ray (003) reflection and (004) reflection peaks corresponding to the α and β' polymorphs of LLL were explored at all cooling rates. As an illustration, Figure 6-1 (A) and (B) shows the (003) and (004) reflections for LLL cooled at rates of 20 C°/min and 2.5 C°/min, respectively. The peak positions and peak areas were obtained by manually fitting the data using the Voigt distribution with IgorPro9 software. The peak positions were constrained to have the ratio of scattering vector 1/3:1/4.

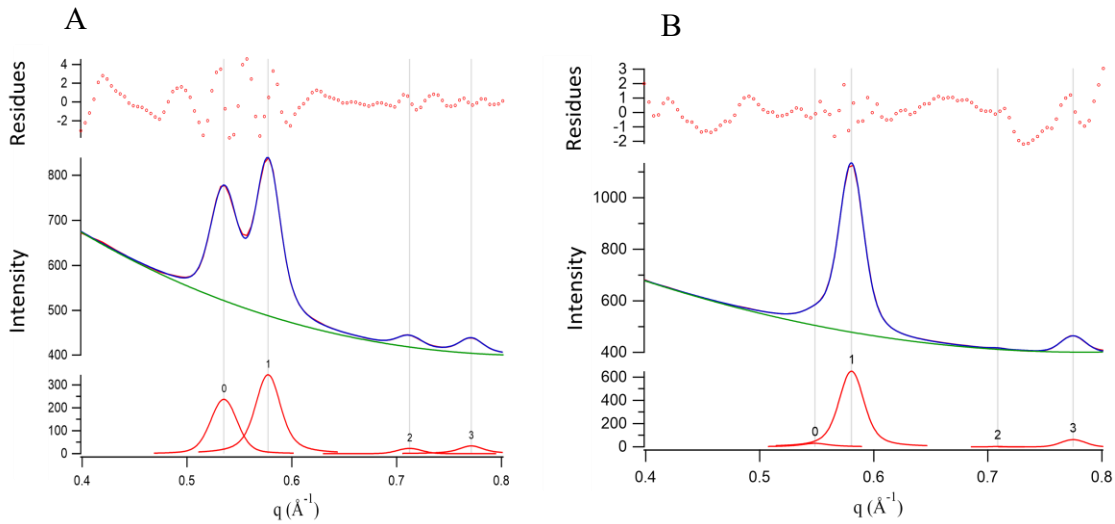

Figure 6-1 Intensity of XRD as a function of scattering vector q, displaying the functions fitted to peaks (003) (peaks # 0 and 1) and (004) (peaks # 2 and 3). (A) Cooling rate of 20 C°/min, (B) cooling rate of 2.5 C°/min (from Igor) Voigt distribution.

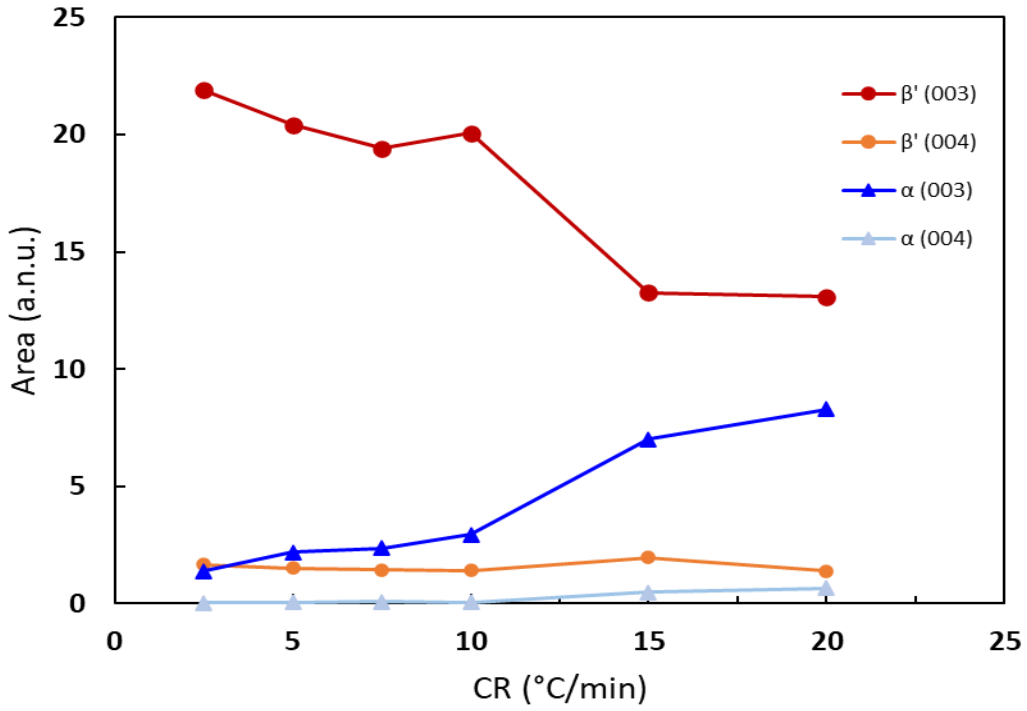

Figure 6-2 XRD areas of the peaks (003) and (004) from LLL for α and β' phases as a function of cooling rates. These are the areas at the endo of crystallization, each one obtained from averaging the measured areas of at least 10 diffraction patterns.

Table 6-1 Average of the areas integrated using Igor Pro9 from the peaks from the X-ray diffraction patterns of the (003) and (004) planes of LLL. The area ratios are the two last lines.

CR	20.0	15.0	10.0	7.5	5.0	2.5
β' (003)	13.08	13.26	20.05	19.42	20.42	21.90
β' (004)	1.37	1.95	1.40	1.43	1.51	1.66
α (003)	8.28	7.00	2.93	2.36	2.19	1.38
α (004)	0.67	0.48	0.06	0.08	0.04	0.04
α/β'(003)	0.63	0.53	0.15	0.12	0.11	0.06
α/β'(004)	0.49	0.25	0.05	0.05	0.03	0.02

6.2 The Proportionality Factor and mass fraction

Quantification of the different polymorphic phases present in crystalline triacylglycerols is crucial for understanding their structure-property relationships and controlling their functional properties in various applications. To achieve accurate quantification, a proportionality factor is required to establish the relationship between the areas of X-ray diffraction (XRD) peaks and the mass fraction of each polymorphic phase.

In X-ray diffraction, it is ideal to have a linear relationship between the crystalline mass and the peak area for a specific polymorph. This relationship holds true when the experimental conditions, such as sample thickness and beam intensity, are normalized with respect to the measured crystalline mass. It is important to note that the proportionality factor is assumed to remain constant regardless of the temperature and the experimental cooling rate. However, deviations from linearity can occur, especially at high cooling rates, due to the non-equilibrium nature of the crystallization process. These deviations may affect the accuracy of quantification and should be taken into account.

The following equation relates the mass value M, and XRD peak area value A_x, of two components of a mixture of polymorphs to their respective proportionality factors P:

$$M_{\alpha} = A_{x\alpha} \cdot P_{\alpha}; M_{\beta'} = A_{x\beta'} \cdot P_{\beta'} \tag{6-1}$$

While the two phases crystallize simultaneously during cooling the mass fraction is:

$$w_{\beta'} = \frac{M_{\beta'}}{M_{\alpha} + M_{\beta'}} \tag{6-2}$$

Therefore, the proportionality factor can be expressed in terms of mass fraction:

$$w_{\beta'} = \frac{A_{x\beta'} \cdot P_{\beta'}}{A_{\mathrm{x}\alpha} \cdot P_{\alpha} + A_{x\beta'} \cdot P_{\beta'}} \tag{6-3}$$

Reorganized as

$$w_{\beta'} = \frac{1}{\left(1 + \frac{A_{\mathrm{x}\alpha} \cdot P_{\alpha}}{A_{\beta x'} \cdot P_{\beta'}}\right)} \tag{6-4}$$

The ratio of P_{α} to $P_{\beta'}$ factors $w_{\beta'}$ was determined to be 1.322 ± 0.004 for the X-ray diffraction areas. A linear regression was performed using the calculated mass fractions, and the estimated areas for a mass fraction of 1 are shown in Figure 6-3. The areas for all material in the β' phase was 23.3 ± 0.26, while for the α phase they were 17.7 ± 0.25. The regression produced estimates of areas of ± 0.49 for β' and ± 0.16 for α, with corresponding fraction estimates of ± 0.02 and ± 0.01, respectively. The uncertainty in the fitted peak areas was less than 2% for β' and between 2% and 9% for the α form. The uncertainty in the mass fraction estimate increased as the area decreased. Taking all of these effects into account, the uncertainty in the mass fraction estimates of β' is less than 1.5%.

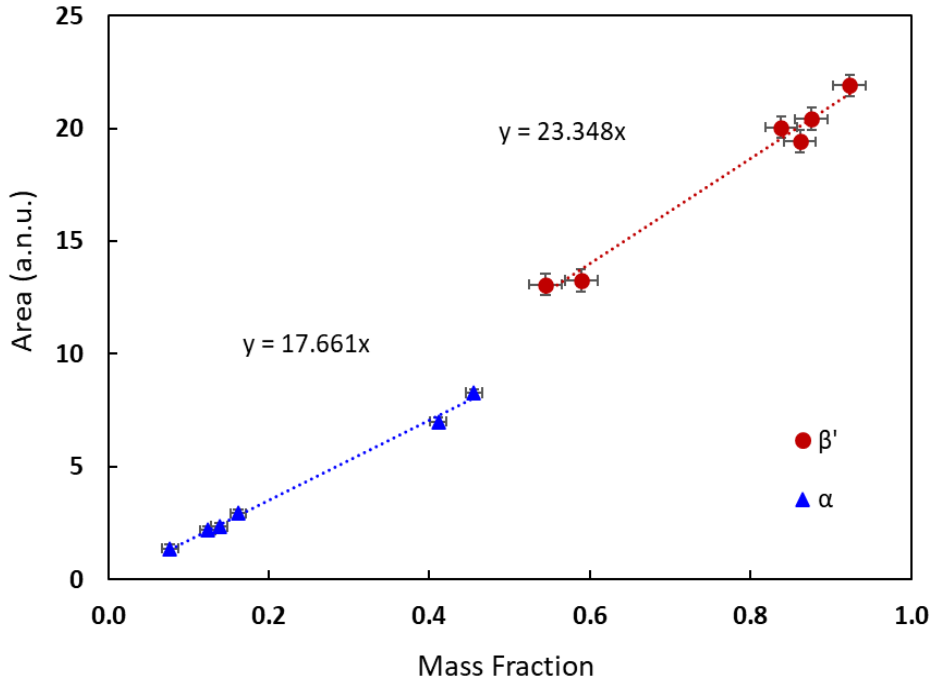

Figure 6-3 XRD areas of the (003) and (004) peaks as a function of mass fraction of α and β'.

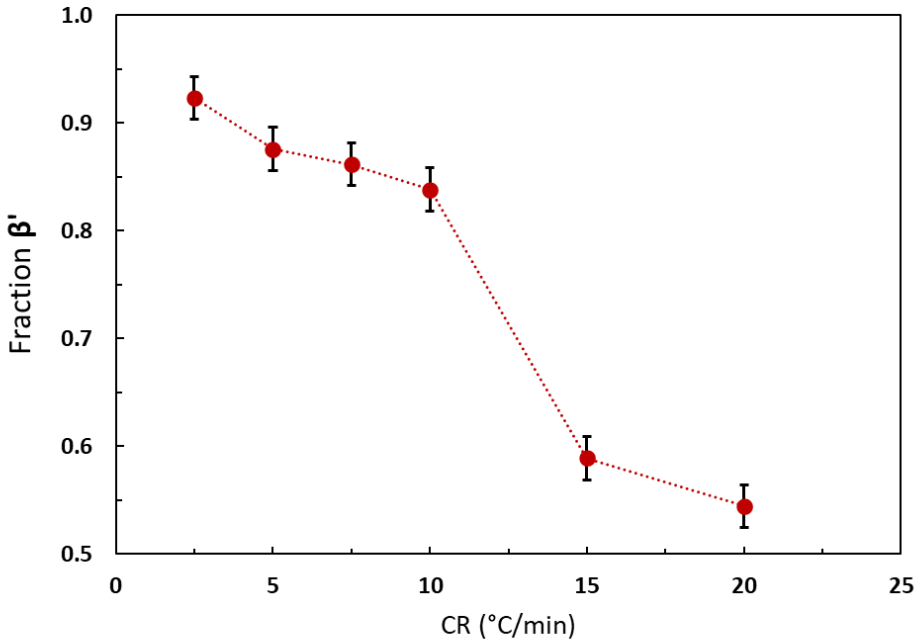

Figure 6-4 Mass fraction of β' at the end of crystallization as a function of cooling rate (CR) in C°/min

6.3 Fitting DSC Thermograms

The method to fitting thermogram data developed for this research starts by estimating the areas of α and β' polymorph in thermogram. To do this, an initial estimate of the total area, A_T, is computed as a numerical integral of the thermogram heat flow, after removal of a coarse estimate of the baseline, as explained in the next section.

$$A_T = A_{\beta'} + A_{\alpha} \tag{6-5}$$

Using this initial estimate of A_T, the area of the beta prime region, $A_{\beta'}$, can be calculated from the mass fraction using the enthalpies as proportionality factors, in equation:

$$A_{\beta'} = \frac{A_T}{1 + \frac{1 - w_{\beta'}}{w_{\beta'}} \cdot \frac{\Delta H_{\beta'}}{\Delta H_a}} \tag{6-6}$$

The variable to fit is $0 < w_{\beta'} < 1$. The XRD experiments were done in capillaries in a thermal holder that is different from the DSC. Although the general trends are the same between instruments, details of the behaviour of the same material can be somewhat different between the two setups. The onset temperature, the rate of nucleation and growth of each polymorph, and the final mass fraction of each one is different, as discussed in section 4.3.

The area of the α region in the thermogram (not under an X-ray peak), Aα, can be then estimated using the equation

$$A_\alpha = \frac{A_T}{1 + \frac{w_{\beta'}}{1 - w_{\beta'}} \frac{\Delta H_a}{\Delta H_{\beta'}}} \tag{6-7}$$

It can be expressed as well as

$$A_\alpha = \left(\frac{1 - w_{\beta'}}{w_{\beta'}} \cdot \frac{\Delta H_{\beta'}}{\Delta H_a} \right) \cdot A_{\beta'} \tag{6-8}$$

6.3 Estimated baseline generation with iterative linear fitting

The baseline is the portion of the DSC signal where the signal comes only from the change of temperature of the material, not from phase transitions. From observation of many thermograms it was assumed to be a reasonably linear function of temperature above and below the crystallization event. This baseline is subtracted from the original data, and the integral function in MATLAB is used to find an initial value of A_T between onset temperature β' polymorph of and the start point of the area selected to calculate the slope of the solid. The amount of heat needed to raise the temperature of a material is directly

proportional to its heat capacity. Using this relationship, we can simulate the two components that contribute to the solid phase of our system in proportion to their respective heat capacities.

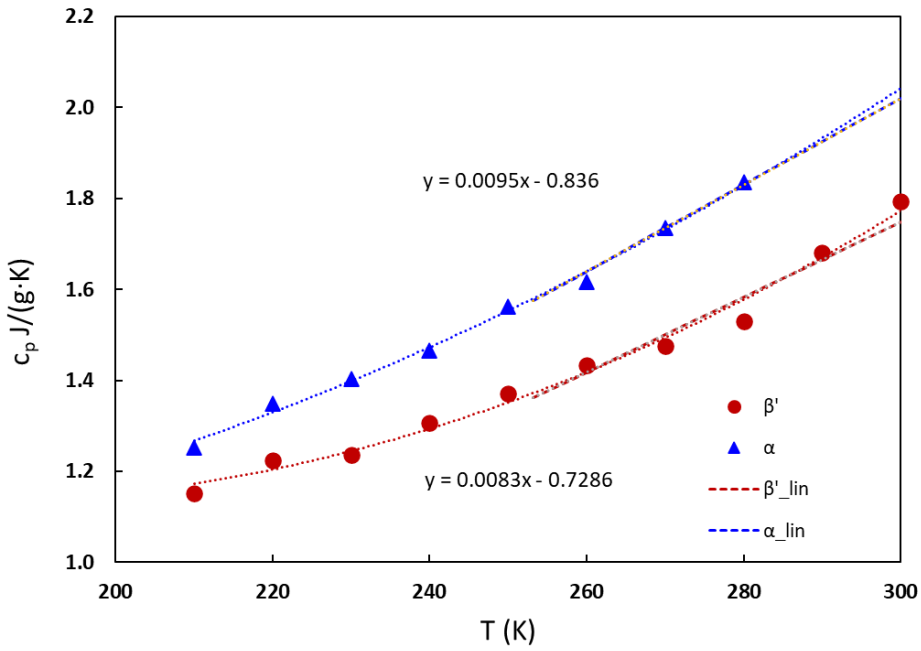

Figure 1-5 Specific heat in J/(g·K) for LLL α and β' polymorphs, as a function of absolute temperature. (Adapted from Hampson, J.W., Rothbart, H.L. (1983))

We performed a linear regression analysis on the data in the -20 °C to 20 °C range (253.15 K - 293.15 K), based on the experimental specific heat capacity of Hampson's data. Based on this analysis, we calculated the values of r_0 and r_1, which represent the ratios of the specific heat capacities of two different polymorphs or components, denoted by α and β', respectively.

$$cp_{\alpha} = cp_0^{\alpha} + cp_1^{\alpha} \cdot T; \quad cp_{\beta'} = cp_0^{\beta'} + cp_1^{\beta'} \cdot T \tag{6-9}$$

$$r_0 = \frac{cp_0^{\alpha}}{cp_0^{\beta'}}\ ; \qquad r_1 = \frac{cp_1^{\alpha}}{cp_1^{\beta'}} \tag{6-10}$$

The parameters bs_1 and bs_2, which define the heat capacity value, were obtained by independently fitting the end of the DSC heat flow thermogram, i.e. below the end of crystallization.

$$cp_s = bs_1 + bs_2 \cdot T \tag{6-11}$$

The coefficient of regression at the end of the curve can be expressed using the fitting parameters bs_1 and bs_2, as well as the mass fraction β'.

$$cp_0^{\beta'} = \frac{bs_1}{w_{\beta'} - w_{\beta'} \cdot r_0 + r_0} \tag{6-12}$$

$$cp_1^{\beta'} = \frac{bs_2}{w_{\beta'} - w_{\beta'} \cdot r_1 + r_1} \tag{6-13}$$

$$cp_0^{\alpha} = r_0 \cdot cp_0^{\beta'} \tag{6-14}$$

$$cp_1^{\alpha} = r_1 \cdot cp_1^{\beta'} \tag{6-15}$$

The baseline can be easily defined by the following equation:

$$BS = \left((bs_1 + bs_2 \cdot T) \cdot \Delta T_s \cdot w_s + (bl_1 + bl_2 \cdot T) \cdot \Delta T_l \cdot (1 - w_s)\right) \cdot C_R \tag{6-16}$$

Where ΔT_s is the temperature interval between the end of fitting and peak maximum temperature, ΔT_l is the temperature interval between onset temperature and peak maximum temperature. CR represents the cooling rate. The total fraction of solids (material crystallized) is w_s. For the initial guess of the baseline, we assumed that the transition from liquid to solid happens at the temperature T_{int}, at the intersection between the two lines.

$$(bs_1 + bs_2 \cdot T_{int}) = (bl_1 + bl_2 \cdot T_{int}) \tag{6-17}$$

The further two iterations compute w_s at each point using the peaks fitted to the crystallization data.

6.4 Peak signal identification

We propose a modified Avrami function to identify peak signals and detect second onsets, which has the same expression as the probability density function of the Weibull distribution. The Avrami function, presented earlier in Equation 2-27, is a mathematical equation commonly used to describe the kinetics of phase transformations. As the Weibull distribution, it is able to model a broad range of distribution shapes, surpassing the Normal (Gaussian) distribution in this regard, and its capable to handle skewed data. Specifically, we employed the scale factor of the Weibull distribution to control the shapes of the peaks and used a threshold parameter to establish the lower limit, allowing us to identify the onset time. We modify the Avrami (Weibull) function for non-isothermal conditions:

$$y_c = 1 - exp\left[-\left(\frac{\Delta T}{b}\right)^a\right] \; with \; \Delta T = T_o - T \tag{6-18}$$

$$y_D = \frac{a}{b}\left(\frac{\Delta T}{b}\right)^{a-1} \cdot exp\left[-\left(\frac{\Delta T}{b}\right)^a\right] \tag{6-19}$$

We introduce a variable characteristic rate constant, in lieu of "b", which becomes b - $c \cdot \Delta$T. To ensure that the cumulative function remains between zero and one, a scaling factor y_o is introduced. The y_o term is in all our cases was very close to 1.

$$y_c = \left(1 - exp\left[-\left(\frac{\Delta T}{b - c \cdot \Delta T}\right)^a\right]\right) \cdot y_o \; with \; \Delta T = T_o - T \tag{6-20}$$

In the limit when ΔT is very large, the scaling factor is very close to unity

$$y_o \rightarrow \left(\frac{exp((-c)^{-a})}{exp((-c)^{-a}) - 1}\right) \approx 1 \tag{6-21}$$

Thus, it is possible to simplify the equation as

$$y_c = 1 - exp[-(r_T{}^a)] \; with \; \Delta T = T_o - T \; and \; r_T = \frac{\Delta T}{b - c \cdot \Delta T} \tag{6-22}$$

The derivative of this function with respect to ΔT then becomes:

$$y_D = \frac{a}{b - c \cdot \Delta T}(r_T{}^{a-1})(1 + c \cdot r_T) \cdot exp[-(r_T{}^a)] \tag{6-23}$$

To keep r_T positive, the fit parameter used was "c_m" with the constraint,

$$c = \frac{c_m - 1}{c_m \cdot \Delta T_{max}} \; with \; 1 \le c_m \le c_{m_{max}} \tag{6-24}$$

The fitting functions can be used to find the parameters that best fit the functions to the data plotted versus time. To use it as a function of time, we replace the experimental ΔT with the linear relationship provided by the cooling rate, C_R.

$$\Delta t = t - t_o \; and \; \Delta T = T_o - T \; with \; \Delta T = C_R \cdot \Delta t \tag{6-25}$$

Similarly, we introduce a time variable, b then becomes b - $c \cdot \Delta t$. The cumulative function is still between zero and one, with a scaling factor y_{ot}. The scaling factor is as well very close to one in the limit when ΔT is very large.

$$y_c = \left(1 - exp\left[-\left(\frac{C_R \cdot \Delta t}{b - c \cdot C_R \cdot \Delta t}\right)^a\right]\right) \cdot y_{ot} \; with \; \Delta t = t - t_o \tag{6-26}$$

$$y_{ot} \rightarrow \left(\frac{exp((-C_R \cdot c)^{-a})}{exp((-C_R \cdot c)^{-a}) - 1}\right) \approx 1 \tag{6-27}$$

$$y_c = 1 - exp[-(r_t{}^a)] \; with \; \Delta t = t - t_o \; and \; r_t = \frac{C_R \cdot \Delta t}{b - c \cdot C_R \cdot \Delta t} \tag{6-28}$$

The derivative function with respect to **Δ**t is then

$$y_D = \frac{a}{b - c \cdot C_R \cdot \Delta t}(r_t{}^{a-1})(1 + c \cdot r_t) \cdot exp[-(r_t{}^a)] \tag{6-29}$$

There are six shape fitting parameters, $a_{\beta'}$, $b_{\beta'}$, $c_{m\beta'}$ for β' and a_α, b_α, $c_{m\alpha}$ for α. There are also two more parameters, which are the onset time and temperature T_o, for the α polymorph;

and the mass fraction of the β' at the end of the crystallization, $w_{\beta'}$.To prevent negative values, the fit parameter for c is "c_m" with the constraint,

$$c = \frac{c_m - 1}{c_m \cdot \Delta T_{max}} \; with \; 1 \leq c_m \leq c_{m_{max}} \tag{6-30}$$

Reformulating the derivative function

$$r_t = \frac{C_R \cdot \Delta t}{b - \frac{c_m - 1}{c_m \cdot \Delta T_{max}} \cdot C_R \cdot \Delta t} \tag{6-31}$$

$$y_D = \frac{a}{b - c_m \cdot C_R \cdot \Delta t} ({r_t}^{a-1}) \left(1 + \frac{c_m - 1}{c_m \cdot \Delta T_{max}} \cdot \; r_t\right) \cdot exp[-({r_t}^{a})] \tag{6-32}$$

The procedure to fit the function to the data and find the values of the eight parameters was programmed in MATLAB. The search for the minimum of the sum of squared errors was done using the 'fmincon' function. The 'fmincon' function is a widely used tool in MATLAB for solving constrained nonlinear optimization problems. It is designed to find the minimum value of a multivariable objective function subject to a set of constraints.

The function uses various numerical methods and optimization algorithms, such as interior-point and active-set methods, to efficiently search for the optimal solution. The search process involves iteratively adjusting the values of the input variables until the minimum value of the objective function is found while satisfying the constraints. The numerical techniques used by the function, such as gradient and Hessian calculations, improve the accuracy and efficiency of the optimization process.

To use the 'fmincon' function, several inputs are required, including the objective function, initial guess, linear and nonlinear constraints, and options. The objective function is the

function to be minimized, usually the sum of squared errors between the calculated function and the data. The initial guess is the starting point for the search algorithm for a given data set. The initial guess can be obtained from the result of the previous fitting. The constraints are the conditions that the solution must satisfy. In our case, derivatives and critical points were used to constrain the fitting.

The first derivate and second derivate are expressed as follows:

$$y'_D = \frac{\partial}{\partial \Delta t} \frac{a}{b - c_m \cdot C_R \cdot \Delta t} (r_t{}^{a-1})(1 + c_m \cdot r_t) \cdot exp[-(r_t{}^a)] \tag{6-33}$$

$$y''_D = \frac{\partial^2}{\partial \Delta t^2} \frac{a}{b - c_m \cdot C_R \cdot \Delta t} (r_t{}^{a-1})(1 + c_m \cdot r_t) \cdot exp[-(r_t{}^a)] \tag{6-34}$$

These derivatives were obtained as analytical functions in Maple and pasted into MATLAB nested functions. They are rather cumbersome expressions (See appendix).

The output of the function includes a structure with calculated heat flow, residuals, and calculated baseline values for each data point, as well as other coefficients and results related to the fitting process.

The 'Esthf' structure contains nptsx6 cells, with each cell representing one data point in the run. The columns in each cell represent the culled data times, culled data temperatures, culled data heat flow, calculated heat flow, residuals, and calculated baseline, respectively. The 'ftcpl' and 'ftcps' output parameters are the heat capacity coefficients for the liquid and solid phases, respectively, for each run.

The 'ftcoeff' structure contains coefficients and other results related to the fitting process for each run. The rows in the structure correspond to each of the 54 runs in the DSC set

being analyzed. The columns in each cell include the coefficients fitted for the run, the minimized value of the objective function, a flag indicating the type of exit from the optimization algorithm used, a message from the optimization algorithm, the linear and nonlinear constraints values, the gradient of the minimized function with respect to the parameters, and the real part of the Hessian matrix. There are also some additional columns with information related to the cooling rate, onset temperature, and β' mass fraction.

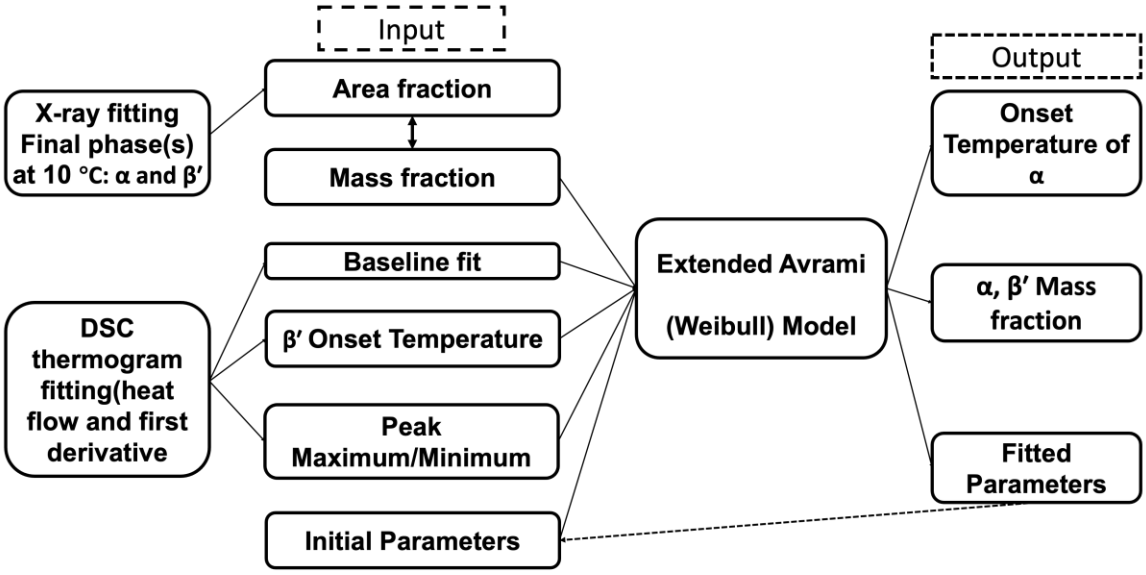

Figure 6-6 The schematic diagram of MATLAB fitting program for detect second onset in DSC thermograms.

6.5 Results from the fitting procedures

Figures 6-7, 6-8, and 6-9 show the fitting result of the MATLAB code for data from LLL pan 1 under 2.5 C°/min, 10 C°/min, and 20 C°/min cooling rates. Including the heat flow, fitting, rate (Derivative) functions for α and β', as well as a fitted baseline against undercooled time. Several DSC thermograms under slow cooling rates often show two distinct peaks. When fitted, the onset temperatures appeared to be too high to correspond to the α polymorph. Perhaps at such cooling rates the second polymorph is not α, or the literature value for the real melting point of α has been severely underestimated. The longer cooling time allows for the formation of more nuclei of the β' polymorph, resulting in a reduced amount of crystallizable liquid available for the α polymorph. On the other hand, at faster cooling rates, most DSC thermograms exhibit one late “irregular” peak. This third peak appears after the onset of β' and after the onset of α. It is likely that the in the competing

crystallization process below the α melting point, as the alpha is formed, some of it may start transitioning to β'.

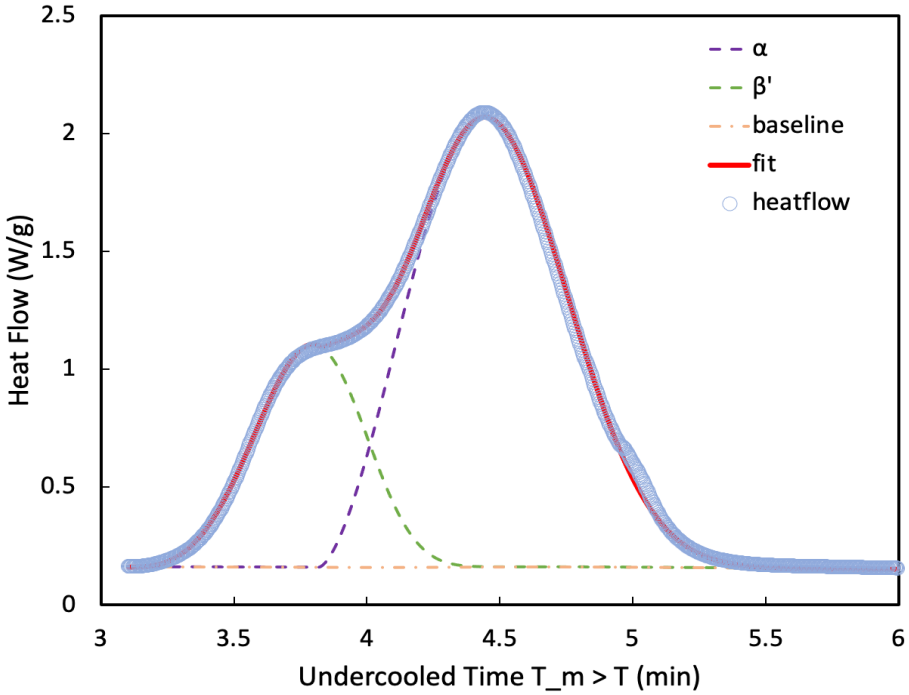

Figure 6-7 Heat flow of LLL1 as a function of undercooled time, under a cooling rate of 2.5 C°/min, including heat flow, total function fitted (red), α rate function, β' rate function, and fitted baseline.

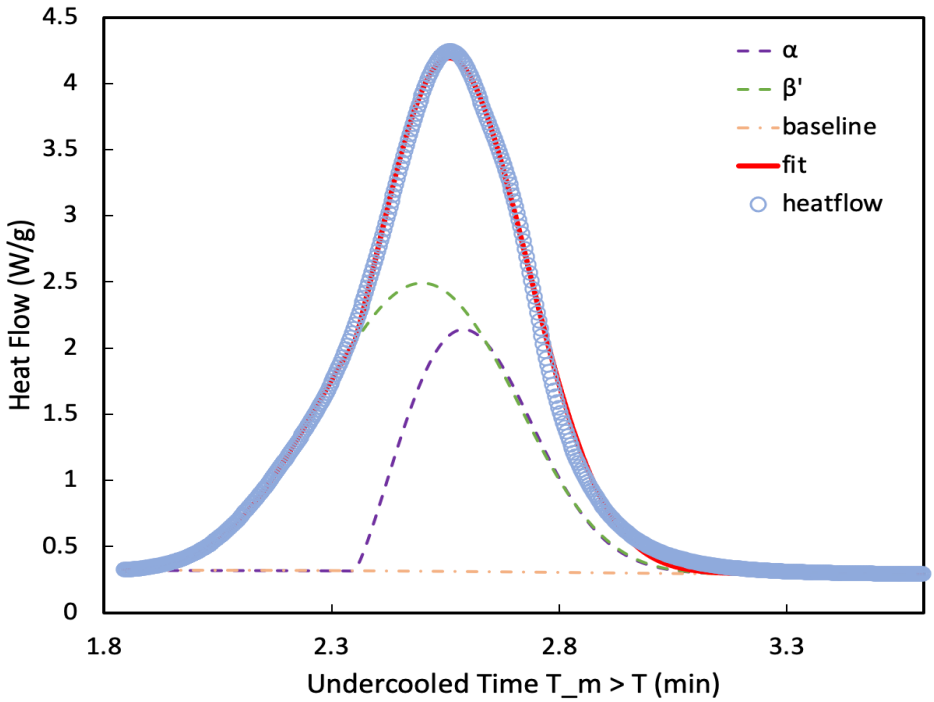

Figure 6-8 Heat flow from LLL1 as a function of undercooled time, under a cooling rate of 10 C°/min, including heat flow, total function fitted (red), α rate function, β' rate function, and fitted baseline.

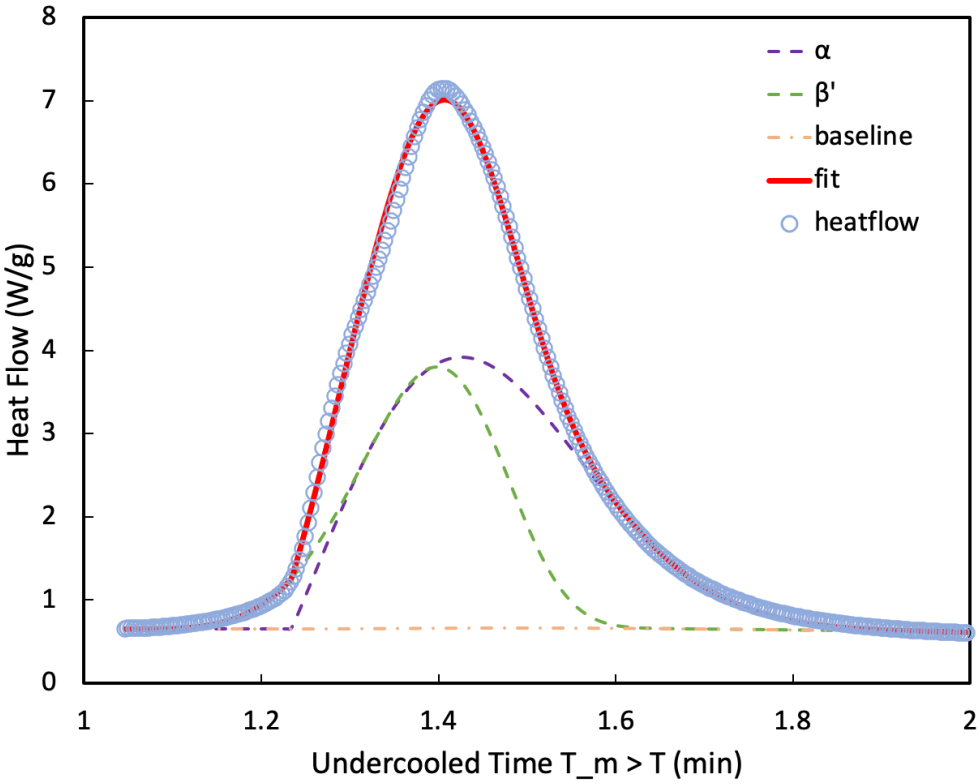

Figure 6-9 Heat flow from LLL1 as a function of undercooled time, under a cooling rate of 20 C°/min, including heat flow, total function fitted (red), α rate function, β' rate function, and fitted baseline.

The fitting of the extended Avrami function to the data sets was an arduous work, made especially difficult by the deviation of the temperatures from the linear ramp.

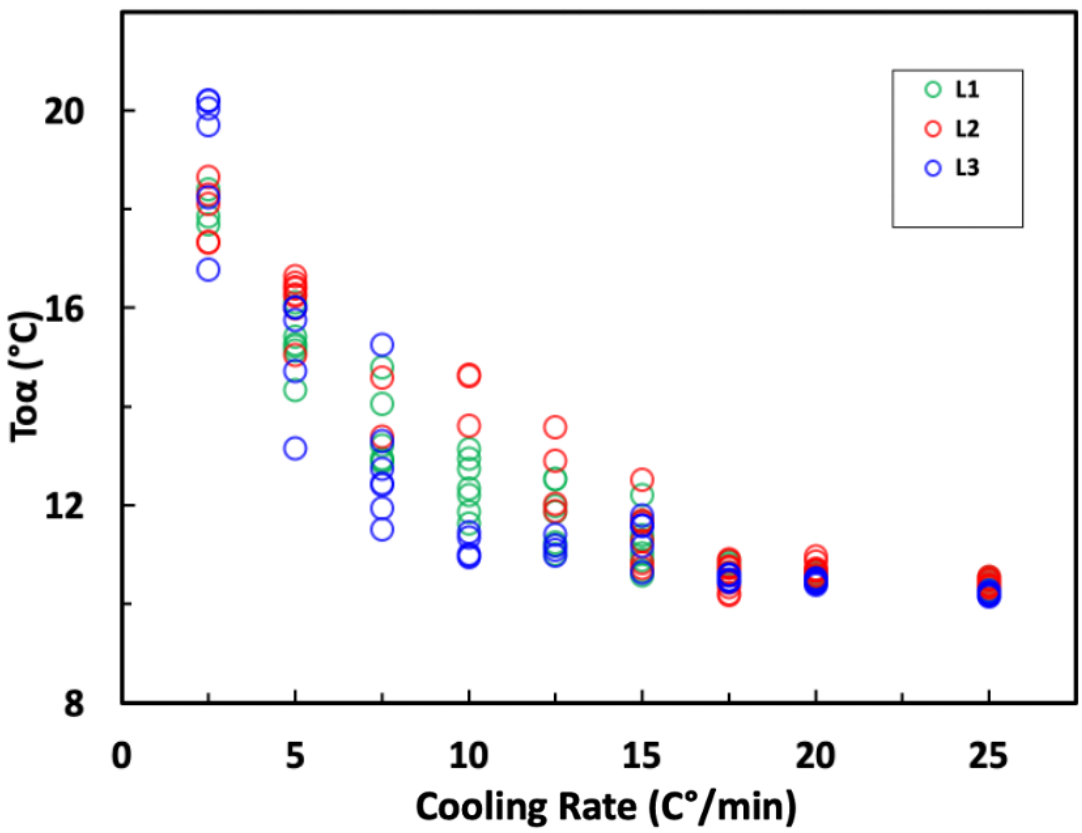

Figure 6-10 Onset temperature of the α polymorph as a function of the cooling rate for LLL1, LLL2, and LLL3, which were computed by the MATLAB program using the DSC thermograms obtained with the DSC Q100.

The onset temperatures of α and β' for LLL1, LLL2, and LLL3, are plotted against the cooling rate in Figures 6-10 and 6-11. Two different MATLAB programs were developed to compute these values from the DSC thermograms obtained with the DSC Q100 and premium aluminum hermetic pans. Figure 6-11 also includes the average values and 95% confidence intervals. There are a couple of methodological factors that contribute strongly to the uncertainty of the data. Firstly, the fitting process has eight variables, and the overlapping peaks are not sharp. Therefore, similar looking peaks can be fitted to somewhat different sets of values of the parameters.

Secondly, there may be some differences in heat transfer due to pan positioning that can also contribute to uncertainty. However, it is worth noting that the effect of these differences seems to be relatively small for the cooling rate of 17.5 C°/min, 20 C°/min, and 25 C°/min. Seems that this effect may be amplified if the cooling rate is reduced. One of the reasons is that when a higher cooling rate is applied with a DSC instrument, it is too fast for the DSC to detect any small variations. The higher the cooling rate is, the less data points are collected, because the instrument reads a maximum of 5 points per second. It may also be that at faster cooling rates a large undercooling is reached much faster and there is less time for events to go astray.

Beyond these two factors, it is likely that the behaviour of these molecules during liquid cooling and crystallization is very variable in the mid range of cooling rates. In the liquid two processes of pre-nucleation of α polymorph and crystallization of β' polymorph take place simultaneously. Therefore, there exists a competing process between the crystallization of two polymorphs, which has already begun and is ongoing. Depending on the cooling rate, these processes compete at different rates and in different manners. The greater the number of potential interactions in the system, the higher the probability of encountering some degree of variability in the outcome. Even tiny variations in the effective cooling rate, and the compensating actions of the DSC, introduce a different path for this competition.

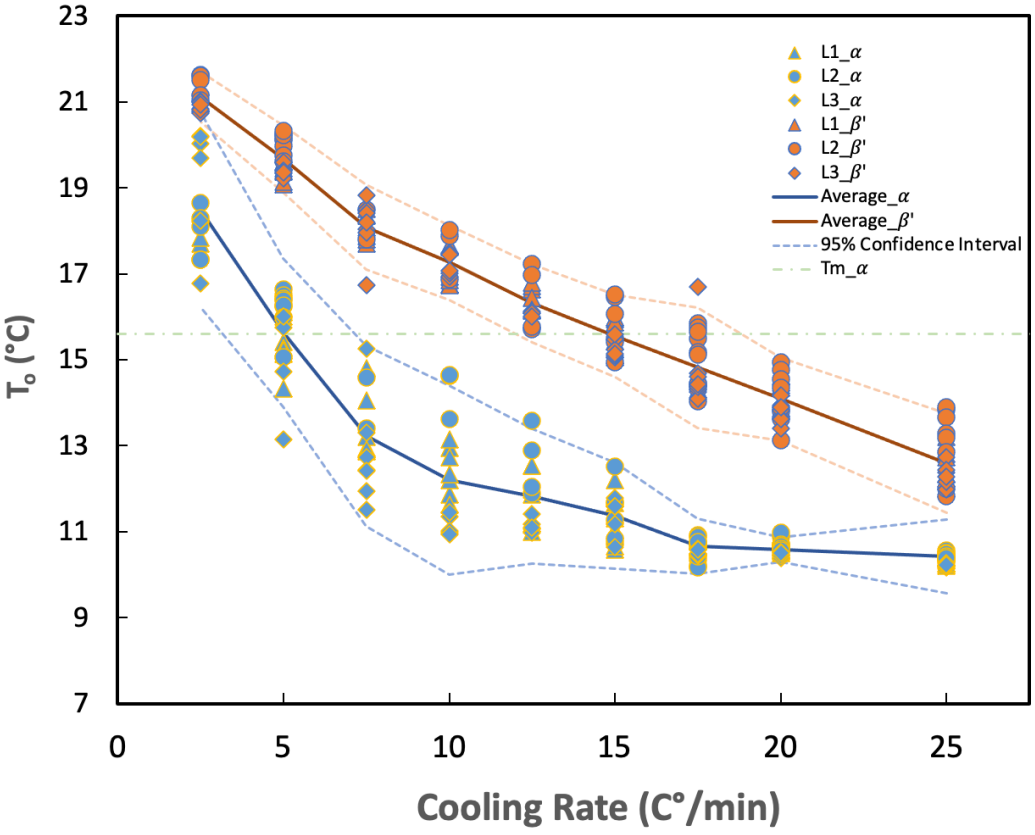

Figure 6-11 Onset temperature for α and β' polymorphs for LLL1, LLL2, and LLL3 as a function of nominal cooling rate. The average values and 95% confidence intervals are plotted as well. These values were computed by the MATLAB programs using the DSC thermograms obtained with the DSC Q100 and premium aluminum hermetic pans.

Figure 6-12 and Figure 6-13 shows the fitting result of parameters 'a' and 'b' for the crystallization of α and β'. Parameter 'a' is the dimensionless exponent representing the nature of the geometry of the system, as discussed in chapter 2, Equation 2-27. The 'a' parameter shows a gradual increase up to 15 C°/min, followed by a clear change in behavior. Parameter 'b' is the inverse of the rate of transformation. The 'b' parameter also has a break in its trend around 15 C°/min. The values of the 'c' parameter are plotted in Figure 6-14. The 'c' parameter was introduced by the author as part of the characteristic

rate constant, in Equation 6-20. The ‘c’ parameter did not show a clear trend and had a huge uncertainty: the error bars would be far out of the chart. To keep it from making the denominator zero or negative, we used large values of ΔT_{max} in equation 6-30, 56 K for β' and 36 K for α. Thus, even large variations in the c_m fitting parameter had a small impact on the fit. For future developments, it would be better to scale the ‘c’ parameter differently.

The values of the parameter $w_{\beta'}$, the mass fraction of β' at the end of crystallization, are plotted in Figure 6-15 as a function of cooling rate. The Avrami parameters To, ‘a’, ‘b’, and ‘c’ correspond to either the β' or the α polymorph crystallization kinetics. The mass fraction is the parameter that ‘connects’ those two crystallization events to make them add up to the total thermogram peak. This is described by Equation 6-8. As happens with the ‘c’ parameter, the ratio $(1- w_{\beta'})/w_{\beta'}$ can take a range of values that produce almost the same good fit.

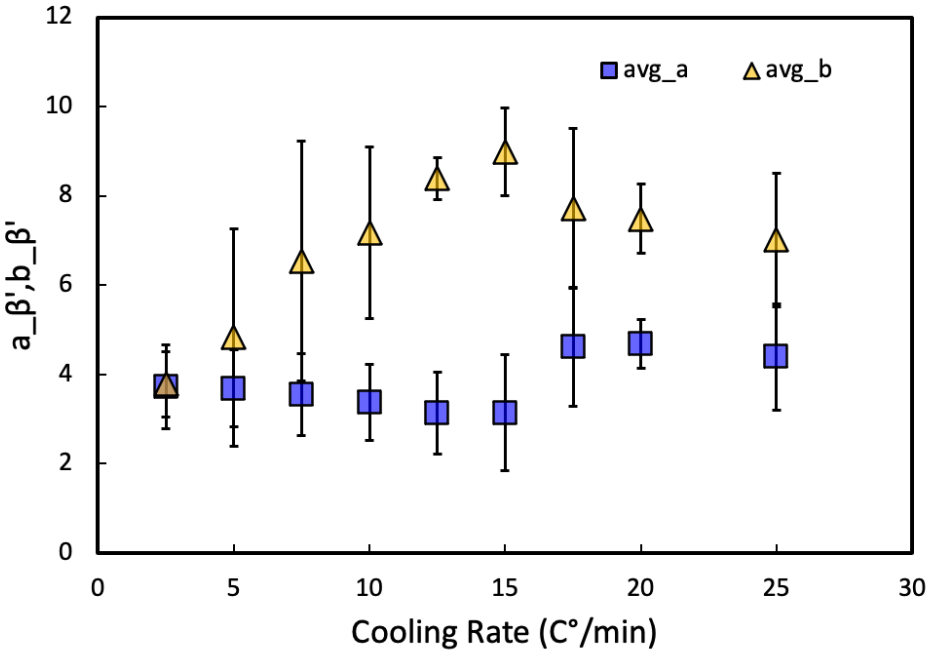

Figure 6-12 Fitting parameters ‘a’ and ‘b’, with 2σ error bars, for the β' polymorph versus cooling rate, including three pans.

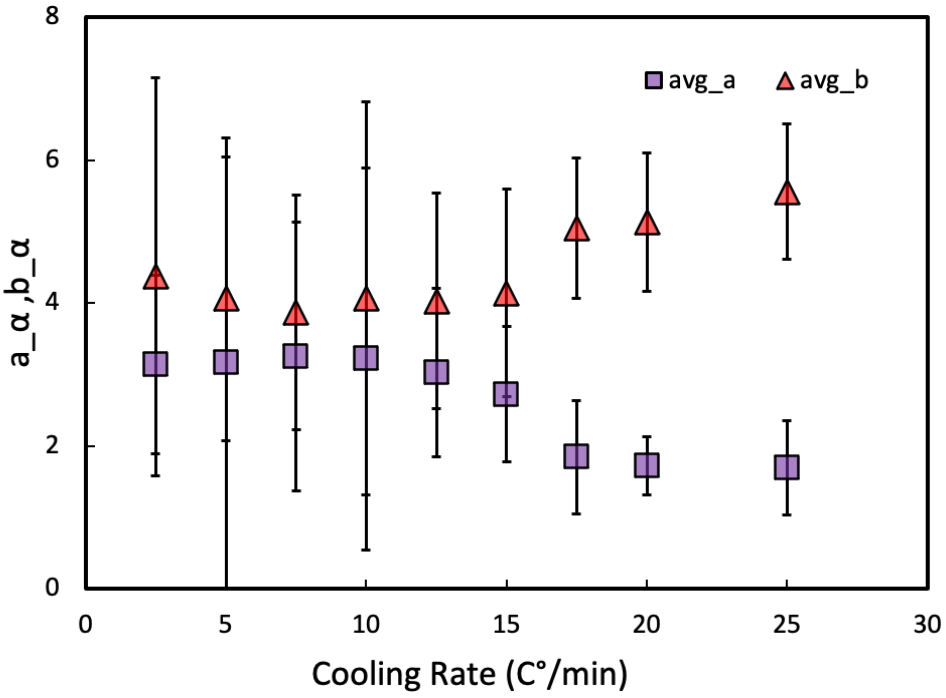

Figure 6-13 Fitting parameters ‘a’ and ‘b’, with 2σ error bars, for the α polymorph, as a function of cooling rate.

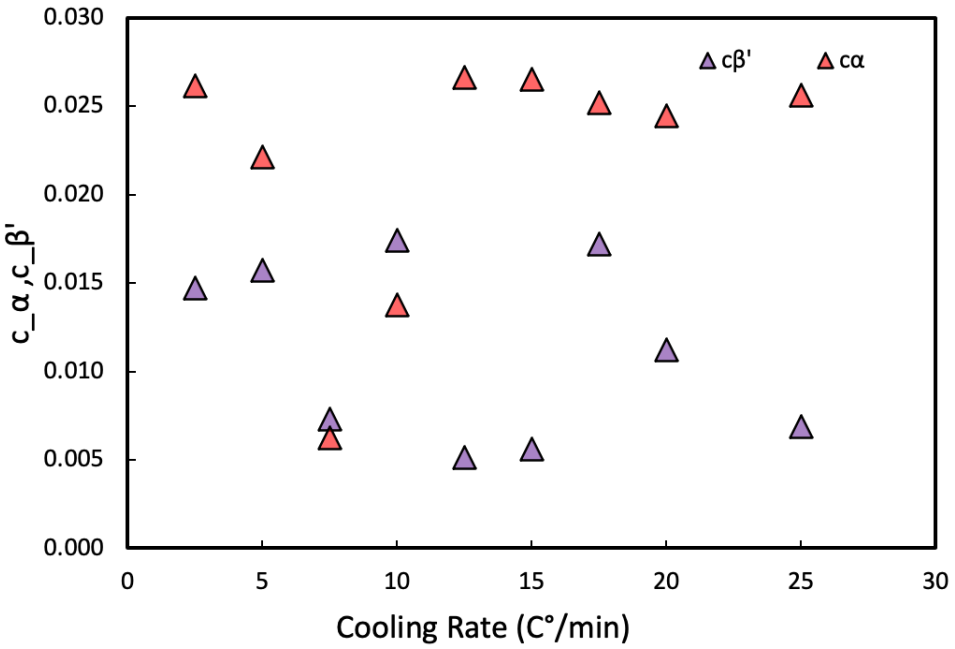

Figure 6-14 Fitting parameters 'c' for the α polymorph and β' as a function of cooling rate.

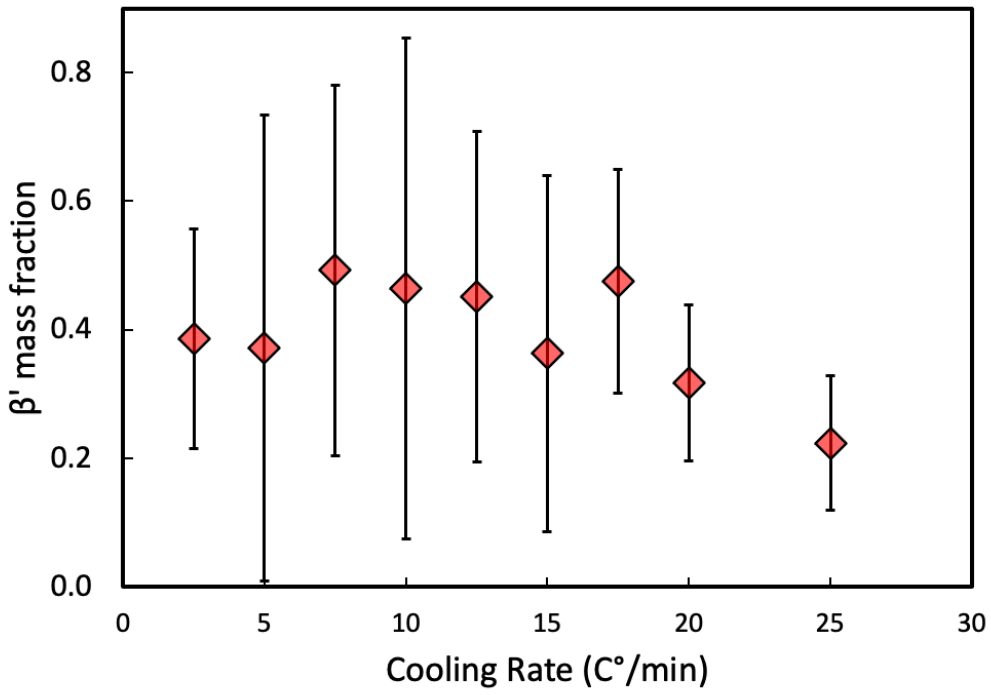

Figure 6-15 Fitted values of the β' polymorph mass fraction, $w_{\beta'}$, versus cooling rate.

CHAPTER 7 CONCLUSION AND FUTURE WORK

The first objective of this study is to investigate the effect of cooling rate on the onset temperature of the pure saturated triacylglycerols LLL, MMM, PPP, and SSS. For this, experiments were planned, optimized, and conducted using DSC equipment. A MATLAB code was developed to process the thermal analysis data from the DSC and obtain the onset temperature. The results show a near linear relationship between onset temperature and cooling rate for PPP, SSS, and LLL. However, the almost linear relationship of LLL has a steeper slope that PPP and SSS. The different slopes may be attributed to the formation of different polymorphs. At cooling rates between 2.5 and 10 C°/min, LLL and MMM have similar slopes and form similar polymorphs. However, PPP, SSS, and a section of MMM (between 10 and 25 C°/min) may form another polymorph. To ensure the data's consistency, we conducted a comparative experiment using different DSC instruments and pans, and discussed their effects.

To ascertain the polymorphic states that emerge under our experimental conditions, as well as the possibility of a phase transition, the analysis of X-ray data and comparison with DSC thermograms was done. The combination of DSC and XRD results show that the cooling rate changes the type and ratio of the crystallizing polymorphs of the triacylglycerols. At cooling rates between 2.5 to 25 °C /min, the α polymorph is formed for all triacylglycerols except MMM, which forms the β' polymorph at the lowest cooling rate. The XRD data for LLL shows that the β' polymorph crystallizes first, followed by the α polymorph at cooling rates between 5 to 25 °C /min. Observation of the ‘humps’ of the thermograms had led to the hypothesis that at least two polymorphs may be formed in some cases, and this was confirmed by the XRD data.

A MATLAB method was developed to estimate the onset of the second polymorph formed. It was aimed at locating the temperature of the second onset in the concurrent crystallization events. This method provides valuable data for modeling the crystallization temperature/time profile of a liquid triacylglycerol using the homogeneous nucleation theory of Turnbull and Fisher. DSC thermograms may display multiple melting-recrystallization peaks that can be identified through mathematical calculations and fitted using the extended Avrami function proposed in Equation 6-20. The fitting program requires input of β' onset temperature, a guess of the β' mass fraction, and initial conditions. Eight parameters are fitted in the program, including onset temperature, a, b, and c for α and a, b, and c for β', as well as the β' mass fraction, $w_{\beta'}$.

Further experiments can be conducted to verify the results of this study. A combined study of SR-XRD, small-angle X-ray scattering (SAXS), and wide-angle X-ray scattering (WAXS) with DSC can provide a more detailed understanding of the crystallization behavior of liquid triacylglycerols under various cooling rates. Additionally, the mathematical model developed in this study can be extended to other triacylglycerols and other organic compounds to predict their crystallization behavior under different cooling rates. Finally, the model can be used to optimize the processing conditions for the production of triacylglycerol-based products, such as food and pharmaceuticals.

BIBLIOGRAPHY

Ameh, E. S. (2019). A review of basic crystallography and X-ray diffraction applications. *International Journal of Advanced Manufacturing Technology*, *105*(7–8), 3289–3302. https://doi.org/10.1007/s00170-019-04508-1

Arirna, S., Ueno, S., Ogawa, A., & Sato, K. (2009). Scanning microbeam small-angle X-ray diffraction study of interfacial heterogeneous crystallization of fat crystals in oil-in-water emulsion droplets. Langmuir, 25(17), 9777–9784. https://doi.org/10.1021/la901115x

Arima, S., Ueji, T., Ueno, S., Ogawa, A., & Sato, K. (2007). Retardation of crystallization-induced destabilization of PMF-in-water emulsion with emulsifier additives. Colloids and Surfaces B: Biointerfaces, 55(1), 98–106. https://doi.org/10.1016/j.colsurfb.2006.11.025

Avrami, M. (1939). Kinetics of phase change. I: General theory. *The Journal of Chemical Physics*, *7*(12), 1103–1112. https://doi.org/10.1063/1.1750380

Avrami, M. (1940). Kinetics of phase change. II Transformation-time relations for random distribution of nuclei. *The Journal of Chemical Physics*, *8*(2), 212–224. https://doi.org/10.1063/1.1750631

Bailey, & Shahidi, F. (2005). Bailey's industrial oil & fats products. John Wiley & Sons.

Barasi, M. (2003). Human nutrition: a health perspective. CRC press.

Bayés-García, L., Calvet, T., Cuevas-Diarte, M. A., Ueno, S., & Sato, K. (2011a) In situ synchrotron radiation X-ray diffraction study of crystallization kinetics of polymorphs of 1,3-dioleoyl-2- palmitoyl glycerol (OPO). CrystEngComm. 13, 3592–99.

Bayés-García, L., Calvet, T., Cuevas-Diarte, M. A., Ueno, S., & Sato, K. (2013) In situ observation of transformation pathways of polymorphic forms of 1,3-dipalmitoyl-2-oleoyl glycerol (POP) examined with synchrotron radiation X-ray diffraction and DSC. CrystEngComm. 15, 302–14.

Bayés-García, L., Calvet, T., Cuevas-Diarte, M. A., Ueno, S., & Sato K. (2013b) Crystallization and transformation of polymorphic forms of trioleoyl glycerol and 1,2-dioleoyl-3-rac-linoleoyl glycerol. Journal of Physical Chemistry B. 117, 9170–81.

Bayés-García, L., Patel, A. R., Dewettinck, K., et al. (2015a) Lipid crystallization kinetics—roles of external factors influencing functionality of end products. Current Opinions in Food Science. 4, 32–38.

Bayés-García, L., Calvet, T., Cuevas-Diarte, M. A., Ueno, S., & Sato, K. (2015b) Phase behavior of binary mixture systems of saturated-unsaturated mixed-acid triacylglycerols: Effects of Glycerol structures and chain-chain interactions. Journal of Physical Chemistry B. 119, 4417–27.

Bayés-García, L., Calvet, T., Cuevas-Diarte, M. A., et al. (2015c) New textures of chocolate are formed by polymorphic crystallization and template effects: Velvet chocolate. Crystal Growth and Design. 15, 4045–54.

Bayés-García, L., Calvet, T., Cuevas-Diarte, M. A., & Ueno, S. (2016) In situ crystallization and transformation kinetics of polymorphic forms of saturated-unsaturated-unsaturated triacylglycerols: 1-palmitoyl-2,3-dioleoyl glycerol, 1-stearoyl-2,3-dioleoyl glycerol, and 1-palmitoyl-2-oleoyl-3-linoleoyl glycerol. Food Research International. 85, 244–58.

Boistelle, R. Fundamentals of nucleation and crystal growth. In: Crystallization and Polymorphism of Fats and Fatty Acids. Ed. Garti, N.; Sato, K. Marcel Dekker:New York, 189-226, 1988

Bolze, J., Kogan, V., Beckers, D., & Fransen, M. (2018). High-performance small- A nd wide-angle X-ray scattering (SAXS/WAXS) experiments on a multi-functional laboratory goniometer platform with easily exchangeable X-ray modules. Review of Scientific Instruments, 89(8). https:/doi.org/10.1063/1.5041949

Bouzidi, L., & Narine, S. S. (2010). Evidence of critical cooling rates in the nonisothermal crystallization of triacylglycerols: A case for the existence and selection of growth modes of a lipid crystal network. Langmuir, 26(6), 4311–4319. https://doi.org/10.1021/la903420n

Campos, R., Narine, S. S., & Marangoni, A. G. (n.d.). *Effect of cooling rate on the structure and mechanical properties of milk fat and lard*. www.elsevier.com/locate/foodres

Cebula, D. J., & Smith, K. W. (1991). Differential Scanning Calorimetry of Confectionery Fats. Pure Triacylglycerols: Effects of Cooling and Heating Rate Variation. In *JAOCS* (Vol. 68, Issue 8).

Danley, R. L. (2003). *New heat flux DSC measurement technique*. *Thermochimica Acta*, *395*(1-2), 201–208.

Domingues, M. A. F., Ribeiro, A. P. B., Kieckbusch, T. G. , Gioielli, L. A. , Grimaldi, R., Cardoso, L. P. , & Gonçalves, L. A. G. (2015). Advances in Lipids Crystallization Technology. In (Ed.), Advanced Topics in Crystallization. IntechOpen. https://doi.org/10.5772/59767

Erdemir, D., Lee, A. Y., & Myerson, A. S. (2009). Nucleation of crystals from solution: Classical and two-step models. Accounts of Chemical Research, 42(5), 621–629. https://doi.org/10.1021/ar800217x

Guthrie, S.E., Mazzanti, G., Marangoni, A., & Idziak, S. H. J. (2004). Implications of Orientation in Sheared Cocoa Butter. *Bulletin of the American Physical Society*, *49*(1).

Hampson, J.W., Rothbart, H.L. (1969). Heats of fusion for some triglycerides by differential scanning calorimetry. J Am Oil Chem Soc 46, 143–144. https://doi.org/10.1007/BF02635718

Hampson, & Rothbart, H. L. (1983). Triglyceride specific heat determined by differential scanning calorimetry. Journal of the American Oil Chemists' Society, 60(6), 1102–1104. https://doi.org/10.1007/BF02671334

Hartel, R. W. (2013). Advances in food crystallization. In Annual Review of Food Science and Technology (Vol. 4, Issue 1, pp. 277–292). https://doi.org/10.1146/annurev-food-030212-182530

Hartel, R.W. (2013). Advances in Crystallization in Foods. Annual Review of Food Science and Technology; 4(1) 277-292. DOI: 10.1146/annurev-food-030212-182530

Hartel, R.W. Crystallization in Foods. Aspen Publishers, Inc., Gaithersburg, MD, 2001.

Herrera, M. L., & Hartel, R. W. (2000). Effect of Processing Conditions on Physical Properties of a Milk Fat Model System: Microstructure (Vol. 77, Issue 11).

Himawan, C., Starov, V. M., & Stapley, A. G. F. (2006). Thermodynamic and kinetic aspects of fat crystallization. In Advances in Colloid and Interface Science (Vol. 122, Issues 1–3, pp. 3–33). https://doi.org/10.1016/j.cis.2006.06.016

Himawan, C., MacNaughtan, W., Farhat, I. A., & Stapley, A. G. F. (2007). Polymorphic occurrence and crystallization rates of tristearin/tripalmitin mixtures under non-isothermal conditions. European Journal of Lipid Science and Technology, 109(1), 49–60. https://doi.org/10.1002/ejlt.200600179

Kashchiev, D. (2000) Nucleation: Basic theory with applications. Oxford, UK: Butterworth-Heinemann.

Kashchiev, D., & van Rosmalen, G. M. (2003) Review: Nucleation in solutions revisited. Crystal Research and Technology. 38, 555–74.

Kalikmanov, V. I. (2013) Nucleation Theory: Lecture Notes in Physics, Vol. 860, Springer, Dodrecht, pp. 43– 53.

Kellens, M., Meeussen, W., Riekel, C., & Reynaers, H. (1990). Time resolved X-ray diffraction studies of the polymorphic behaviour of tripalmitin using synchrotron radiation. In Chemistry and Physics of Lipids (Vol. 52).

Kovalev, D. Y., & Ponomarev, V. I. (2019). Time-Resolved X-Ray Diffraction in SHS Research and Related Areas: An Overview. International Journal of Self-Propagating High-Temperature Synthesis, 28(2), 114–123. https://doi.org/10.3103/S1061386219020079

Lacmann, R., Herden, A., & Mayer, C. (1999). Kinetics of nucleation and crystal growth. In *Chemical Engineering and Technology* (Vol. 22, Issue 4, pp. 279–289). Wiley-VCH Verlag. https://doi.org/10.1002/(SICI)1521-4125(199904)22

Lawler, P.J.; Dimick, P.S. (2008) Crystallization and polymorphism of fats. In: Food lipids: chemistry, nutrition, and biotechnology. Ed. Akoh, C.C. CRC Press:Boca Raton,275-300, 2002. https://doi.org/10.1201/9781420046649

Limandri, S. P., Bonetto, R. D., di Rocco, H. O., & Trincavelli, J. C. (2008). Fast and accurate expression for the Voigt function. Application to the determination of uranium M linewidths. Spectrochimica Acta - Part B Atomic Spectroscopy, 63(9), 962–967. https://doi.org/10.1016/j.sab.2008.06.001

Marangoni, A. G., & Narine, Suresh. (2002). Physical properties of lipids. Marcel Dekker.

Marangoni, A. G., Tang, D., & Singh, A. P. (2006). Non-isothermal nucleation of triacylglycerol melts. Chemical Physics Letters, 419(1–3), 259–264. https://doi.org/10.1016/j.cplett.2005.11.085

Marangoni, A. G., Aurand, T. C., Martini, S., & Ollivon, M. (2006). A probabilistic approach to model the nonisothermal nucleation of triacylglycerol melts. Crystal Growth and Design, 6(5), 1199–1205. https://doi.org/10.1021/cg050630i

Marangoni, A., & Wesdorp, Leendert H. (2013). Structure and properties of fat crystal networks (2nd ed.). Boca Raton, Fla.: CRC Press.

Marangoni, A. (2017). Kinetic Analysis of Food Systems. 10.1007/978-3-319-51292-1.

Marangoni, A. G. (2017). Non-isothermal Nucleation Kinetics in Fats. In Kinetic Analysis of Food Systems (pp. 145–160). Springer International Publishing. https://doi.org/10.1007/978-3-319-51292-1_9

Martini, S., Herrera, M. L., & Hartel, R. W. (2001). Effect of cooling rate on nucleation behavior of milk fat - Sunflower oil blends. Journal of Agricultural and Food Chemistry, 49(7), 3223–3229. https://doi.org/10.1021/jf001101j

Martini, S., Herrera, M. L., & Hartel, R. W. (2002) Effect of cooling rate on crystallization behavior of milk fat fraction/sunflower oil blends. Journal of the American Oil Chemists' Society. 79, 1055–61

Martini, S., Suzuki, A. H., & Hartel, R. W. (2008). Effect of high intensity ultrasound on crystallization behavior of anhydrous milk fat. *JAOCS, Journal of the American Oil Chemists' Society*, *85*(7), 621–628. https://doi.org/10.1007/s11746-008-1247-5

Mazzanti, G., Guthrie, S. E., Sirota, E. B., Marangoni, A. G., & Idziak, S. H. J. (2003). Orientation and phase transitions of fat crystals under shear. *Crystal Growth and Design*, *3*(5), 721–725. https://doi.org/10.1021/cg034048a

Mazzanti, G., Li, M., Marangoni, A. G., & Idziak, S. H. J. (2011). Effects of shear rate variation on the nanostructure of crystallizing triacylglycerols. *Crystal Growth and Design*, *11*(10), 4544–4550. https://doi.org/10.1021/cg200786k

Metin, & Hartel, R. W. (2005). Crystallization of Fats and Oils. In Bailey's Industrial Oil and Fat Products. John Wiley & Sons, Ltd. https://doi.org/10.1002/047167849X.bio021

Minato A', A., Ueno, S., Yano, J., Wangb, Z. H., Seto, H., Amemiya, Y., & Sato, K. (1996a). Synchrotron Radiation X-ray Diffraction Study on Phase Behavior of PPP-POP Binary Mixtures (Vol. 73, Issue 11).

Minato A', A., Ueno, S., Yano, J., Wangb, Z. H., Seto, H., Amemiya, Y., & Sato, K. (1996b). Synchrotron Radiation X-ray Diffraction Study on Phase Behavior of PPP-POP Binary Mixtures (Vol. 73, Issue 11).

Minato, A., Ueno, S., Yano, J., Smith, K., Seto, H., Amemiya, Y., & Sato, K. (1997). Thermal and Structural Properties of sn-1,3-Dipalmitoyl-2-oleoylglycerol and sn-1,3-Dioleoyl-2-palmitoylglycerol Binary Mixtures Examined with Synchrotron Radiation X-Ray Diffraction (Vol. 74, Issue 10).

Mullin. (2001). Crystallization (4th ed.). Butterworth-Heinemann. https://doi.org/10.1016/B978-075064833-2/50008-5.

O'Brien, R.D. (2009). Fats and Oils: Formulating and Processing for Applications, Third Edition (3rd ed.). CRC Press. https://doi.org/10.1201/9781420061673

Reading, & Hourston, D. J. (2006). *Modulated temperature differential scanning calorimetry theoretical and practical applications in polymer characterisation*. Springer.

Rogers, M. A., Tang, D., Ahmadi, L., & Marangoni, A. G. (2008). Fat crystal networks. In Food Materials Science: Principles and Practice (pp. 369–414). Springer New York. https://doi.org/10.1007/978-0-387-71947-4_17

Rigolle, A., Foubert, I., Hettler, J., Verboven, E., Demuynck, R., & van den Abeele, K. (2015). Development of an ultrasonic shear reflection technique to monitor the crystallization of cocoa butter. *Food Research International*, *75*, 115–122. https://doi.org/10.1016/j.foodres.2015.05.059

Rigolle, A., Foubert, I., Hettler, J., Verboven, E., Martens, A., Demuynck, R., & van den Abeele, K. (2016). Insight in ultrasonic shear reflection parameters by studying temperature and limonene influence on cocoa butter crystallization. *Innovative*

Food Science and Emerging Technologies, *33*, 289–297. https://doi.org/10.1016/j.ifset.2015.12.004

Rye, G.G.; Liwinenko, J.W.; Marangoni, A.G. (2005). Fat crystal networks. in Bailey's Industrial Oil and Fat Products (Shahidi, F. ed.), John Wiley & Sons Inc., pp. 369-414. https://doi.org/10.1002/047167849X.bio008

Sato, K. (2001). Crystallization behaviour of fats and lipids * a review. In *Chemical Engineering Science* (Vol. 56).

Sato, K. (2018). Crystallization of lipids: Fundamentals and applications in food, cosmetics, and pharmaceuticals (First ed.). Hoboken, NJ, USA: Wiley.

Sato, K., Ueno, S., & Yano, J. (1999). Molecular interactions and kinetic properties of fats. Progress in lipid research, 38(1), 91–116. https://doi.org/10.1016/s0163-7827(98)00019-8

Sato, K. and Ueno, S. (2005). Polymorphism in Fats and Oils. In Bailey's Industrial Oil and Fat Products, F. Shahidi (Ed.). https://doi.org/10.1002/047167849X.bio020

Sato, K., Bayés-García, L., Calvet, T., Cuevas-Diarte, M. À., & Ueno, S. (2013). External factors affecting polymorphic crystallization of lipids. *European Journal of Lipid Science and Technology*, *115*(11), 1224–1238. https://doi.org/10.1002/ejlt.201300049

Small, D.M.(1986).*The Physical Chemistry of Lipids.* New York: Plenum Press.

Smith, K. W., Cain, F. W., & Talbot, G. (2005). Crystallization of 1,3-dipalmitoyl-2-oleoylglycerol and tripalmitoylglycerol and their mixtures from acetone. *European Journal of Lipid Science and Technology*, *107*(9), 583–593. https://doi.org/10.1002/ejlt.200501169

Smith, P., Shiori, T., Hondoh, H., Wallecan, J., & Ueno, S. (2022). Polymorphic and microstructural behaviors of palm oil/lecithin blends crystallized under shear. *JAOCS, Journal of the American Oil Chemists' Society*, *99*(8), 665–674. https://doi.org/10.1002/aocs.12628

Stanjek, H., & Häusler, W. (2004). Basics of X-ray Diffraction. In *Hyperfine Interactions* (Vol. 154).

Syamala, U. S. (2018). Calculation of MTDSC signals, factors effecting the signals and applications in drug development. *MOJ Bioequivalence & Bioavailability*, *5*(3). https://doi.org/10.15406/mojbb.2018.05.00095

Turnbull, D. (1950). Kinetics of heterogeneous nucleation. The Journal of Chemical Physics, 198–203. https://doi.org/10.1063/1.1747588

Takeguchi, S., Sato, A., Hondoh, H., Aoki, M., Uehara, H., & Ueno, S. (2020). Multiple β Forms of Saturated Monoacid Triacylglycerol Crystals. Molecules, 25(21). https://doi.org/10.3390/molecules25215086

Takeuchi, M., Ueno, S., & Sato, K. (2003). Synchrotron radiation SAXS/WAXS study of polymorph-dependent phase behavior of binary mixtures of saturated monoacid triacylglycerols. Crystal Growth and Design, 3(3), 369–374. https://doi.org/10.1021/cg025594r

Ueno, S., Ristic, R. I., Higaki, K., & Sato, K. (2003). In situ studies of ultrasound-stimulated fat crystallization using synchrotron radiation. *Journal of Physical Chemistry B*, *107*(21), 4927–4935. https://doi.org/10.1021/jp027840f

Yoshikawa, S., Kida, H., & Sato, K. (2015). Fat crystallization with talc particles is influenced by particle size, concentration, and cooling rate. *European Journal of Lipid Science and Technology*, *117*(6), 858–868. https://doi.org/10.1002/ejlt.201400420

Zhang, H., Zhao, H., Zhang, Y., Shen, Y., Su, H., Jin, J., Jin, Q., & Wang, X. (2018). Characterization of Positional Distribution of Fatty Acids and Triacylglycerol Molecular Compositions of Marine Fish Oils Rich in Omega-3 Polyunsaturated Fatty Acids. *BioMed Research International*, *2018*. https://doi.org/10.1155/2018/3529682

APPENDICES

Appendix A: Method log for DSC experimental analysis

Example from run 1 of LLL pan 1:

Method Log:
1: Sampling interval 0.20 sec/pt
2: Data storage: Off
3: Equilibrate at 120.00°C
4: Isothermal for 2.00 min
5: Ramp 30.00C°/min to -30.00°C
6: Isothermal for 1.00 min
7: Ramp 20.00C°/min to 120.00°C
8: Isothermal for 1.00 min
9: Equilibrate at 110.00°C
10: Data storage: On
11: Isothermal for 7.00 min
12: Mark end of cycle 0
13: Ramp 10.00C°/min to -30.00°C
14: Mark end of cycle 0
15: Isothermal for 3.00 min
16: Mark end of cycle 0
17: Ramp 10.00C°/min to 110.00°C
18: Mark end of cycle 0
19: Isothermal for 7.00 min
20: Mark end of cycle 0
21: Ramp 5.00C°/min to -30.00°C
22: Mark end of cycle 0
23: Isothermal for 3.00 min
24: Mark end of cycle 0
25: Ramp 10.00C°/min to 110.00°C
26: Mark end of cycle 0
27: Isothermal for 7.00 min
28: Mark end of cycle 0
29: Ramp 25.00C°/min to -30.00°C
30: Mark end of cycle 0
31: Isothermal for 3.00 min
32: Mark end of cycle 0
33: Ramp 10.00C°/min to 110.00°C
34: Mark end of cycle 0
35: Isothermal for 7.00 min
36: Mark end of cycle 0
37: Ramp 10.00C°/min to -30.00°C
38: Mark end of cycle 0
39: Isothermal for 3.00 min
40: Mark end of cycle 0
41: Ramp 10.00C°/min to 110.00°C
42: Mark end of cycle 0
43: Isothermal for 7.00 min
44: Mark end of cycle 0
45: Ramp 12.50C°/min to -30.00°C
46: Mark end of cycle 0
47: Isothermal for 3.00 min
48: Mark end of cycle 0
49: Ramp 10.00C°/min to 110.00°C
50: Mark end of cycle 0
51: Isothermal for 7.00 min
52: Mark end of cycle 0
53: Ramp 15.00C°/min to -30.00°C
54: Mark end of cycle 0
55: Isothermal for 3.00 min
56: Mark end of cycle 0
57: Ramp 10.00C°/min to 110.00°C
58: Mark end of cycle 0
59: Isothermal for 7.00 min
60: Mark end of cycle 0
61: Ramp 12.50C°/min to -30.00°C
62: Mark end of cycle 0
63: Isothermal for 3.00 min
64: Mark end of cycle 0
65: Ramp 10.00C°/min to 110.00°C
66: Mark end of cycle 0
67: Isothermal for 7.00 min
68: Mark end of cycle 0
69: Ramp 10.00C°/min to -30.00°C
70: Mark end of cycle 0
71: Isothermal for 3.00 min
72: Mark end of cycle 0
73: Ramp 10.00C°/min to 110.00°C
74: Mark end of cycle 0
75: Isothermal for 7.00 min
76: Mark end of cycle 0
77: Ramp 15.00C°/min to -30.00°C
78: Mark end of cycle 0
79: Isothermal for 3.00 min
80: Mark end of cycle 0
81: Ramp 10.00C°/min to 110.00°C
82: Mark end of cycle 0
83: Isothermal for 7.00 min
84: Mark end of cycle 0
85: Ramp 20.00C°/min to -30.00°C
86: Mark end of cycle 0
87: Isothermal for 3.00 min
88: Mark end of cycle 0
89: Ramp 10.00C°/min to 110.00°C
90: Mark end of cycle 0
91: Isothermal for 7.00 min
92: Mark end of cycle 0
93: Ramp 2.50C°/min to -30.00°C
94: Mark end of cycle 0
95: Isothermal for 3.00 min
96: Mark end of cycle 0
97: Ramp 10.00C°/min to 110.00°C
98: Mark end of cycle 0
99: Isothermal for 7.00 min
100: Mark end of cycle 0
101: Ramp 7.50C°/min to -30.00°C
102: Mark end of cycle 0
103: Isothermal for 3.00 min
104: Mark end of cycle 0
105: Ramp 10.00C°/min to 110.00°C
106: Mark end of cycle 0
107: Isothermal for 7.00 min
108: Mark end of cycle 0
109: Ramp 20.00C°/min to -30.00°C
110: Mark end of cycle 0
111: Isothermal for 3.00 min
112: Mark end of cycle 0
113: Ramp 10.00C°/min to 110.00°C
114: Mark end of cycle 0
115: Isothermal for 7.00 min
116: Mark end of cycle 0
117: Ramp 10.00C°/min to -30.00°C
118: Mark end of cycle 0
119: Isothermal for 3.00 min
120: Mark end of cycle 0
121: Ramp 10.00C°/min to 110.00°C
122: Mark end of cycle 0
123: Isothermal for 7.00 min
124: Mark end of cycle 0
125: Ramp 5.00C°/min to -30.00°C
126: Mark end of cycle 0
127: Isothermal for 3.00 min
128: Mark end of cycle 0
129: Ramp 10.00C°/min to 110.00°C
130: Mark end of cycle 0
131: Isothermal for 7.00 min
132: Mark end of cycle 0

133: Ramp 15.00C°/min to -30.00°C
134: Mark end of cycle 0
135: Isothermal for 3.00 min
136: Mark end of cycle 0
137: Ramp 10.00C°/min to 110.00°C
138: Mark end of cycle 0
139: Isothermal for 7.00 min
140: Mark end of cycle 0
141: Ramp 12.50C°/min to -30.00°C
142: Mark end of cycle 0
143: Isothermal for 3.00 min
144: Mark end of cycle 0
145: Ramp 10.00C°/min to 110.00°C
146: Mark end of cycle 0
147: Isothermal for 7.00 min
148: Mark end of cycle 0
149: Ramp 7.50C°/min to -30.00°C
150: Mark end of cycle 0
151: Isothermal for 3.00 min
152: Mark end of cycle 0
153: Ramp 10.00C°/min to 110.00°C
154: Mark end of cycle 0
155: Isothermal for 2.00 min
156: Mark end of cycle 0
157: End of method

Appendix B: Matlab code for detect the first onset temperature

```
function[OTF] = DSC_onset_Xinyue_LLL_Jun(Xfnm)


% Xfnm = 'LLL1_2000.xlsx';
[~,sheet_name]=xlsfinfo(Xfnm);

figure(1)
%  figure('Name','DataPlot','NumberTitle','off');
 hold on;

nums=numel(sheet_name);
OTF=zeros(nums,6);

% Temperature range for the TAG
% Onset range (by eye): SSS(49-51.5/52),PPP(38-42),MMM(26-32),LLL(8-17/18)
% input value of the highest temp of linear regression

 Thigh = 40;

% input value of the lowest temp of linear regression

 Tlow = 22;

% input value include real onset temp

 Tons = 8;
%
for k=1:numel(sheet_name)

  % 1. Regression operations
  snm=sheet_name{k};
  CR = str2double(snm(1:3))/10;
  REP = str2double(snm(4));
  data{k} = xlsread(Xfnm,snm);
  % fnm = strcat(Xfnm, snm);
  % reading data

  times=data{1,k}(:,1);
  temps=data{1,k}(:,2);
  hf=data{1,k}(:,3);

  if CR>=15
  Thigh = 30;
  Tlow = 20;
  end
  if CR<15&&CR>=10
  Thigh = 30;
  Tlow = 20;
  end
  if CR<10
  Thigh = 30;
  Tlow = 24;
  end
```

```
rg=find(temps<Thigh&temps>Tlow);% create new data set for fitting
dn=size(rg,1);    % total data number of culled data set
fnrg=rg(1,1);     % first number of range
lnrg=rg(1,1)+dn;  % last number of range

% Create the vectors with the culled data
Ntemps=temps(fnrg:lnrg);
Ntimes=times(fnrg:lnrg);
Nhf = hf(fnrg:lnrg);

mdl = fitlm(Ntemps,Nhf) ;% linear fit

cof=table2array(mdl.Coefficients);

slp=cof(2,1);
b=cof(1,1);

diff=Nhf-(slp*Ntemps+b);%yi-yc

sigma=sqrt((sum(diff.^2))/dn);

% 2. To find onset
rgo=find(temps<Tlow&temps>Tons);% new data set
dno=size(rgo,1);    % total data number of culled data set
fnrgo=rgo(1,1);     % first number of range
lnrgo=rgo(1,1)+dno;  % last number of range
% Create the vectors with the culled data use to find onset(temp beyond
% 3*sigma
Ntempso=temps(fnrgo:lnrgo);
% Ntimeso=times(fnrgo:lnrgo); not used
Nhfo = hf(fnrgo:lnrgo);
diffo=Nhfo-(slp*Ntempso+b);%yi-yc


%find onset!!!!

if  sigma<5e-05
ind_onset=find(abs(diffo)>30*sigma);
end
if  sigma>5e-05&&sigma<1e-04
ind_onset=find(abs(diffo)>11*sigma);
end
if  sigma>1e-04
ind_onset=find(abs(diffo)>10*sigma);
end

onset_temp=Ntempso(ind_onset(1));
onset_index=find(temps==onset_temp);


OTF(k,1) = CR; % cooling rate
OTF(k,2) = REP;% replicates
OTF(k,3) = onset_index;% sequence number of point of onset
OTF(k,4) = times(onset_index);% time of onset
OTF(k,5) = onset_temp; % onset
OTF(k,6) = hf(onset_index);% heat flow of onset
OTF(k,7) = sigma;

% Plot
figure(1)
% figure('Name','DataPlot','NumberTitle','off');
```

```
  hold on
  plot(temps,hf);
  plot(onset_temp,hf(onset_index),'b*');
  hold on
  title(Xfnm)
  xlabel('T(°C)');
  ylabel('Heatflow(W/g)');
  % axis([Tons Tlow -0.1 0.1]);
  hold on

  ind_diffo=Ntempso==onset_temp;
  figure(2)
  % figure('Name','Yc-Yo','NumberTitle','off');
  hold on
  scatter(Ntemps,diff,'.');
  scatter(Ntempso,diffo,'.')
  psx=[Tons,Thigh];
  psy=[3*sigma,3*sigma];
  hold on
  plot(psx,psy,'c--')
  title(Xfnm);
  xlabel('T(°C)');
  ylabel('Deviation(W/g)');
  axis([8 24 -0.002 0.01]);
  hold on
  plot(onset_temp,diffo(ind_diffo),'rd');
  hold on

  dirfigs='C:\Users\User\OneDrive - Dalhousie
University\DSC_data_Matlab_Xinyue_2021\Spreadsheets\Speadsheet_Mar_22\fig_Mar\L7';
  fignm=strcat(dirfigs,cell2mat(sheet_name(k)),'.png');
  fignm2=strcat(dirfigs,cell2mat(sheet_name(k)),'.png');
end
```

Appendix C: Onset temperature results from Matlab

LLL, MMM, PPP and SSS onset temperature detected by Matlab code, this data set is generated by DSC Q100 with standard hermetic aluminum pan from DSC consumable.

	LLL5			LLL6			LLL7			MMM4			MMM5			MMM6		
	Cooling_rate	Repetitions	Onset_Temp	Cooling_rate	Repetitions	Onset_Temp	Cooling_rate	Repetitions	Onset_Temp	Cooling_rate	lepetition	Onset_Temp	Cooling_rate	Repetitions	Onset_Temp	Cooling_rate	Repetitions	Onset_Temp
1	25	1	10.514	25	1	9.755	25	1	11.718	25	1	27.318	25	1	26.492	25	1	27.106
2	25	2	9.451	25	2	9.723	25	2	11.291	25	2	27.330	25	2	26.427	25	2	27.232
3	25	3	9.365	25	3	9.598	25	3	11.790	25	3	27.404	25	3	26.283	25	3	27.031
4	25	4	9.180	25	4	9.334	25	4	11.448	25	4	27.565	25	4	26.560	25	4	27.034
5	25	5	9.364	25	5	9.341	25	5	9.632	20	1	28.055	25	5	26.554	25	5	27.095
6	25	6	9.320	25	6	9.318	25	6	9.933	20	2	27.870	25	6	26.478	25	6	26.971
7	25	7	9.239	25	7	9.064	20	1	14.531	20	3	27.752	25	7	26.473	25	7	27.394
8	20	1	10.804	25	8	8.974	20	2	12.888	20	4	27.751	25	8	26.540	25	8	27.058
9	20	2	10.665	20	1	10.861	20	3	11.896	17.5	1	27.951	20	1	26.762	25	9	27.557
10	20	3	10.788	20	2	10.476	20	4	11.852	17.5	2	27.950	20	2	26.704	20	1	27.302
11	20	4	10.903	20	3	10.604	20	5	11.048	17.5	3	28.061	20	3	26.628	20	2	27.483
12	20	5	11.098	20	4	10.467	20	6	10.752	17.5	4	28.147	20	4	26.624	20	3	27.326
13	20	6	10.394	20	5	10.395	20	7	10.724	17.5	5	27.928	20	5	27.053	20	4	27.461
14	17.5	1	11.565	20	6	10.328	17.5	1	12.562	17.5	6	27.979	20	6	26.852	20	5	27.431
15	17.5	2	11.240	20	7	10.462	17.5	2	11.937	17.5	7	27.945	20	7	26.848	20	6	27.299
16	17.5	3	11.245	20	8	10.325	17.5	3	12.410	15	1	28.328	20	8	27.041	20	7	27.300
17	15	1	12.932	17.5	1	11.960	17.5	4	12.111	15	2	28.228	20	9	26.975	20	8	27.360
18	15	2	12.258	17.5	2	11.957	17.5	5	12.576	15	3	28.111	17.5	1	26.843	17.5	1	27.757
19	15	3	12.342	17.5	3	11.307	17.5	6	11.463	15	4	28.204	17.5	2	26.985	17.5	2	27.485
20	15	4	12.041	17.5	4	11.463	17.5	7	11.497	15	5	28.146	17.5	3	26.985	17.5	3	27.487
21	15	5	12.277	17.5	5	11.550	17.5	8	11.265	15	6	28.192	17.5	4	26.978	17.5	4	27.425
22	15	6	12.372	17.5	6	11.371	15	1	14.270	15	7	28.108	17.5	5	26.969	17.5	5	27.545
23	15	7	11.956	17.5	7	11.305	15	2	13.601	15	8	28.156	17.5	6	26.972	17.5	6	27.486
24	15	8	12.002	17.5	8	11.414	15	3	13.598	15	9	28.119	15	1	27.174	17.5	7	27.484
25	12.5	1	13.079	17.5	9	11.411	15	4	12.908	12.5	1	28.459	15	2	27.392	17.5	8	27.457
26	12.5	2	13.115	17.5	0	11.230	15	5	12.849	12.5	2	28.219	15	3	27.297	15	1	27.796
27	12.5	3	12.909	15	1	12.212	15	6	12.399	12.5	3	28.214	15	4	27.288	15	2	27.842
28	12.5	4	12.860	15	2	12.397	12.5	1	13.790	12.5	4	28.234	15	5	27.336	15	3	27.636
29	12.5	5	13.071	15	3	12.353	12.5	2	13.022	12.5	5	28.273	12.5	1	27.668	15	4	27.679
30	12.5	6	12.903	15	4	12.356	12.5	3	12.651	12.5	6	28.190	12.5	2	27.624	15	5	27.684
31	12.5	7	12.900	15	5	12.449	12.5	4	12.439	10	1	28.988	12.5	3	27.579	15	6	27.656
32	10	1	14.133	15	6	12.347	10	1	14.283	10	2	28.612	12.5	4	27.534	12.5	1	27.914
33	10	2	14.213	12.5	1	13.306	10	2	12.877	10	3	28.541	10	1	27.730	12.5	2	27.921
34	10	3	13.571	12.5	2	13.265	10	3	14.212	10	4	28.573	10	2	27.696	12.5	3	27.891
35	10	4	13.552	12.5	3	13.085	10	4	14.046	10	5	28.556	10	3	27.691	12.5	4	27.992
36	10	5	13.460	12.5	4	12.877	10	5	13.441	7.5	1	30.110	10	4	27.658	12.5	5	27.910
37	10	6	13.406	10	1	14.095	7.5	1	16.194	7.5	2	29.589	10	5	27.842	10	1	28.431
38	10	7	13.443	10	2	14.012	7.5	2	15.753	7.5	3	29.548	10	6	27.899	10	2	28.229
39	7.5	1	14.459	10	3	13.570	7.5	3	15.696	7.5	4	29.500	10	7	27.898	10	3	28.128
40	7.5	2	14.402	7.5	1	14.929	7.5	4	15.022	7.5	5	29.349	7.5	1	28.340	7.5	1	28.486
41	7.5	3	14.341	7.5	2	14.288	7.5	5	14.645	5	1	32.227	7.5	2	28.001	7.5	2	28.371
42	7.5	4	14.340	5	1	15.810	7.5	6	14.502	5	2	32.025	7.5	3	28.260	7.5	3	28.481
43	7.5	5	14.215	5	2	15.655	7.5	7	14.242	5	3	31.802	7.5	4	28.180	7.5	4	28.377
44	7.5	6	14.140	5	3	15.616	5	1	17.841	5	4	31.265	5	1	28.508	7.5	5	28.388
45	5	1	15.798	5	4	15.597	5	2	17.029	5	5	31.142	5	2	28.761	7.5	6	28.508
46	5	2	15.434	5	4	15.625	5	3	16.303	5	6	31.293	5	3	28.830	5	1	29.883
47	5	3	15.180	5	5	15.523	5	4	15.691	5	7	31.023	5	4	28.797	5	2	29.143
48	5	4	15.338	5	6	15.437	5	5	15.691	5	8	30.828	5	5	28.797	5	3	28.947
49	5	5	15.434	5	7	15.536	2.5	1	20.040	2.5	1	34.157	5	6	28.812	5	4	28.990
50	5	6	15.384	2.5	1	17.285	2.5	2	19.016	2.5	2	33.872	5	7	28.730	5	5	28.837
51	5	7	15.433	2.5	2	18.865	2.5	3	19.501	2.5	3	33.654	2.5	1	30.572	2.5	1	31.578
52	2.5	1	16.999	2.5	3	16.747	2.5	4	18.467	2.5	4	33.659	2.5	2	30.360	2.5	2	31.490
53	2.5	2	17.000	2.5	4	16.814	2.5	5	17.923	2.5	5	33.501	2.5	3	30.237	2.5	3	31.586
54	2.5	3	16.996	2.5	5	17.003	2.5	6	17.651	2.5	6	33.606	2.5	4	29.804	2.5	4	31.611
	PPP4			PPP5			PPP6			SSS5			SSS6			SSS7		
	Cooling_rate	Repetitions	Onset_Temp	Cooling_rate	Repetitions	Onset_Temp	Cooling_rate	Repetitions	Onset_Temp	Cooling_rate	lepetition	Onset_Temp	Cooling_rate	Repetitions	Onset_Temp	Cooling_rate	Repetitions	Onset_Temp
1	25	1	39.86685	25	1	39.84854	25	1	39.673	25	1	49.31931	25	1	49.7404	25	1	49.6359
2	25	2	39.85124	25	2	39.8261	25	2	37.7796	25	2	49.37161	25	2	49.5956	25	2	49.7639
3	25	3	39.78806	25	3	39.82772	25	3	39.74059	25	3	49.33472	25	3	49.7452	25	3	49.71757
4	25	4	39.77355	25	4	39.86634	25	4	39.74806	25	4	49.41526	25	4	49.70315	25	4	49.68007
5	25	5	39.76729	25	5	39.99414	25	5	39.81182	25	5	49.37439	25	5	49.65438	25	5	49.6784
6	25	6	39.74783	25	6	39.90734	25	6	39.80271	25	6	49.66172	25	6	49.69336	25	6	49.68298
7	25	7	39.74488	25	7	39.9025	25	7	39.79831	25	7	49.6094	20	1	49.9538	25	7	49.68306
8	20	1	40.1506	20	1	40.26163	20	1	40.0626	20	1	49.72434	20	2	49.8846	25	8	49.7611
9	20	2	40.04584	20	2	40.19492	20	2	40.05586	20	2	49.7224	20	3	49.8962	20	1	49.9089
10	20	3	40.0911	20	4	40.23125	20	3	40.07661	20	3	49.723	20	4	49.89736	20	2	50.00561
11	20	4	40.07688	20	3	40.16841	20	4	40.11446	20	4	49.73628	20	5	49.89316	20	3	50.00813
12	20	5	40.0711	20	5	40.23397	20	5	40.11298	20	5	49.7373	20	6	49.92716	20	4	50.03144
13	20	6	40.00484	20	6	40.26317	17.5	1	40.18399	20	6	49.99926	20	7	49.96168	20	5	49.98544
14	20	7	40.00286	20	7	40.26237	17.5	2	40.224	20	7	50.0016	17.5	1	50.0606	20	6	50.01623
15	20	8	39.99597	20	8	40.75745	17.5	3	40.28448	17.5	1	49.99952	17.5	2	50.0719	20	7	50.0134
16	17.5	1	40.4241	17.5	1	40.25434	17.5	4	40.27746	17.5	2	49.92132	17.5	3	50.1083	17.5	1	50.1432
17	17.5	2	40.3102	17.5	2	40.33523	17.5	5	40.2771	17.5	3	49.94522	17.5	4	50.0806	17.5	2	50.186
18	17.5	3	40.20556	17.5	3	40.45062	17.5	6	40.27902	17.5	4	50.17484	17.5	5	50.12388	17.5	3	50.15538
19	17.5	4	40.23894	17.5	4	40.38191	17.5	7	40.33562	17.5	5	50.14645	17.5	6	50.09422	17.5	4	50.18254
20	17.5	5	40.17798	17.5	5	40.40939	15	1	40.45955	15	1	50.13306	17.5	7	50.05848	17.5	5	50.16084
21	17.5	6	40.18309	17.5	6	40.46671	15	2	40.44772	15	2	50.15136	17.5	8	50.02881	17.5	6	50.18978
22	17.5	7	40.17705	15	1	40.52002	15	3	40.43731	15	3	50.11068	17.5	9	50.11275	17.5	7	50.15961
23	17.5	8	40.17956	15	2	40.54715	15	4	40.47712	15	4	50.13236	15	1	50.3571	15	1	50.3357
24	15	1	40.5252	15	3	40.58015	15	5	40.45526	15	5	50.30445	15	2	50.23496	15	2	50.375
25	15	2	40.45887	15	4	40.63034	15	6	40.4557	15	6	50.35222	15	3	50.22959	15	3	50.4663
26	15	3	40.43015	15	5	40.57735	15	7	40.49404	12.5	1	50.36773	15	4	50.2501	15	4	50.4187
27	15	4	40.35922	15	6	40.50122	15	8	40.49338	12.5	2	50.29978	15	5	50.274	15	5	50.4135
28	12.5	1	40.8598	12.5	1	40.75765	15	9	40.48903	12.5	3	50.32488	15	6	50.27447	15	6	50.30066
29	12.5	2	40.67918	12.5	2	40.73648	15	0	40.4905	12.5	4	50.30816	12.5	1	50.5012	15	7	50.34082
30	12.5	3	40.68495	12.5	3	40.7765	12.5	1	40.6699	12.5	5	50.3023	12.5	2	50.40488	15	8	50.33744
31	12.5	4	40.66903	12.5	4	40.75342	12.5	2	40.70392	12.5	6	50.32338	12.5	3	50.41906	12.5	1	50.6822
32	12.5	5	40.62313	12.5	5	40.75745	12.5	3	40.70484	12.5	7	50.38535	10	1	50.6626	12.5	2	50.5093
33	12.5	6	40.62126	12.5	6	40.80051	10	1	40.86698	12.5	8	50.51219	10	2	50.6826	12.5	3	50.51122
34	10	1	41.05956	10	1	40.9271	10	2	40.89974	10	1	50.56246	10	3	50.59731	12.5	4	50.53526
35	10	2	40.98957	10	2	40.89688	10	3	40.88211	10	2	50.56518	10	4	50.60724	10	1	50.8526
36	10	3	40.88524	10	3	40.95698	10	4	40.90355	10	3	50.51218	7.5	1	50.8662	10	2	50.7798
37	10	4	40.84757	10	4	40.91142	10	5	40.90225	10	4	50.54586	7.5	2	50.8971	10	3	50.68492
38	10	5	40.74535	7.5	1	41.12143	10	6	40.93463	10	5	50.64458	7.5	3	50.8942	10	4	50.76438
39	7.5	1	41.00207	7.5	2	41.11228	7.5	1	41.0871	10	6	50.64581	7.5	4	50.9092	7.5	1	51.0403
40	7.5	2	41.22655	7.5	3	41.12344	7.5	2	41.1078	10	7	50.59631	7.5	5	50.79986	7.5	2	50.914
41	7.5	3	41.17239	7.5	4	41.15463	5	1	41.35304	7.5	1	50.78258	7.5	6	50.82059	7.5	4	50.94548
42	7.5	4	41.11755	7.5	5	41.25982	5	2	41.3651	7.5	2	50.75439	5	1	51.1349	7.5	3	50.93248
43	7.5	5	41.09394	7.5	6	41.16094	5	3	41.40234	7.5	3	50.79048	5	2	51.122	5	1	51.335
44	7.5	6	41.05616	5	1	41.32233	5	4	41.43328	7.5	4	50.89226	5	3	51.04216	5	2	51.3026
45	7.5	7	40.96653	5	2	41.36609	5	5	41.39924	7.5	5	50.86613	5	4	51.05716	5	3	51.2259
46	5	1	41.49586	5	3	41.3624	5	6	41.42839	5	1	51.11416	5	5	50.98985	5	4	51.18563
47	5	2	41.27503	5	4	41.3735	5	7	41.44561	5	2	51.04942	5	6	51.04102	5	5	51.16238
48	5	3	41.27036	5	5	41.38645	5	8	41.41194	5	3	51.03024	2.5	1	51.36796	5	6	51.16998
49	5	4	41.23644	5	6	41.38441	5	9	41.46374	5	4	51.01937	2.5	2	51.3328	5	7	51.17492
50	2.5	1	41.57144	2.5	1	41.72616	5	0	41.41148	5	5	51.02041	2.5	3	51.31641	5	8	51.1455
51	2.5	2	41.5385	2.5	2	41.75552	2.5	1	41.78699	5	6	51.17016	2.5	4	51.36455	2.5	1	51.5343
52	2.5	3	41.52679	2.5	3	41.7062	2.5	2	41.7294	2.5	1	51.46578	2.5	5	51.3689	2.5	2	51.45222
53	2.5	4	41.50678	2.5	4	41.7193	2.5	3	41.75106	2.5	2	51.43924	2.5	6	51.35312	2.5	3	51.41596
54	2.5	5	41.50628	2.5	5	41.75646	2.5	4	41.77963	2.5	3	51.28716	2.5	7	51.32238	2.5	4	51.4589

Onset temperature of LLL from comparative experiment using same pan and same method in two different instruments, DSC Q100 and DSC Q2000.

DSC Q100									DSC Q2000								
LLL1			LLL2			LLL3			LLL1			LLL2			LLL3		
Cooling_rate	Repetitions	Onset_Temp	Cooling_rate	Repetitions	Onset_Temp	Cooling_rate	Repetitions	Onset_Temp	Cooling_rate	Repetitions	Onset_Temp	Cooling_rate	Repetitions	Onset_Temp	Cooling_rate	Repetitions	Onset_Temp
25	1	13.207	25	1	13.841	25	1	11.990	25	1	16.452	25	1	16.247	25	1	16.082
25	2	12.818	25	2	13.904	25	2	12.168	25	2	15.086	25	2	15.666	25	2	15.916
25	3	12.726	25	3	13.653	25	3	12.731	25	3	15.003	25	3	14.948	25	3	15.747
25	4	12.010	25	4	13.279	25	4	12.381	25	4	14.924	25	4	14.530	25	4	14.866
25	5	12.239	25	5	13.183	25	5	12.434	25	5	14.670	25	5	14.363	25	5	14.768
25	6	12.332	25	6	12.855	25	6	12.281	25	6	14.622	25	6	14.195	25	6	14.519
25	7	12.348	25	7	11.823	20	1	13.942	25	7	14.882	25	7	14.858	20	1	17.680
20	1	14.622	25	8	12.009	20	2	13.412	20	1	16.958	25	8	15.026	20	2	16.709
20	2	14.599	20	1	14.934	20	3	14.181	20	2	17.023	20	1	16.912	20	3	15.606
20	3	14.399	20	2	14.772	20	4	13.826	20	3	16.249	20	2	15.475	20	4	15.807
20	4	14.475	20	3	14.552	20	5	13.638	20	4	16.248	20	3	15.475	20	5	15.800
20	5	14.342	20	4	14.349	20	6	13.619	20	5	16.315	20	4	15.339	20	6	16.127
20	6	13.883	20	5	13.848	20	7	13.898	20	6	16.349	20	5	15.403	20	7	16.129
17.5	1	14.567	20	6	13.802	17.5	1	14.684	17.5	1	16.407	20	6	15.737	17.5	1	16.600
17.5	2	14.579	20	7	13.629	17.5	2	14.258	17.5	2	16.729	20	7	16.004	17.5	2	16.366
17.5	3	14.304	20	8	13.129	17.5	3	14.309	17.5	3	16.495	20	8	16.201	17.5	3	16.192
15	1	15.941	17.5	1	14.456	17.5	4	16.693	15	1	18.136	17.5	1	18.336	17.5	4	16.428
15	2	15.978	17.5	2	15.853	17.5	5	14.086	15	2	18.146	17.5	2	17.864	17.5	5	16.369
15	3	15.986	17.5	3	15.747	17.5	6	14.374	15	3	17.933	17.5	3	17.570	17.5	6	16.535
15	4	15.873	17.5	4	15.504	17.5	7	14.606	15	4	17.361	17.5	4	17.162	17.5	7	16.300
15	5	15.237	17.5	5	15.642	17.5	8	14.428	15	5	17.163	17.5	5	16.894	17.5	8	16.241
15	6	15.106	17.5	6	15.182	15	1	15.472	15	6	16.966	17.5	6	16.193	15	1	18.735
15	7	15.062	17.5	7	15.116	15	2	15.069	15	7	16.886	17.5	7	16.250	15	2	18.337
15	8	15.426	17.5	8	14.330	15	3	15.093	15	8	17.288	17.5	8	16.425	15	3	17.355
12.5	1	16.634	17.5	9	14.039	15	4	15.242	12.5	1	18.971	17.5	9	16.599	15	4	16.579
12.5	2	16.716	17.5	0	14.426	15	5	15.593	12.5	2	18.559	17.5	0	16.830	15	5	16.831
12.5	3	16.799	15	1	16.463	15	6	15.136	12.5	3	18.933	15	1	18.211	15	6	16.880
12.5	4	16.446	15	2	16.515	12.5	1	16.088	12.5	4	18.200	15	2	18.212	12.5	1	17.716
12.5	5	16.151	15	3	16.067	12.5	2	16.127	12.5	5	17.827	15	3	16.632	12.5	2	17.879
12.5	6	16.167	15	4	15.503	12.5	3	16.082	12.5	6	17.869	15	4	16.678	12.5	3	17.795
12.5	7	15.925	15	5	14.951	12.5	4	16.000	12.5	7	17.704	15	5	17.029	12.5	4	17.501
10	1	16.758	15	6	15.415	10	1	17.486	10	1	20.121	15	6	17.375	10	1	20.124
10	2	17.620	12.5	1	17.226	10	2	17.448	10	2	19.690	12.5	1	18.997	10	2	18.585
10	3	17.666	12.5	2	16.967	10	3	16.934	10	3	19.430	12.5	2	17.802	10	3	18.286
10	4	17.643	12.5	3	15.715	10	4	17.005	10	4	19.227	12.5	3	17.798	10	4	18.287
10	5	16.742	12.5	4	15.767	10	5	17.068	10	5	18.408	12.5	4	17.923	10	5	18.445
10	6	16.936	10	1	17.875	7.5	1	18.492	10	6	18.258	10	1	19.945	7.5	1	20.516
10	7	16.860	10	2	18.013	7.5	2	18.037	10	7	18.294	10	2	19.406	7.5	2	19.777
7.5	1	18.364	10	3	16.873	7.5	3	17.963	7.5	1	20.271	10	3	18.785	7.5	3	19.773
7.5	2	18.509	7.5	1	18.484	7.5	4	18.828	7.5	2	19.869	7.5	1	21.233	7.5	4	19.413
7.5	3	17.700	7.5	2	17.797	7.5	5	16.745	7.5	3	19.181	7.5	2	19.087	7.5	5	19.059
7.5	4	17.874	5	1	20.142	7.5	6	18.415	7.5	4	19.342	5	1	21.703	7.5	6	19.409
7.5	5	18.071	5	2	20.112	7.5	7	18.196	7.5	5	19.117	5	2	21.285	7.5	7	19.258
7.5	6	17.797	5	3	19.974	5	1	19.332	7.5	6	18.993	5	3	21.150	5	1	21.745
5	1	19.457	5	4	20.254	5	2	19.594	5	1	21.861	5	4	21.200	5	2	20.866
5	2	19.770	5	4	20.233	5	3	19.216	5	2	20.942	5	4	20.925	5	3	20.354
5	3	19.598	5	5	20.330	5	4	19.395	5	3	20.499	5	5	20.556	5	4	20.336
5	4	19.091	5	6	19.750	5	5	19.352	5	4	19.993	5	6	20.423	5	5	20.217
5	5	19.149	5	7	19.613	2.5	1	20.735	5	5	19.829	5	7	20.255	2.5	1	23.123
5	6	19.385	2.5	1	21.632	2.5	2	20.848	5	6	20.342	2.5	1	22.155	2.5	2	23.270
5	7	19.622	2.5	2	21.601	2.5	3	21.011	5	7	20.042	2.5	2	21.843	2.5	3	22.438
2.5	1	21.362	2.5	3	21.505	2.5	4	20.826	2.5	1	22.362	2.5	3	21.601	2.5	4	22.019
2.5	2	20.970	2.5	4	21.152	2.5	5	20.988	2.5	2	21.451	2.5	4	21.925	2.5	5	21.606
2.5	3	20.967	2.5	5	21.046	2.5	6	20.939	2.5	3	21.626	2.5	5	21.933	2.5	6	21.932

Appendix D: MATLAB code for detect the second onset

```
function[Esthf,ftcpl,ftcps,ftcoeff,Onseta] = Avr_t_L_v12(DSC_data,T_onset,ini_guess,Maxv,DSCset,setrange)
% Xinyue Zhang, Omar AlQatami & Gianfranco Mazzanti
%
%  * Version dates
%  2022-05-01 - 07 -2022_Aug,Sep,Oct - 2023 Feb/Mar/Apr -Version 12.0
%   Adjusted estimate of T_onset_1 to the data set
%   Uses the vector T_onset(nums,1) as required input
%   Includes fitting cp parameters from L and S, not in crystallization
%   Uses fmincon and includes linear and non-linear constraints
%       from the first and second derivatives
%   Allows for sets with one maximum or with two maxima & one minimum
%   Fits all CR
%% 0. Parameters

%   0.1. INPUT

%   DSC_data,       Name of the Excel file with the data
%   T_onset,        Vector with the onsets for betaprime
%   ini_guess,      Array(9,8) with rows of the guess of 8 parameter for
%                   each of the 9 cooling rates :
          %   ROWS correspond to the cooling rate
          %   25,20,17.5,15,12.5,10,7.5,5,2.5 in that order
          %   COLUMNS
          %   1 a for betaprime
          %   2 b for betaprime
          %   3 cm for betaprime (>1)
          %   4 a for alpha
          %   5 b for alpha
          %   6 cm for alpha (>1)
          %   7 To for alpha
          %   8 Mass fraction of betaprime 0<bpfr<1

%   Maxv,           Structure 54x3 with maximum(1) or maxima(3). Each
%                   column is for one of the DSCsets (1 to 3)
%   DSCset,         Numer of the set (pan) being run, (1 to 3)
%   setrange,       Runs to be included in the fitting e.g. 27:32


%   0.2. OUTPUT

%   Esthf,          Structure with nptsx6 in each cell:
          %   ROWS correspond to data points for the run
          %
          %   COLUMNS
          %   1 Data times culled
          %   2 Data temperatures culled
          %   3 Data heat flow culled
          %   4 Calculated heat flow
          %   5 Residuals
          %   6 Calculated Baseline
%   ftcpl,      cp coeffcients for the liquid for each run
%   ftcps,      cp coeffcients for the solid for each run
%   ftcoeff,    Structure with coefficients and other results
          %   ROWS correspond to runs (1 to 54) on the DSCset
          %
          %   COLUMN CELLS
          %   1 Coefficients fitted for the run (coefav)
```

```
                        %   1 a for betaprime
                        %   2 b for betaprime
                        %   3 cm for betaprime
                        %   4 a for alpha
                        %   5 b for alpha
                        %   6 cm for alpha
                        %   7 To for alpha
                        %   8 Mass fraction of betaprime
          %   2 fval,     Minimized value of the objective function
          %   3 exitflag, Flag for the type of exit from fmincon
          %   4 output,   Message from fmincon
          %   5 lambda,   Linear and Nonlinear constraints values
          %   6 grad,     gradient of fval wrt to parameters at the min
          %   7 hessian,  Real part of the hessian matrix 8x8
          %   8 bp fraction
          %   9 not used
          %   10 Cooling rate of the run, K/min
          %   11 T_onset_bp
          %   12 not used
          %
%   Onseta,         Vector with the Tonset for alpha
%% 1. Initial commands in driver script
% 1.1. Before running do the commands in the "Driver_Avrami_ext_v4.m"
%       driver script to prepare the data from each DSCset:
%
% DSC SET TO FIT
   % DSCset=1;
   % setstr=num2str(DSCset,'%1u');
   %
   % load(strcat('T_onset_LLL',setstr,'_Q100.mat'));
   % DSC_data = strcat('LLL',setstr,'_Q100.xlsx');
   % load(strcat('inital_guess_L',setstr,'_Q100.mat'));
   % load(strcat('IP_',setstr,'_new'));
   % load('Max.mat');
   % if DSCset==1
   %     Coepo_1=zeros(54,8);
   % elseif DSCset==2
   %     Coepo_2=zeros(54,8);
   %
   % elseif DSCset==3
   %     Coepo_3=zeros(54,8);
   % end
   % Maxv=Max;
% ============================================

% 1.2. Specifiy options for the fmincon solver
optx=optimoptions('fmincon','Algorithm','sqp',...
   'FunctionTolerance',1.00e-07,'OptimalityTolerance',1.00e-07);

% 1.3. READ the EXCEL spreadsheet with the data

[~,sheet_name]=xlsfinfo(DSC_data);

% 1.4. Define some operating variables
setstr=num2str(DSCset,'%1u'); % create string for the DSCset number
% Define directory
dirfigs='C:\Users\mazza\OneDrive - Dalhousie University\DSC_data_Matlab_Xinyue_2021\JACS
paper\Part_2\Matlabcode_uptodate\L1';
% dirfigs='C:\DATA\A_Students\Zhang_Xinyue\Onset_T\L1';

% Create a cell arrays that contains a total of the same number of doubles
```

```
% as sheet numbers
Onseta=zeros(54,1);   %Create vetor to return onset temperatures of alpha
nums=numel(sheet_name);
Esthf=cell(nums,1); % Structure to return culled data (t,T,hf)and calculated hf
ftcpl=cell(nums,1); % Parameters for the liquid cp
ftcps=cell(nums,1); % Parameters for the mixed solid cp
ftcoeff=cell(nums,12); % Parameters from the overall fit

%% 2. Cycle through the data sets
% Section xyz
% CR_a is the cooling rate where alpha no longer appears, if there is
% however, sometimes alpha does appear. The fit with bp alone will
% make it more clear in the plot...

CR_a = 1.0;
% 2.1. Ratio of specific heat linear parameters
% ---------
% Linear approximation for the upper temperature range
a_L_0lin =0.009523; a_L_1lin =-0.8359948;
bp_L_0lin =0.008256; bp_L_1lin =-0.7285608;

% -------
% r_o ratio of intercepts of alpha/betaprime
r_o =        a_L_0lin/bp_L_0lin;% 1.153437658;

% r_1 ratio of slopes of alpha/betaprime
r_1 = a_L_1lin/bp_L_1lin;% 1.147460644;

%2.2. Other Thermal parameters

%heat capacity   J/(g·K) These are for T in Kelvin

l_L_0 =1.2; l_L_1 =0.025;  l_L_2 =4.5E-05;

% a_L_0 =2.55; a_L_1 =-0.016; a_L_2 =4.9E-05;

% bp_L_0=3.45; bp_L_1=-0.023; bp_L_2=5.7E-04;

% Melting point
TMa=288.75;           TMbp=308.25;TMbpC=TMbp-273.15;

%enthalpy J/g

enth_a=109.23; enth_bp=134.58;
deltaTmax_bp=56;% melting point bp to -20C
deltaTmax_a=36;% melting point a to -20C
% To cycle trhough all the data sets, we use numel(sheet_name) at end of 'for'
% numel(sheet_name) % otherwise we use the range provided in the parameters
% 2.3. ******************   RANGE   *******************
for k= setrange %

   % 2.3.1. Regression operations
   snm=sheet_name{k};              % name of the set
   CR = str2double(snm(1:3))/10;   % Cooling rate in C/min
   ftcoeff(k,10)={CR};             % Store the CR for output
   crs = CR/60.0;                  % Cooling rate in C/s

   if (CR==25)
      cr_n=1;
   else
      cr_n = round(10-0.4*CR,0);
```

```
end


% 2.3.3. T onset for bp from data
T_onset_bp =T_onset(k,1); % From previous analysis


% 2.3.4.Read the data from the Excel spreadsheet
% REP = str2double(snm(4)); % Replicate number for the CR for the pan

% 2.3.4.1 Read full data set
data{k} = xlsread(DSC_data,snm); %#ok<AGROW> % Read the data for the run
% Separate the data sets into three vectors
times=data{1,k}(:,1);   % Times, running along the experiment
temps=data{1,k}(:,2);   % Temperatures in C
hf=data{1,k}(:,3);      % Heat Flow in W/g
% Find timestamp for melting point t_Tm
ix=sum(temps>TMbpC);
t_Tm=times(ix)+(times(ix)-times(ix+1))/(temps(ix)-temps(ix+1))...
    *(temps(ix)-TMbpC);

% 2.3.4.2. Segment data for fit using temperature ranges
Tstart=round(T_onset_bp + 5.0,1);
Tend=round(2.14-0.86*CR + 5,1);
if (CR==25)
    Tend=-10;
end

% 2.3.4.3. create new data set
rg_av=find(temps<=T_onset_bp&temps>Tend);          %for Avarmi fitting
rg_cpl=find(temps>(Tstart)&temps<(Tstart+5)); %for Cp liquid fitting
rg_cps=find(temps<(Tend)&temps>(Tend-5));     %for Cp solid fitting

% 2.3.4.4. total data number of culled data set
dng=size(rg_av,1);
dnl=size(rg_cpl,1);
dns=size(rg_cps,1)-1;

% 2.3.4.5. first number of range
fnrg=rg_av(1,1);
fnrgl=rg_cpl(1,1);
fnrgs=rg_cps(1,1);

% 2.3.4.6. last number of range
lnrg=rg_av(1,1)+dng;
lnrgl=rg_cpl(1,1)+dnl;
lnrgs=rg_cps(1,1)+dns;

% 2.3.4.7. Create the vectors with the culled data. Set t_zero = t_Tm
avtemps=temps(fnrg:lnrg);
avtimes=times(fnrg:lnrg)-t_Tm;

% VERY IMPORTANT: Create the IDEAL temperature ramp to be used
% for the fit

avtemps_c=avtemps(1)-CR*(avtimes-avtimes(1));
avhf = hf(fnrg:lnrg);

% 2.3.4.8. Liquid data for baseline
ltemps_o=temps(fnrgl:lnrgl);
ltimes=times(fnrgl:lnrgl)-t_Tm;
```

```
ltemps = ltemps_o(1)-CR*(ltimes-ltimes(1));
lhf = hf(fnrgl:lnrgl);

% 2.3.4.9. Solid data for baseline
stemps_o=temps(fnrgs:lnrgs);
stimes=times(fnrgs:lnrgs)-t_Tm;
stemps = stemps_o(1)-CR*(stimes-stimes(1));
shf = hf(fnrgs:lnrgs);

% 2.3.6. Growth function initial guesses
%% Ampl_a=abp_f*Ampl_bp;
% Beta prime polymorph

% 2.3.6.1. yci is the index for the cooling rate guesses
if CR==25
   yci=1.0;
else
   yci=10-0.4*CR;
end

% 2.3.6.2. Get the guesses from the array
avA_bp=ini_guess(yci,1);
avB_bp=ini_guess(yci,2);
avB1m_bp=ini_guess(yci,3);
avA_a=ini_guess(yci,4);
avB_a=ini_guess(yci,5);
avB1m_a=ini_guess(yci,6);
T_onset_a=ini_guess(yci,7);
bpfr=ini_guess(yci,8);     %2.3.2. get the bp fraction from the file

% Ratio of areas between alpha/betaprime
abp_f =(1-bpfr)/bpfr*enth_a/enth_bp;

% 2.3.6.3. create a double that contains the data in one sheet for upcoming fitting
tdp=length(avhf);
avdlb=zeros(tdp,6);
avdlb(:,1)=avtimes;
avdlb(:,2)=avtemps;
avdlb(:,3)=avhf;

% 2.3.6.4. Save the culled data in text files
%     fnm=strcat('C:\DATA\A_Students\Zhang_Xinyue\Onset_T\D7txt\D_7_',snm,'.txt');
%     sf=avdlb(:,1:3);
%     save(fnm,'sf','-ascii','-tabs');

%%    % 2.3.7. fitting! for getting a reasonable starting value for Cp
% 2.3.7.1. Fit heat capacity to linear or quadratic function

modelfun = @(b,x)b(1) + b(2)*x(:,1);% + b(3)*x(:,1).^2;
% 2.3.7.1.1 cp of liquid coefficient fitting
ncoeffl=2;
coef0l =[l_L_0,l_L_1];%,l_L_2];

% Dividing  lhf by cr makes into cp_l signal
% Add 273.15 to make it in KELVIN and do the fit
mdll = fitnlm(ltemps+273.15,lhf/crs,modelfun,coef0l);
bl=[mdll.Coefficients{1:ncoeffl,1};0];

% 2.3.7.1.2 cp of solid coefficient fitting
ncoeffs=2;
if CR>CR_a
```

```
    coef0s=[a_L_0lin,a_L_1lin];%,a_L_2];
else
    coef0s=[bp_L_0lin,bp_L_1lin];%,bp_L_2];
end

% Dividing  lhf by cr makes into cp_s signal
% Add 273.15 to make it in KELVIN and do the fit
mdls = fitnlm(stemps+273.15,shf/crs,modelfun,coef0s);
bs=[mdls.Coefficients{1:ncoeffs,1};0];

% 2.3.7.1.3 Adjusting the fits to the ratio of cp
bbp(1,1)=bs(1)/(bpfr-bpfr*r_o+r_o);
bbp(2,1)=bs(2)/(bpfr-bpfr*r_1+r_1);
bbp(3,1)=0;
ba(1,1)=bbp(1)*r_o;
ba(2,1)=bbp(2)*r_1;
ba(3,1)=0;

% 2.3.7.1.4 place the coefficients in their cells
ftcpl(k,1)={bl};
ftcps(k,1)={[bs;bbp;ba]};



%% 2.3.8.  Fitting setup
% Calculate calhf with the guesses
% Here find total area, AT, by subtracting the baseline from the original data
hf_baseline=guess_baseline();
%%%%%%%%%%%%%%%%%%%%%%
for ft_i=1:3 % small 'for' to refine baseline iteratively (Section 6.3.)
    % 2.3.8.1. Baseline
    if ft_i == 1  %this is first pass, use the guess baseline
        gb = guess_baseline();
        %   if it is a later pass, use hf_baseline from the previous fit
    else  % use the baseline from fit
        gb = hf_baseline;
    end
    % 2.3.8.2. Subtract the cp baseline from the data
    avhf_s = avhf - gb;

% 2.3.8.3. Numerical estimate of the total area after subtracting baseline
% The first iteration uses the guessed baseline
% The next two use the baseline obtained from the fractions
% of liquid and the polymorphic solids
    AT = trapz(avtimes*60,avhf_s);
    % Area fraction provides the amplitude of each polymorph
    % from bpfr
    Ampl_bp = (1/(1+abp_f))*AT;
    Ampl_a = Ampl_bp*abp_f;

    % 2.3.8.4. Prepare the parameters for to compute the curve calhf
    if CR>CR_a
        parav = zeros(8,1);% Abp Will now come from AT and will NOT be fitted

        parav(1)=avA_bp;
        parav(2)=avB_bp;
        parav(3)=avB1m_bp;
        parav(4)=avA_a;
        parav(5)=avB_a;
        parav(6)=avB1m_a;
        parav(7)=T_onset_a;
```

```
        parav(8)=bpfr;
    else
        parav = zeros(4,1);
        parav(1)=Ampl_bp;
        parav(2)=avA_bp;
        parav(3)=avB_bp;
        parav(4)=avB1m_bp;
        % parav(4)=T_onset_bp;
        % parav(5:7)=bs(1:3);

    end
    %sapo=0;
    % 2.3.8.5. Generate the curve with the parameters from the guess
    [calhf,~,~,hf_baseline]=hff(parav);

    avdlb(:,4)=calhf;

    % 2.3.8.6. Plot
    %     figure(k); %
    %     plot(avtemps,avhf,'+r',avtemps,calhf,'--b');
    %     title(cell2mat(sheet_name(k)));
    %     fignm=strcat(dirfigs,cell2mat(sheet_name(k)),'.png');
    %     hold on;

  % 2.3.8.7. Prepare the figure, and plot the data and the curve from guess
    if ft_i == 1
        figure(k);
        plot(avtimes,avhf,'.g',avtimes,calhf,'--b','LineWidth',1);
        title(cell2mat(sheet_name(k)));
%           fignm=strcat(dirfigs,cell2mat(sheet_name(k)),'.png');
        hold on;
        xlabel('Undercooled Time T_m > T (min)');
        ylabel('Heat Flow (W/g)');
        xtickformat('%.1f');
        ylim([0 0.48*CR]);
        ytickformat('%.1f');
    end


    %% 2.3.9. FITTING  AVRAMI_EXTENDED
    % 2.3.9.1. LOCATION OF THE MAXIMA
    Tmaxk=cell2mat(Maxv(k,DSCset));
    Nummax=size(Tmaxk,1);
    % --- Index location of Max idx_mx
    idx_mx=sum(Tmaxk(1)<avtemps);
    % First maximum
    Tmax_c(1)=avtemps_c(idx_mx);
    % If they exist, minimum and second max
    if Nummax==3
        idx_mx=sum(Tmaxk(2)<avtemps);
        Tmax_c(2)=avtemps_c(idx_mx);
        idx_mx=sum(Tmaxk(3)<avtemps);
        Tmax_c(3)=avtemps_c(idx_mx);
    end

    % How to use lsqnonlin/fmincon
    % [coef,resnorm,residual,exitflag,output,lambda,jacobian] = lsqnonlin(fun,x0,lb,ub,options)
    %  Example of difference:  fun = @(x)x(1)*exp(-t).*exp(-exp(-(t-x(2)))) - y;

    % 2.3.9.2. Initial estimates of parameters and lower/upper
    % boundaries
```

```
    % 2.3.9.2.1. --- BETAPRIME ---

    b0av_bp=[avA_bp,avB_bp,avB1m_bp];

    % 2.3.9.2.2. --- ALPHA ---
    if CR>CR_a
       % include betaprime and alpha polymorph
       b0av_a=[avA_a,avB_a,avB1m_a,T_onset_a,bpfr];
       guess0av=[b0av_bp,b0av_a];
    else
       % if only betaprime
       guess0av=b0av_bp;
    end

    % 2.3.9.2.3. --- LOWER & UPPER BOUNDARIES ---

    lb=guess0av*0.80;
    ub=guess0av*1.20;
    % the cm term should not be less than one
    if lb(3)<1.05
       lb(3)=1.05;
    end
    if CR>CR_a
       if lb(6)<1.05
          lb(6)=1.05;
       end
    end

    % 2.3.9.2.3. Setup and call of the fmincon function

    % Definition of function handle as a difference between calculated hf
    % and experimental avhf - ERROR COMPUTATION - in Function "fune"
    % /*Call the ( fmincon -least squares non linear fitting ) function
    % fmincon(@ergn,sedi,A,b,[],[],lb,ub);

    % **** Linear Constraints
    A=zeros(1,8);
    b=zeros(1,1);
    % % A1*x1 + A2*x2 <= b
    A(1,7)=1; % linear constraints, so that T_alpha < T_bp
    % Linear constraint to keep
    b(1,1)=T_onset_bp-0.8;       % A1*x1 + A2*x2 <= b : 1*d_m (-1)*d_23 <= 0

    % **** Non-Linear Constraints are computed in function Nonlcon

    %       Array and variable debg for debugging
%       debgarr=zeros(8,6);

%       for numder=-1:1
%          for pn=1:8
%             debg=guess0av;
%             debg(pn)=coef0av(pn)*(1+0.01*numder);
%             cex=fune(bp);
%             testarray(pn,2+numder)=cex;
%          end
%       end
%
% ******************      MAIN CALL TO THE FMINCON FUNCTION ************
    [coefav,fval,exitflag,output,lambda,grad,hessian]= fmincon(@fune,guess0av,A,b,[],[],lb,ub,@Nonlcon);
```

```
    % 2.3.9.2.4. Assign the coefficients to the cell for this data set
    ftcoeff(k,1:7)={coefav,fval,exitflag,output,lambda,grad,hessian};
end  % of small for (to adjust the baseline)

% 2.3.9.3. check gpdfb,gpdfa in a reasonable shape
T_onset_af=coefav(7);
t_os_bp=avtimes(1);
t_os_a=t_os_bp+((T_onset_bp-T_onset_af)/CR);

%    deltaTmax_bp=56; % From 36 to -20
avB1_bp = (avB1m_bp-1)/(avB1m_bp*deltaTmax_bp);
[acdfb,~] = Avrt(CR*(avtimes-t_os_bp),avA_bp,avB_bp,avB1_bp);

%    deltaTmax_a=36; % From 16 to -20
avB1_a = (avB1m_a-1)/(avB1m_a*deltaTmax_a);
[acdfa,~] = Avrt(CR*(avtimes-t_os_a),avA_a,avB_a,avB1_a);

% 2.3.9.4. Crystallization distribution function pdf


% 2.3.9.5. Plot the hf on the same graph
%     figure(k);
%     plot(avtemps,hfcal,'-k','LineWidth',2);
%     hold off;

% Cacluate the Avrami extended function with the coefficients found
[hfcal,apdfb,apdfa,hf_baseline]=hff(coefav);
apdfbp_h=apdfb*Ampl_bp*crs+hf_baseline;
apdfa_h=apdfa*Ampl_a*crs+hf_baseline;
figure(k);
plot(avtimes,hfcal,'-k','LineWidth',2);
hold on;
plot(avtimes,apdfbp_h,'--m');
plot(avtimes,apdfa_h,'--k');
plot(avtimes,hf_baseline,':b');
hold off;

% 2.3.9.6. Calculate the hf estimates with the parameters fromt the fit

avdlb(:,4)=hfcal;              % calculated heat flow
avdlb(:,5)=hfcal-avdlb(:,3);   % residuals
avdlb(:,6)=hf_baseline;        % calculated baseline

% assemble all the doubles from each sheet in to a cell array
Esthf(k,1)={avdlb};
Onseta(k,1)=coefav(7);


% 2.3.9.7. Report the betaprime mass fraction and save it in a cell
if CR>CR_a
    bp_frac=coefav(8);
else
    bp_frac=1.0;
end
ftcoeff(k,8)={bp_frac};
ftcoeff(k,11)={T_onset_bp};

% 2.3.9.8. Estimate the confidence intervals of the parameters and save it to cell 9
ftcoeff{k,7}=real(ftcoeff{k,7}); % Takes only real part of Hessian/Jacobian
% stderrest = sqrt(diag(inv(hessian)));
% Nonlinear regression parameter confidence intervals
```

```
%     ci =nlparci((ftcoeff{k,1}),(ftcoeff{k,3}),'jacobian',(ftcoeff{k,7})); #
%     we dont have residual any more
%     ftcoeff(k,9)={ci'};

    % ^o.o^ Add here the estimate of the prediction confidence intervals nlpredci
    % This gives us the upper a lower curves of the estimates
    % can be saved to another cell structure since it has 5 columns
    % [Ypred,delta] = nlpredci(modelfun,X,coef,R,'Jacobian',J)

end %of 'for'

%% 2.4. Save values

% To save the outcome to excel file
% Get coefficients from structure ftcoeff
ftcoefft=cell2table(ftcoeff);
% ftcplt=cell2table(ftcpl);
% ftcpst=cell2table(ftcps);

% Make cofficient file name
coef_filnm = strcat('L_',setstr,'_Q100_coeff.xlsx');
% Save coefficients to Excel file
writetable(ftcoefft(:,1),coef_filnm);
%  writetable(ftcplt(:,1),'LLL5mvn2ftcpl.xlsx')
%  writetable(ftcpst(:,1),'LLL5mvn2ftcps.xlsx')
%  for k=1:17
%  writematrix(Esthf{k,1},'LLL5mvn2Esthf.xlsx','Sheet',k)
%  end
% ---------- END OF MAIN CODE----------

%% ======================================================================= %%
%                        NESTED FUNCTIONS
%% ======================================================================= %%

%% NF1. Function to estimate the hf in the av region. Operates as vector.
% ^o.o^ Modify the function, depending on the # of parameters
% 1. When alpha and betaprime are present, CR>CR_a
%  we will pass both sets of parameters
% 2. When only betaprime is present we will pass its parameters

    function [calhf,apdfb,apdfa,hf_baseline]=hff(parav)
    % 1. Get the parameters from parav
        if (CR>CR_a)
            % both betaprime and alpha present
            % Reorganized to put alpha parameters at the end

            avA_bp=parav(1);
            avB_bp=parav(2);
            avB1m_bp=parav(3);


            avA_a=parav(4);
            avB_a=parav(5);
            avB1m_a=parav(6);
            T_onset_af=parav(7);
            bpfr=parav(8);
            abp_f =(1-bpfr)/bpfr*enth_a/enth_bp;
            Ampl_bp = (1/(1+(1-bpfr)/bpfr*enth_a/enth_bp))*AT;
            Ampl_a=Ampl_bp*abp_f; %<-- fitted

        else
```

```
    % only betaprime present

    avA_bp=parav(1);
    avB_bp=parav(2);
    avB1m_bp=parav(3);

    % Others are set to zero, though they are not used
    Ampl_a=0;
    avA_a=0;
    avB_a=0;
    avB1m_a=1;
    T_onset_af=0;

end

% 2. Calculate heat capacities

% 2.1. Liquid from preliminary fit
cpl=bl(1)+bl(2)*(avtemps_c+273.15)+bl(3)*(avtemps_c+273.15).^2;
% Alpha and betaprime could have been calcualted separately
cpa=ba(1)+ba(2)*(avtemps_c+273.15)+ba(3)*(avtemps_c+273.15).^2;
cpbp=bbp(1)+bbp(2)*(avtemps_c+273.15)+bbp(3)*(avtemps_c+273.15).^2;

% ^o.o^ Avrami prob dens /cumulative function time:
% column number of Temp onset to get a correspond time onset

t_os_bp=avtimes(1);
t_os_a=t_os_bp+((T_onset_bp-T_onset_af)/CR);

% Compute the Avrami function estimate of the crystallization
% the function has an area of 1, i.e. has not yet been multiplied
% by the amplitude parameter

% **** Betaprime ****

avB1_bp = (avB1m_bp-1)/(avB1m_bp*deltaTmax_bp);
[acdfb,apdfb] = Avrt(CR*(avtimes-t_os_bp),avA_bp,avB_bp,avB1_bp);



if CR>CR_a
    % **** Alpha ****

    avB1_a = (avB1m_a-1)/(avB1m_a*deltaTmax_a);
    [acdfa,apdfa] = Avrt(CR*(avtimes-t_os_a),avA_a,avB_a,avB1_a);


    % Alpha & betaprime
    % Combine the two functions in the proportion of their amplitudes,
    % Which correspond to their areas
    % cumulative fraction in total
    crfrtot=(acdfa*Ampl_a+acdfb*Ampl_bp)/(Ampl_a+Ampl_bp);

    % Avoid dividing by zero when both gcdf a&b are zero

    zero_zone=(crfrtot==0); % Vector of 0s and 1s
    nz=sum(zero_zone,1); % sum gives us the # of points before onset
    % cumulative fraction for a
    crfra(1:nz,1)=0; % fill the vector with zeroes before onset
    % compute the value of the avrami contributions for the rest of the points
    crfra(nz+1:dng+1,1) = (acdfa(nz+1:dng+1,1)*Ampl_a)./...
```

```
            (acdfa(nz+1:dng+1,1)*Ampl_a+acdfb(nz+1:dng+1,1)*Ampl_bp);

        % Calculate the total heat flow adding the liquid and solid lines to the

        % Extended Avrami functions
        hf_cryst =(Ampl_a*apdfa + Ampl_bp*apdfb)*crs;
        hf_baseline = ((1-crfrtot).*cpl + crfrtot.*crfra.*cpa+(1-crfra).*crfrtot.*cpbp)*crs;
        calhf=hf_cryst + hf_baseline;
        %calhf=(Ampl_a*gpdfa + Ampl_bp*gpdfb + (1-crfrtot).*cpl + crfrtot.*crfra.*cpa+(1-crfra).*crfrtot.*cpbp)*crs;
    else
        % Only betaprime
        calhf=( Ampl_bp*apdfb + (1-acdfb).*cpl + acdfb.*cpbp)*crs;
    end
%         sapo=0; % Debugging variable
  end % Of the hff function
%% NF2. Avrami extended function Avrt
  function [avc,avd] = Avrt(delta_T,av_A,av_B,av_B1)
    % Avrami cumulative function  0 to 1
    % Find values that are negative or zero, i.e. before T_onset
    % make them all zero
    % delta_T is the vector of differences between the onset
    % temperature and the vector of temperatures Tonset-T

    % 1.locate the delta_T values that are positive,
    % i.e. after the onset temperature ...

    dTpos= delta_T>0;
    % ... and make zero the values for delta_T<0
    delta_T=delta_T.*dTpos;

    %2. Compute the ** cumulative ** Avrami function, taking only

    % the real parts in case there are imaginary results
    avc=real(1-exp(-(delta_T./(av_B-av_B1.*delta_T)).^av_A));

    % locate infinity values and replace them with 1
    avc_inf=(avc==inf)|(avc==-inf);
    inf_index = find(avc_inf);
    if size(inf_index,1)>0
        avc(inf_index)=1;
    end

    % 3. Compute Avrami ** derivative ** function

    % 3.1. Prepare the vectors
    dTnp= sum(dTpos,1); % Number of non-zero values
    % compute the index for the non-zero values and
    % create the vector with the temperature differences for that range
    if dng>dTnp
        avd(1:dng-dTnp,1)=0;
        dTp=delta_T(dng-dTnp+1:dng+1);
    else
        dTp=delta_T(1:dng+1);
    end

    % 3.2. *** Compute the Avrami crystallization rate function ***
    % DT^(a - 1)*a*b*exp(-(DT/(b-DT*c ))^a)/(b-DT*c )^(a + 1) from
    % Maple

    dTp_B=av_B-av_B1*dTp;       % Exponent denominator (b-DT*c )
    rTp=dTp./dTp_B;             % ratio (DT/(b-DT*c )
```

```
    f1 = (dTp_B).^(av_A+1);     % Denominator (b-DT*c )^(a + 1)
    f2 = exp(-(rTp.^av_A));     % Exponentioal term exp(-(DT/(b-DT*c ))^a)
    f3 = av_A*av_B*(dTp.^(av_A-1).* f2./f1); %DT^(a - 1)*a*b*f2/f1

    if dng>dTnp
       avd(dng-dTnp+1:dng+1,1)=real(f3(1:dTnp+1,1));
    else
       avd(1:dng+1,1)=real(f3(1:dng+1,1));
    end

    %3.3. Locate and remove any infinity values
    avd_inf=(avd==inf)|(avd==-inf);
    inf_index = find(avd_inf);
    if size(inf_index,1)>0
       avd(inf_index)=0;
    end

  end % of Avrami extended function

%% NF3. Baseline estimate function
  function [gb]=guess_baseline()
   % get the coefficients for the solid and liquid lines
   % that were fitted before
     b_s = bs(1);
     s_s = bs(2);
     b_l = bl(1);
     s_l = bl(2);
  % Intersecton of the cp baselines
     x_int = (b_s-b_l)/(s_l-s_s)-273.15;

     % cp coefficients are for temperature in K

     m1= avtemps_c>x_int; % At temperatures larger than xhalf
     m2 = avtemps_c<=x_int; % At temperatures lower than xhalf
     gbs=(b_s+s_s*(avtemps_c+273.15)).*m2;
     gbl=(b_l+s_l*(avtemps_c+273.15)).*m1;
     gb = (gbs+gbl)*crs;

  end

%% NF4. Error calculation including weighing: our objective function
  function [errsq]=fune(parms)
     % Function to calculate the sum of squared errors for fmincon
     % -- create vector of weights, if desired
     npsq=size(avhf,1);
     indxsq=floor(npsq*0.5);
     w1=ones(npsq,1);
     w1(1:indxsq)=w1(1:indxsq)*12;
     % -- calculate the error including the weights

     [calhfe,~,~,~]=hff(parms);
     errsq=sum(((calhfe- avhf).*w1*100).^2);
  end

%% NF5. Nonlinear constraints [cineq,ceq] function
  function [cineq,ceq]= Nonlcon(paravM)

     % ceq contains the values of the constraints = 0
     % cineq contains the values of the constraints < 0
```

```
% 1. Receive parameters from fmincon
avA_bpM=paravM(1);
avB_bpM=paravM(2);
avB1m_bpM=paravM(3);
avA_aM=paravM(4);
avB_aM=paravM(5);
avB1m_aM=paravM(6);
T_onset_afM=paravM(7);
bpfrM=paravM(8);

% 2. Convert the mass fraction to area fraction:
% 2.1. Ratio of area a / area bp abp_fM
abp_fM =(1-bpfrM)/bpfrM*enth_a/enth_bp;
% 2.2. Amplitude of each area to multiply by the function or deriv.
Ampl_bpM = (1/(1+abp_fM))*AT;
Ampl_aM=Ampl_bpM*abp_fM;
% 2.3. Computation of "B1" from "B1m"
avB1_bpM = (avB1m_bpM-1)/(avB1m_bpM*deltaTmax_bp);
avB1_aM = (avB1m_aM-1)/(avB1m_aM*deltaTmax_a);

% 3. compute the first derivativeas at the Tmax of the kth dataset

% at First (or only) Maximum the conditions are:
% A. The weighted sum of first derivatives must be equal to zero
% B. The weighted sum of second derivatives must be less than zero
   ceq=zeros(1,1);
   cineq=zeros(1,1);
   % 3.1. Derivatives for betaprime
   d1maxbp=y1_v(avA_bpM,avB_bpM,avB1_bpM,T_onset_bp- Tmax_c(1));
   d2maxbp=y2_v(avA_bpM,avB_bpM,avB1_bpM,T_onset_bp- Tmax_c(1));
   if T_onset_afM-Tmax_c(1)>0
      % 3.2. Derivatives for Alpha
      d1maxa=y1_v(avA_aM,avB_aM,avB1_aM, T_onset_afM-Tmax_c(1));
      d2maxa=y2_v(avA_aM,avB_aM,avB1_aM, T_onset_afM-Tmax_c(1));
      % 3.3. calculate the error:it should be zero at first max
      ceq(1)=(Ampl_bpM*d1maxbp+Ampl_aM*d1maxa)*crs;
      % 3.4. Should be NEGATIVE for 2nd derivative, i.e. [] <=0
      % 3.5. Return the nonlinear inequalities
      cineq(1)=(Ampl_bpM*d2maxbp+Ampl_aM*d2maxa)*crs;
   else
      ceq(1)=Ampl_bpM*crs*d1maxbp;
      cineq(1)=Ampl_bpM*crs*d2maxbp;
   end

if Nummax==3
   % 4. at minimum between maxima
   d1maxbp=y1_v(avA_bpM,avB_bpM,avB1_bpM,T_onset_bp - Tmax_c(2));
   d1maxa=y1_v(avA_aM,avB_aM,avB1_aM, T_onset_afM - Tmax_c(2));

   % calculate the error,since should be zero at min
   ceq(2)=(Ampl_bpM*d1maxbp+Ampl_aM*d1maxa)*crs;

   % The second derivative should be POSITIVE at the minimum
   d2maxbp=y2_v(avA_bpM,avB_bpM,avB1_bpM,T_onset_bp - Tmax_c(2));
   d2maxa=y2_v(avA_aM,avB_aM,avB1_aM, T_onset_afM- Tmax_c(2));
   cineq(2)=(-1)*(Ampl_bpM*d2maxbp+Ampl_aM*d2maxa)*crs;



   % 5. at 2nd maximum
   d1maxbp=y1_v(avA_bpM,avB_bpM,avB1_bpM,T_onset_bp- Tmax_c(3));
```

```
        d1maxa=y1_v(avA_aM,avB_aM,avB1_aM, T_onset_afM-Tmax_c(3));

        % calculate the error,since should be zero at second max
        ceq(3)=(Ampl_bpM*d1maxbp+Ampl_aM*d1maxa)*crs;

        % The second derivative should be NEGATIVE at the 2nd maximum
        d2maxbp=y2_v(avA_bpM,avB_bpM,avB1_bpM,T_onset_bp - Tmax_c(3));
        d2maxa=y2_v(avA_aM,avB_aM,avB1_aM, T_onset_afM- Tmax_c(3));
        cineq(3)=(Ampl_bpM*d2maxbp+Ampl_aM*d2maxa)*crs;


    end

  end
%% NF6. Calculation of the   first derivative   of the Avrext function
  function y1 = y1_v(a, b, c, DT)
    % FIRST derivative with respect to TEMPERATURE
    % DT is To-T
    y1 = (-a*b*(-DT/(DT*c - b))^a + 2*DT*c + a*b - b)*...
      exp(-(-DT/(DT*c - b))^a)*b*a*DT^(a - 2)/...
      ((-DT*c + b)^(a + 1)*(-DT*c + b));
  end% end of y1
%% NF7. Calculation of the   second derivative   of the Avrext function
  function y2 = y2_v(a, b, c, DT)
    % SECOND derivative with respect to TEMPERATURE
    % DT is To-T
    y2 = DT^(a - 3)*(((DT/(-DT*c + b))^a)^2*a^2*b^2 - 3*(b*(a - 1)+ ...
      2*DT*c)*a*b*(DT/(-DT*c + b))^a + b^2*(a^2 - 3*a + 2) + ...
      6*c*DT*(a - 1)*b + 6*DT^2*c^2)*a*exp(-(DT/(-DT*c + b))^a)*b/...
      ((-DT*c + b)^(a + 1)*(-DT*c + b)^2);
  end % end of y2
end % of the overall code
% =========================================================================
```

Appendix E: Plots of the fitted functions

The fitting result of the MATLAB code for data from LLL pan 1,2 and 3 under cooling rates from 2.5 C°/min to 24 C°/min. Each sample pan contains 54 runs. The plots including the heat flow, fitting, rate (Derivative) functions for α and β', initial guess line, as well as a fitted baseline against undercooled time.

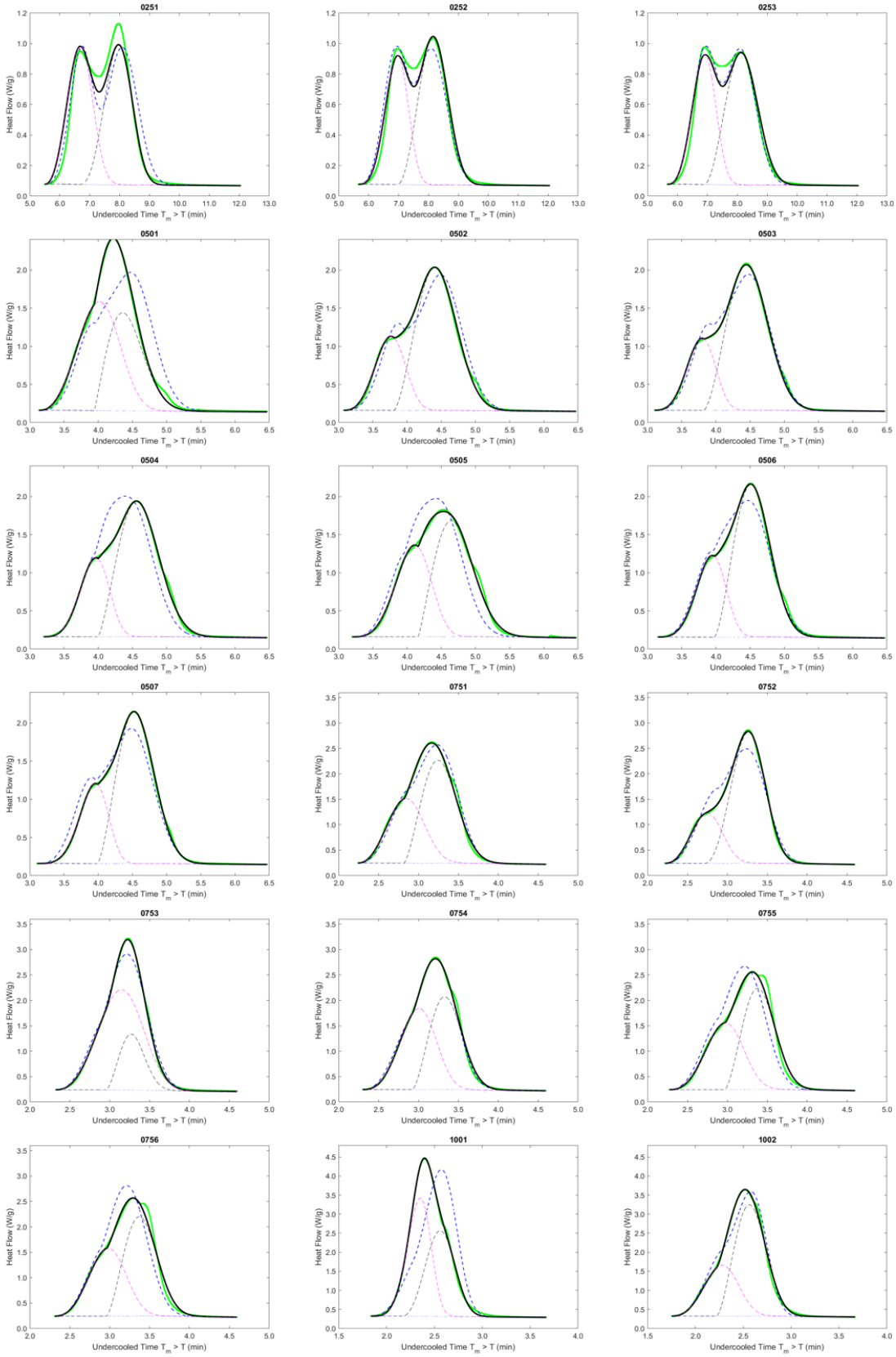
0251
0252
0253
0501
0502
0503
0504
0505
0506
0507
0751
0752
0753
0754
0755
0756
1001
1002
Heat Flow (W/g)
Undercooled Time T_m > T (min)

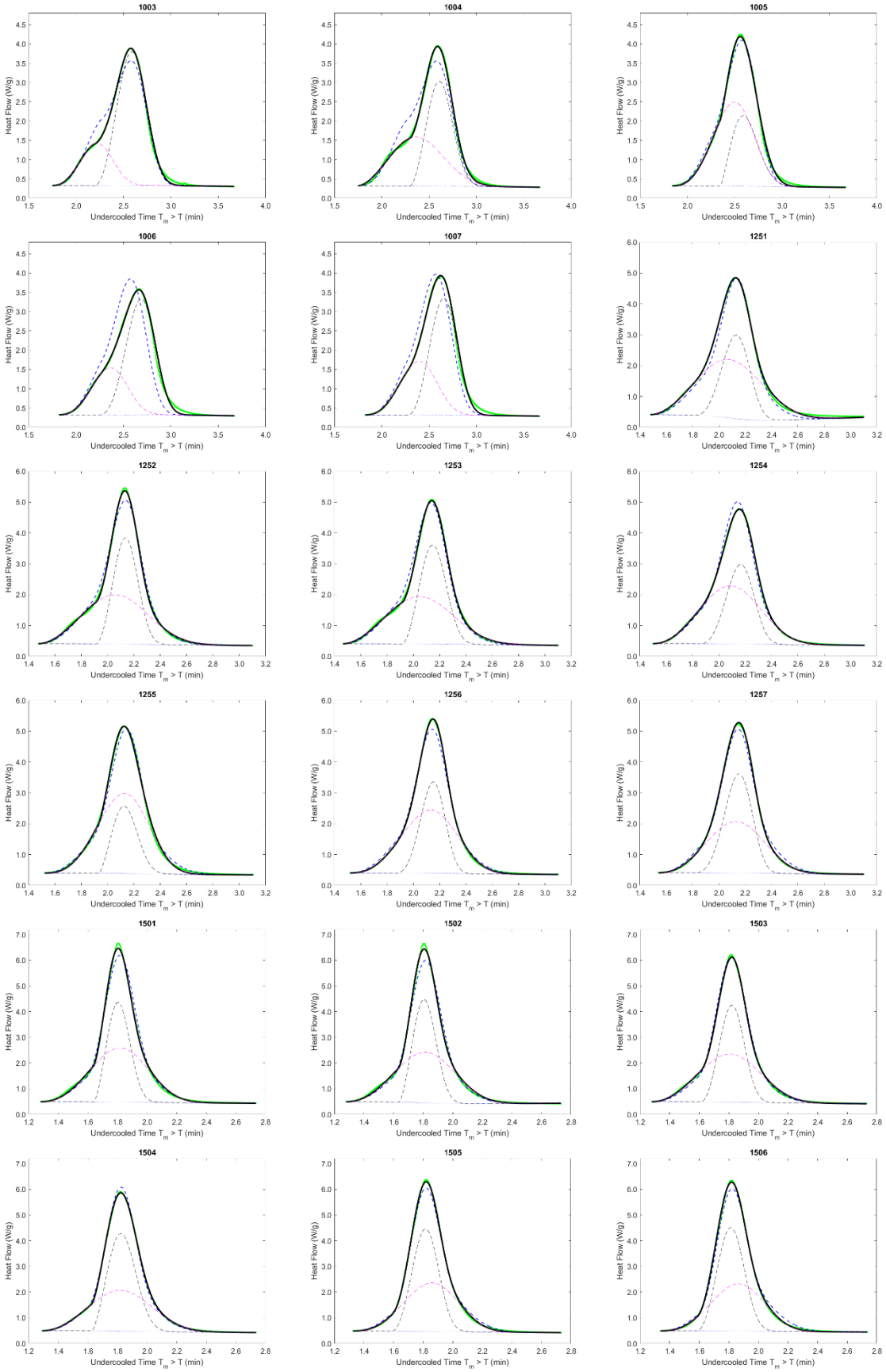
1003
1004
1005
1006
1007
1251
1252
1253
1254
1255
1256
1257
1501
1502
1503
1504
1505
1506
Heat Flow (W/g)
Undercooled Time T_m > T (min)

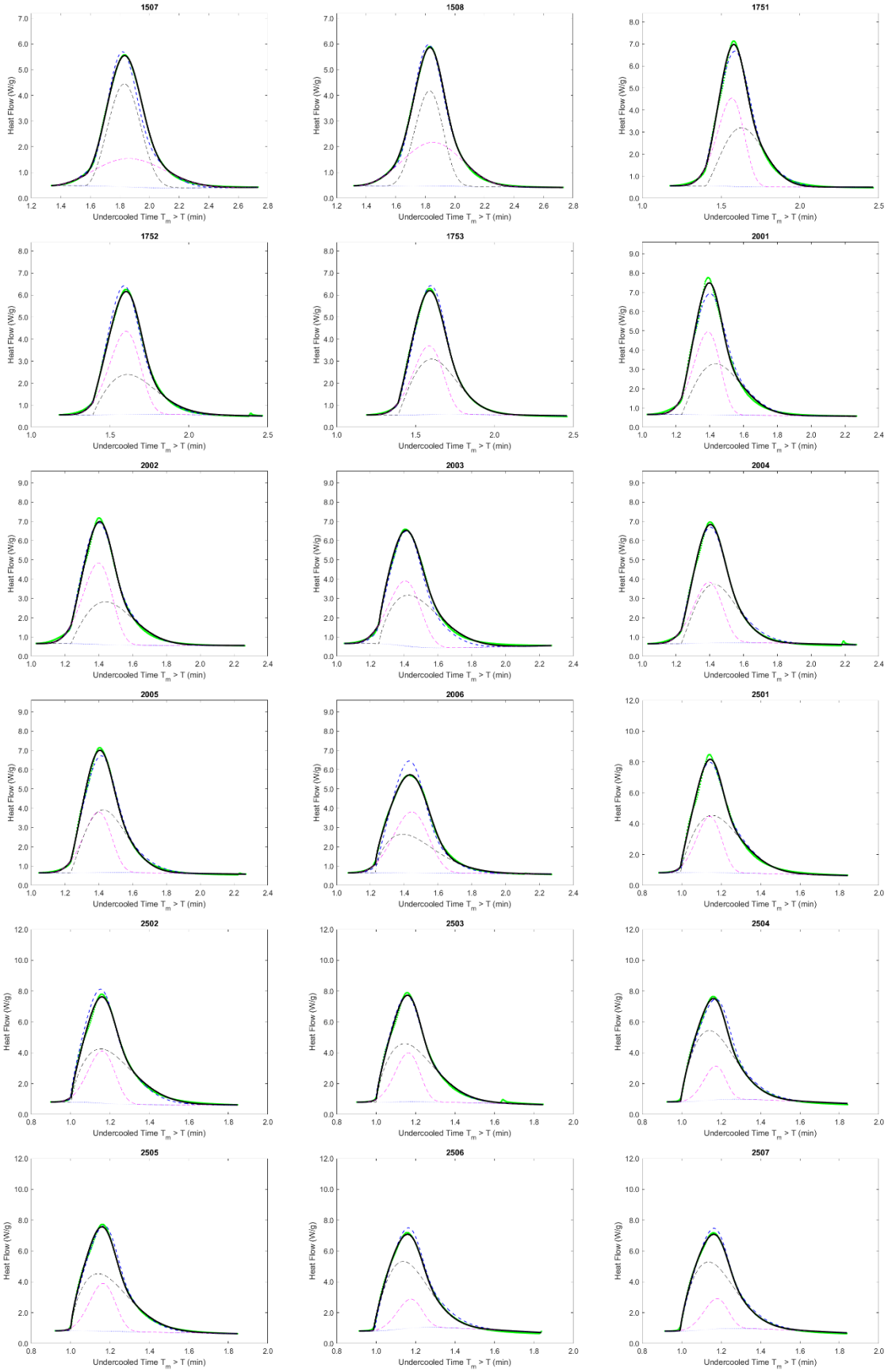
1507
1508
1751
1752
1753
2001
2002
2003
2004
2005
2006
2501
2502
2503
2504
2505
2506
2507
Heat Flow (W/g)
Undercooled Time T_m > T (min)

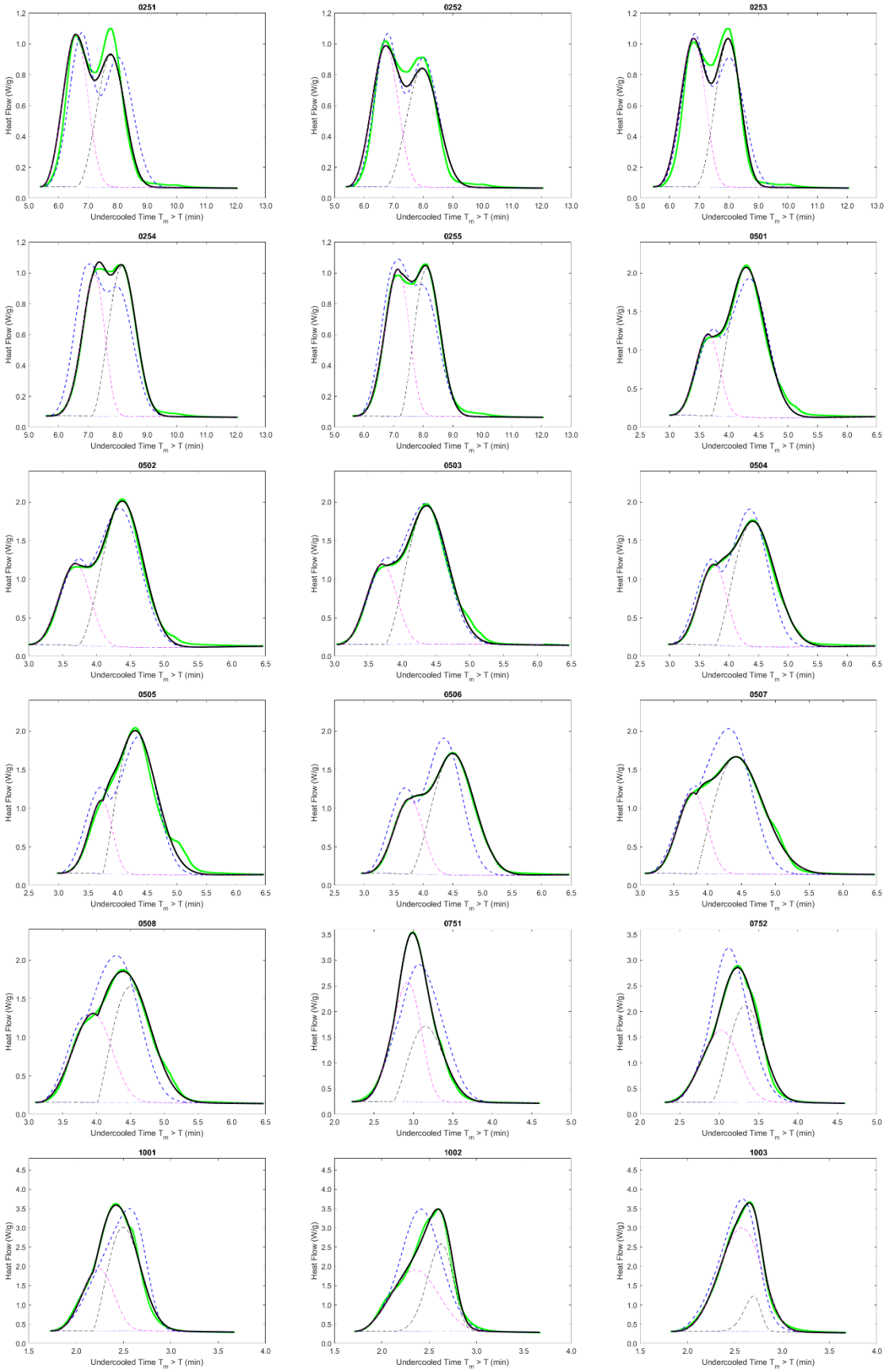
0251
0252
0253
0254
0255
0501
0502
0503
0504
0505
0506
0507
0508
0751
0752
1001
1002
1003
Heat Flow (W/g)
Undercooled Time T_m > T (min)

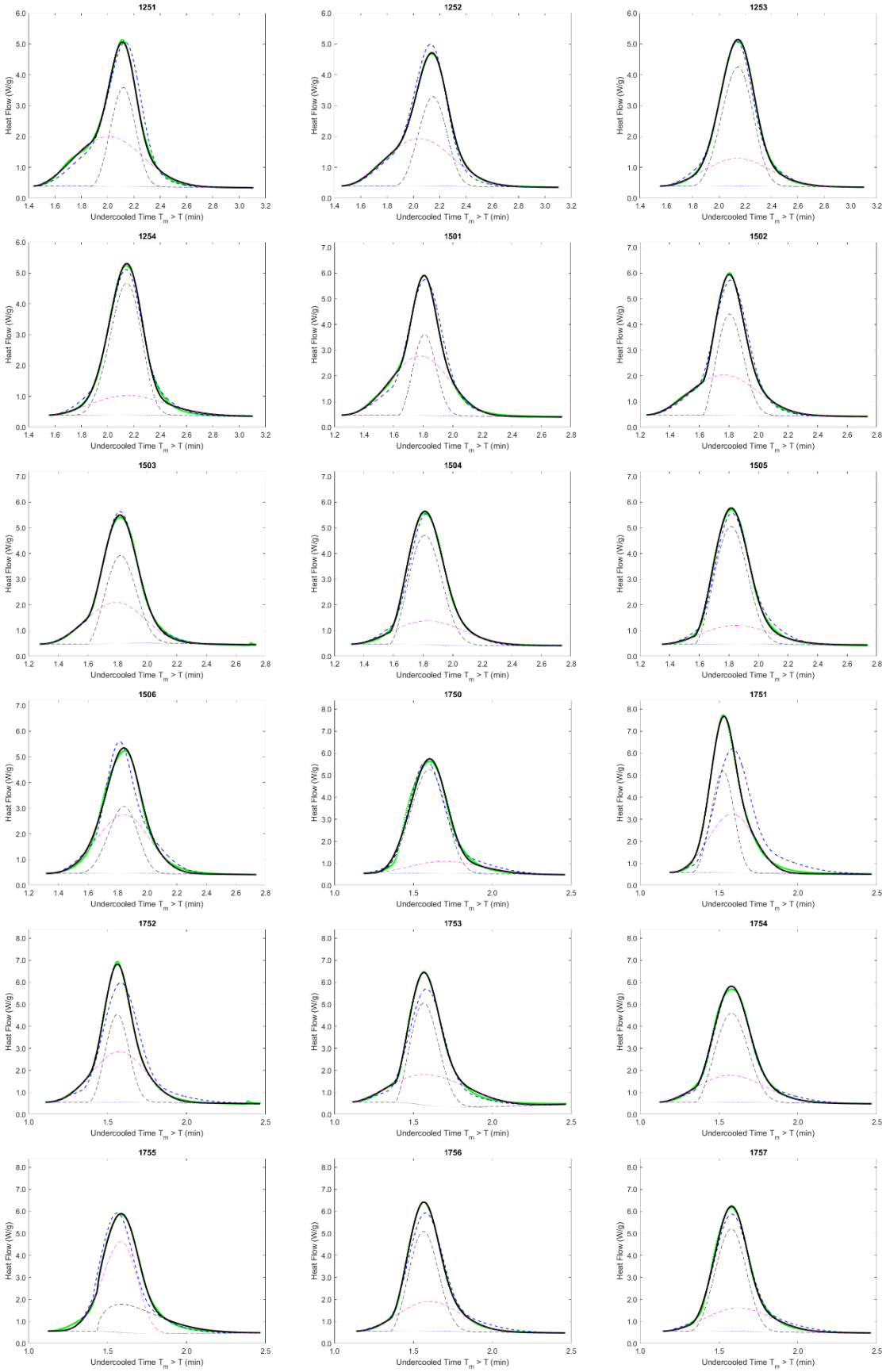
1251
1252
1253
1254
1501
1502
1503
1504
1505
1506
1750
1751
1752
1753
1754
1755
1756
1757
Heat Flow (W/g)
Undercooled Time T_m > T (min)

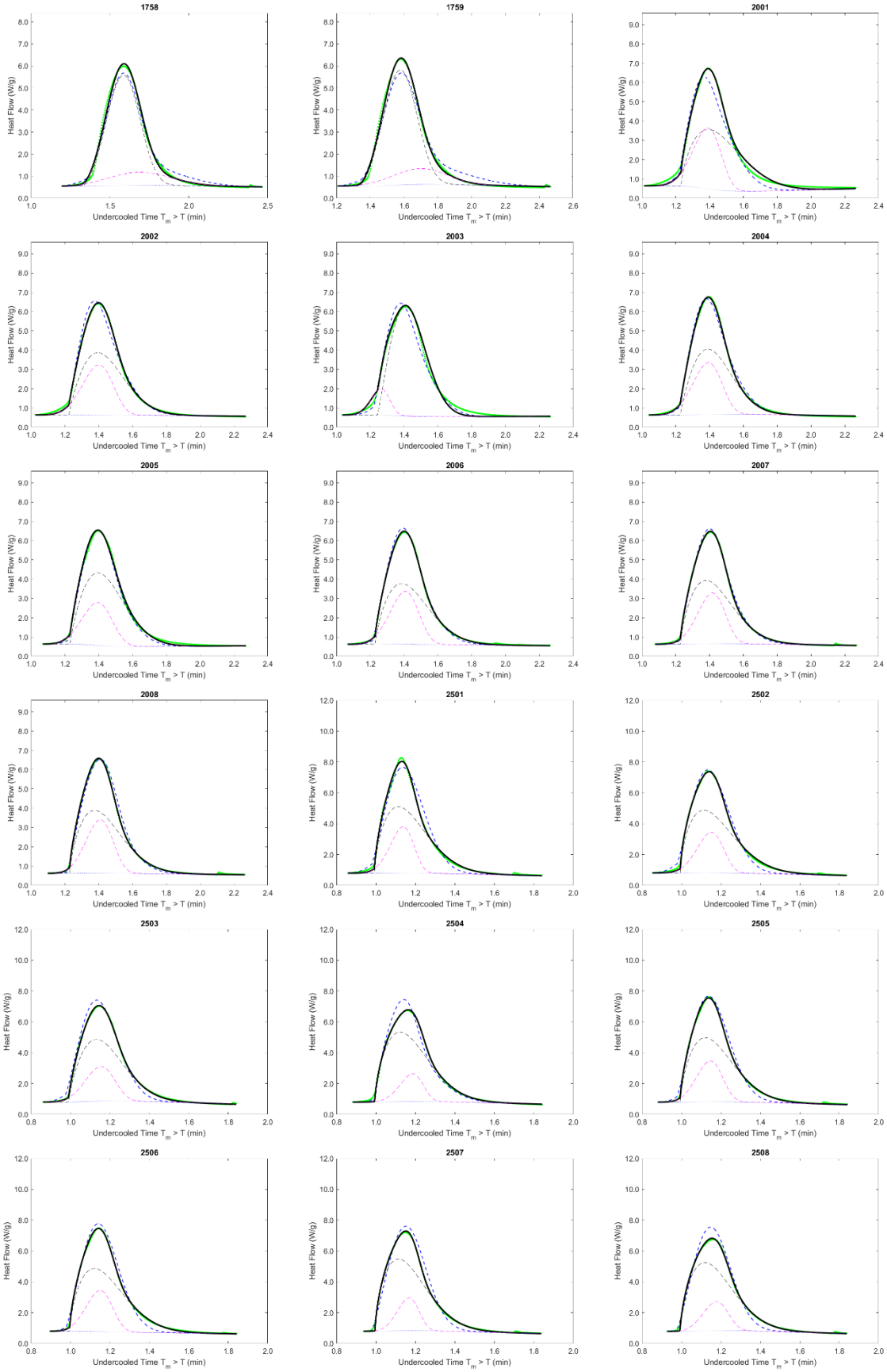
1758
1759
2001
2002
2003
2004
2005
2006
2007
2008
2501
2502
2503
2504
2505
2506
2507
2508
Heat Flow (W/g)
Undercooled Time T_m > T (min)

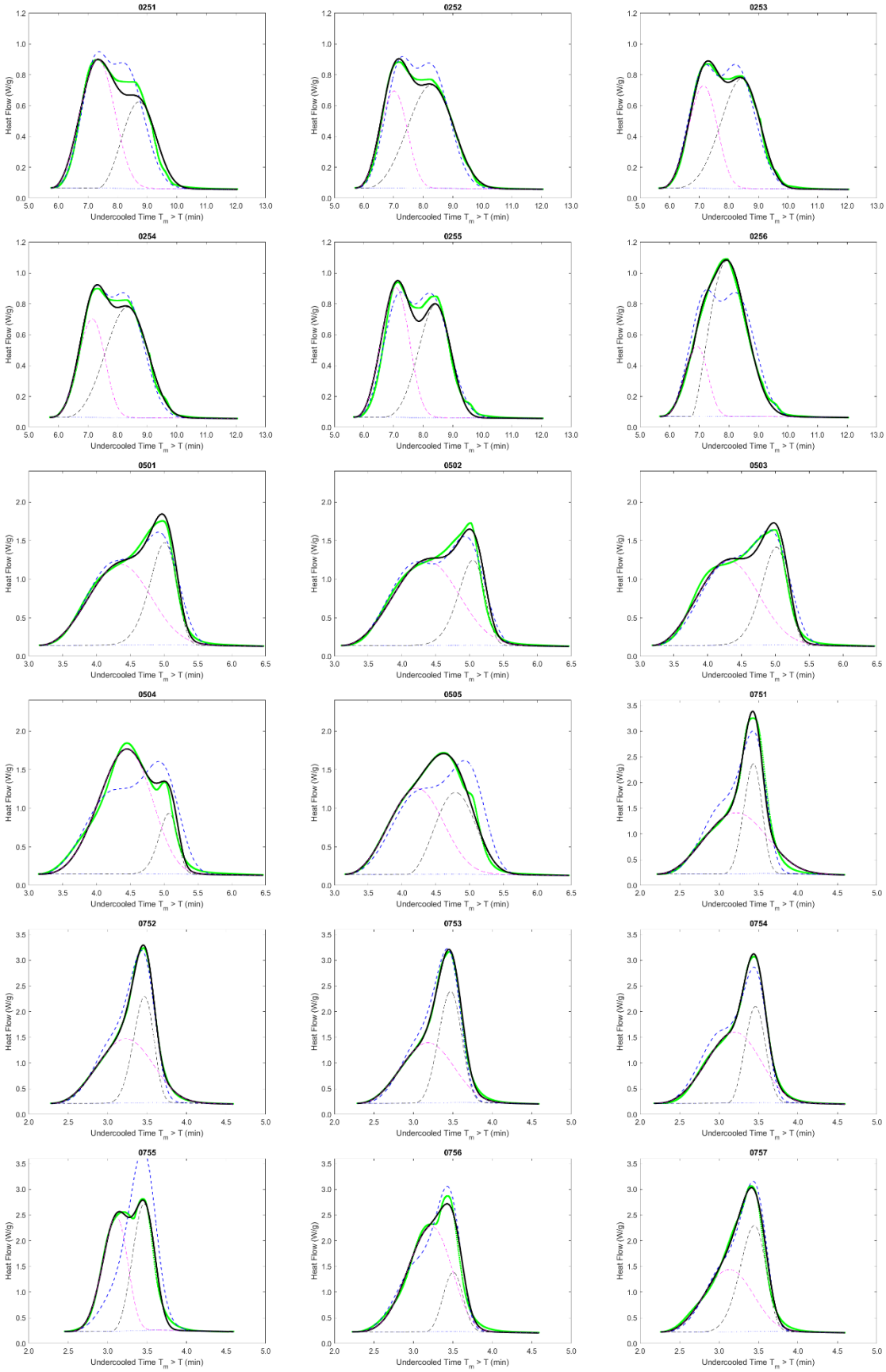
0251
0252
0253
0254
0255
0256
0501
0502
0503
0504
0505
0751
0752
0753
0754
0755
0756
0757
Heat Flow (W/g)
Undercooled Time T_m > T (min)

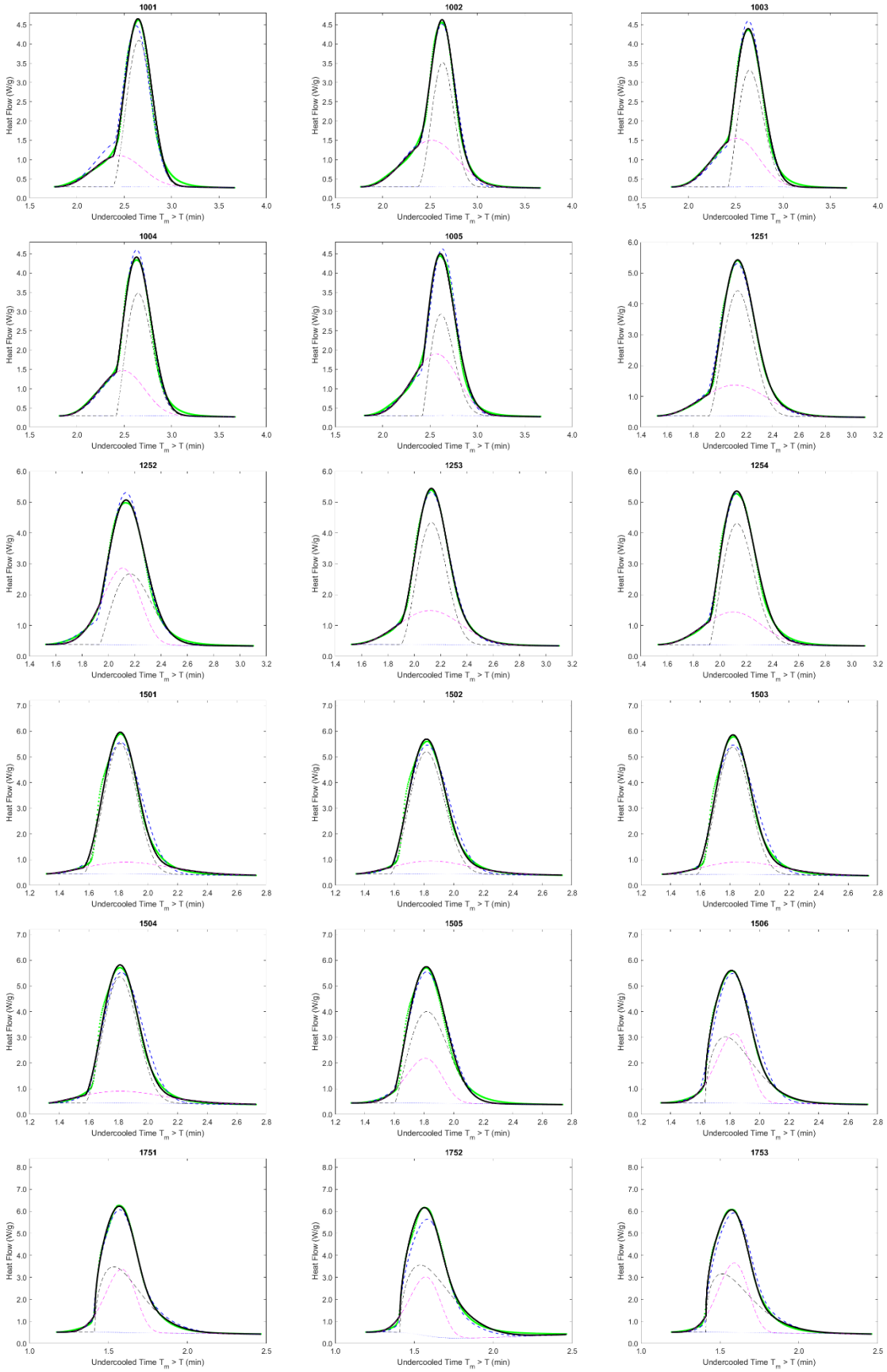
1001
1002
1003
1004
1005
1251
1252
1253
1254
1501
1502
1503
1504
1505
1506
1751
1752
1753
Heat Flow (W/g)
Undercooled Time T_m > T (min)

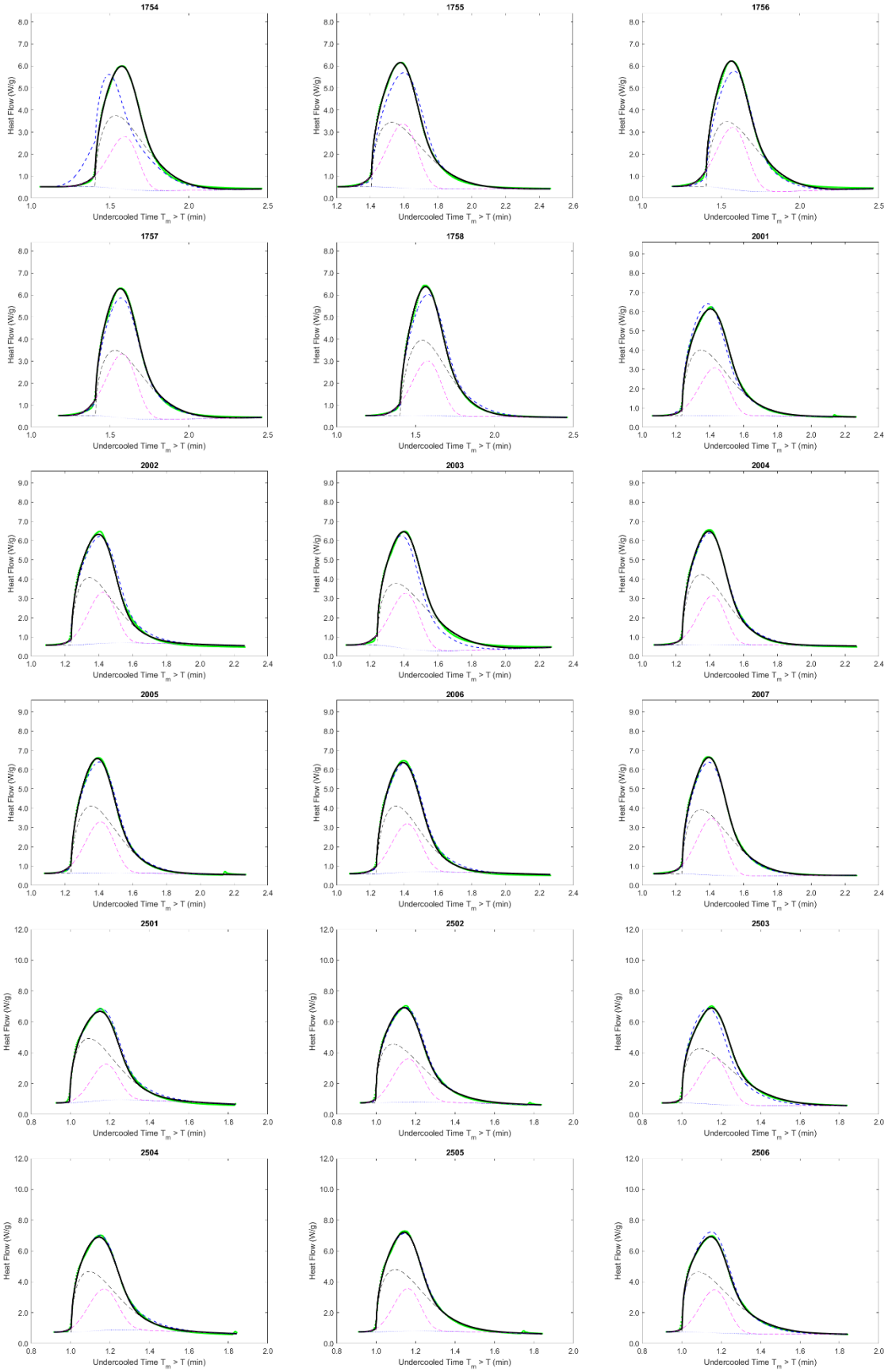
1754
1755
1756
1757
1758
2001
2002
2003
2004
2005
2006
2007
2501
2502
2503
2504
2505
2506
Heat Flow (W/g)
Undercooled Time T_m > T (min)

Appendix F: Plots of the Avrami model fitted parameters for the three pans

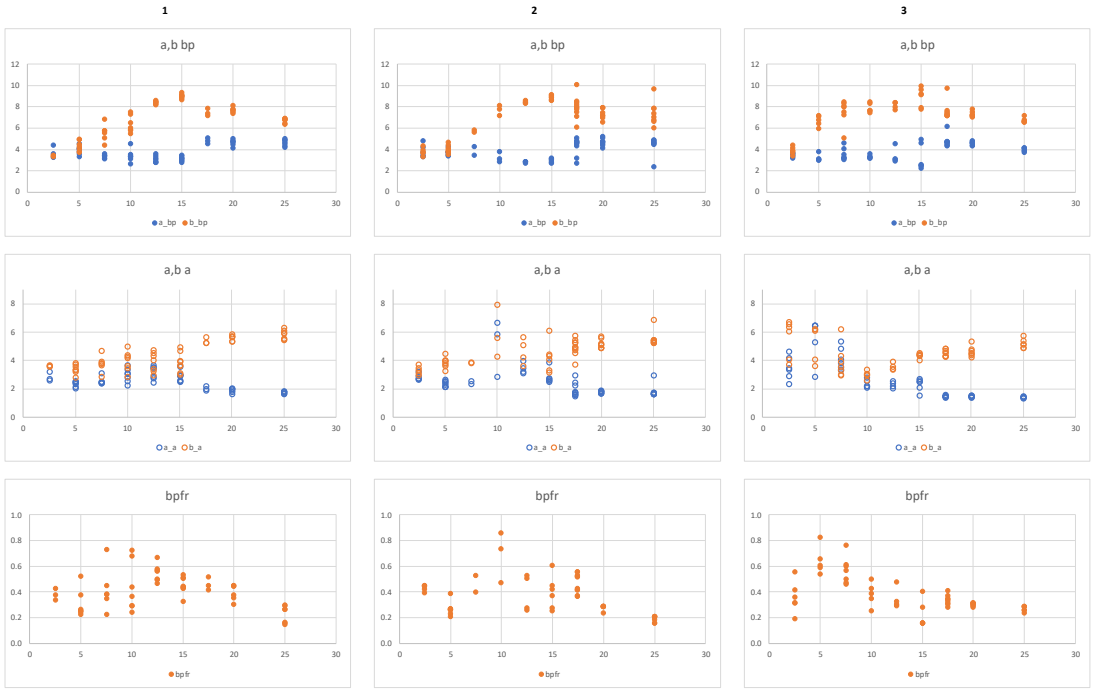

Appendix G: Derivation of modified Avrami model in Maple

Modified Avrami function (v07B)

1. Definition of the function

The cumulative Avrami (Weibull) function, extended by us has three characteristic terms: "a" is the exponent or growth dimension, in the ideal case 1, 2, or 3 for needle, disc, or sphere, plus 0 or 1 for instantaneous or for periodic nucleation. "b" is the characteristic crystallization time, which is the inverse of the maximum crystallization rate. The new term introduced, "c", is the linear decrease in characteristic time as a function of the undercooling. Thus, as the temperature becomes lower, the undercooling increases and the rate of crystallization increases. DTm is the temperature difference between the melting temperature and the current temperature. The time t starts at the onset of crystallization.

$$yct := (a, b, c, DT, t) \to 1 - e^{-\left(\left(\frac{t}{b - c \cdot DTm}\right)^a\right)}$$

$$yct := (a, b, c, DT, t) \mapsto 1 - e^{-\left(\frac{t}{b - c \cdot DTm}\right)^a}$$

For the isothermal case, the time changes, whereas the denominator of "r" stays constant. The derivative with respect to temperature is zero, and the derivative with respect to time is

$$ydt := (a, b, c, DT) \to \frac{d}{dt}(yct(a, b, c, DT, t))$$

$$ydt := (a, b, c, DT) \to \frac{\partial}{\partial t} yct(a, b, c, DT, t)$$

$$ydt(a, b, c, DT)$$

$$\frac{\left(\frac{t}{-c\,DTm + b}\right)^a a\, e^{-\left(\frac{t}{-c\,DTm + b}\right)^a}}{t}$$

For the case that we have a constant linear cooling rate **cr = dT/dt** during the ramp, the time is t = cr*DT. We introduce "DT" as the difference between the onset of crystallization temperature and the current temperature, DT = To-T. The values of b and c are different from above because they change with the cooling rate and the onset temperature. For purely fitting purposes this is not a problem. (If a set of values of b and c that are 'cooling rate independent' is desired, then the function above needs to be defined a bit differently).

$$yc := (a, b, c, DT) \to 1 - e^{-\left(\left(\frac{DT}{b - c \cdot DT}\right)^a\right)}$$

$$yc := (a, b, c, DT) \mapsto 1 - e^{-\left(\frac{DT}{b - c \cdot DT}\right)^a}$$

This version is convenient because we have only one variable, DT, which is the temperature difference from the onset. The derivative of the function with respect to the temperature below the onset is

$$yd := (a, b, c, DT) \to \frac{d}{dDT}(yc(a, b, c, DT))$$

$$yd := (a, b, c, DT) \to \frac{\partial}{\partial DT} yc(a, b, c, DT)$$

$yd(a, b, c, DT)$

$$\frac{\left(\frac{DT}{-c\,DT+b}\right)^{a} a \left(\frac{1}{-c\,DT+b}+\frac{DT\,c}{(-c\,DT+b)^{2}}\right)(-c\,DT+b)\,\mathrm{e}^{-\left(\frac{DT}{-c\,DT+b}\right)^{a}}}{DT}$$

factor

$$-\frac{\mathrm{e}^{-\left(-\frac{DT}{c\,DT-b}\right)^{a}} b\,a\left(-\frac{DT}{c\,DT-b}\right)^{a}}{DT\,(c\,DT-b)}$$

1. ***Definition of the derivatives of the pd function***

$r(b, c, DT) := \frac{DT}{b - c \cdot DT}$

$$r := (b, c, DT) \mapsto \frac{DT}{b - c \cdot DT}$$

$$y := (a, b, c, DT) \to \frac{(DT)^{a-1}\,a\,b\,\mathrm{e}^{-\left(\frac{DT}{b-c\,DT}\right)^{a}}}{(b - c\,DT)^{a+1}}$$

$$y := (a, b, c, DT) \mapsto \frac{DT^{a-1} \cdot a \cdot b \cdot \mathrm{e}^{-\left(\frac{DT}{b - c \cdot DT}\right)^{a}}}{(b - c \cdot DT)^{a+1}}$$

$y(a, b, c, DT)$

$$\frac{DT^{a-1}\,a\,b\,\mathrm{e}^{-\left(\frac{DT}{-c\,DT+b}\right)^{a}}}{(-c\,DT+b)^{a+1}}$$

To check this function, we plot it for two different sets of values

$z := x \to 0.7 \cdot y(3.1, 4.5, 0.15, x)$

$$z := x \mapsto 0.7 \cdot y(3.1, 4.5, 0.15, x)$$

→

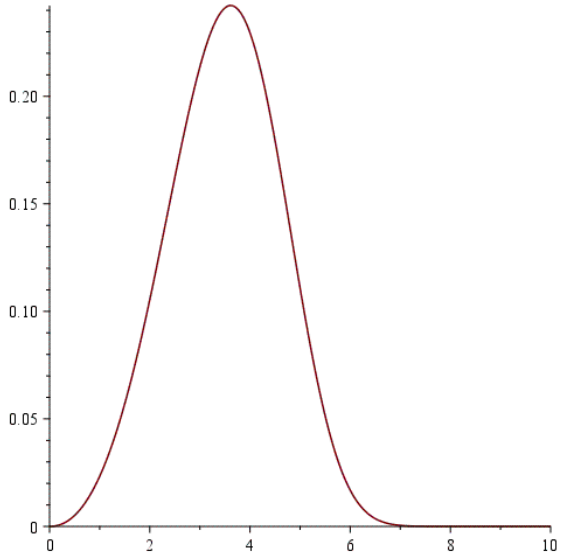

$y(3.1, 4.5, 0.15, 3.614985145) = 0.3460161601$

2. **First derivative**

$$y1 := (a, b, c, DT) \to \frac{\mathrm{d}}{\mathrm{d}\,DT}(y(a, b, c, DT))$$

$$y1 := (a, b, c, DT) \to \frac{\partial}{\partial DT} y(a, b, c, DT)$$

$y1(a, b, c, DT)$

$$\frac{DT^{a-1}(a-1)\,a\,b\,\mathrm{e}^{-\left(\frac{DT}{-c\,DT+b}\right)^{a}}}{DT\,(-c\,DT+b)^{a+1}} - \frac{1}{DT\,(-c\,DT+b)^{a+1}}\left(DT^{a-1}a^{2}b\left(\frac{DT}{-c\,DT+b}\right)^{a}\left(\frac{1}{-c\,DT+b} + \frac{DT\,c}{(-c\,DT+b)^{2}}\right)(-c\,DT+b)\,\mathrm{e}^{-\left(\frac{DT}{-c\,DT+b}\right)^{a}}\right) + \frac{DT^{a-1}\,a\,b\,\mathrm{e}^{-\left(\frac{DT}{-c\,DT+b}\right)^{a}}(a+1)\,c}{(-c\,DT+b)^{a+1}(-c\,DT+b)}$$

factor

$$-\frac{\left(-a\,b\left(-\frac{DT}{c\,DT-b}\right)^{a} + 2\,c\,DT + a\,b - b\right)\mathrm{e}^{-\left(-\frac{DT}{c\,DT-b}\right)^{a}} b\,a\,DT^{a-1}}{(-c\,DT+b)^{a+1}\,DT\,(c\,DT-b)}$$

$$y11 := (a, b, c, DT)$$

$$\rightarrow \frac{\left(-a\,b\left(-\frac{DT}{DT\,c-b}\right)^{a}+2\,DT\,c+a\,b-b\right)\mathrm{e}^{-\left(-\frac{DT}{DT\,c-b}\right)^{a}}\,b\,a\,DT^{a-2}}{(-DT\,c+b)^{a+1}\,(b-DT\,c)}$$

$$y11 := (a, b, c, DT)$$

$$\mapsto \frac{\left(-b\cdot a\cdot\left(-\frac{DT}{c\cdot DT-b}\right)^{a}+2\cdot c\cdot DT+b\cdot a-b\right)\cdot\mathrm{e}^{-\left(-\frac{DT}{c\cdot DT-b}\right)^{a}}\cdot b\cdot a\cdot DT^{a-2}}{(b-c\cdot DT)^{a+1}\cdot(b-c\cdot DT)}$$

$$z := x \rightarrow 0.7\cdot y11(3.1, 4.5, 0.15, x)$$

$$z := x \mapsto 0.7\cdot y11(3.1, 4.5, 0.15, x)$$

$\rightarrow$

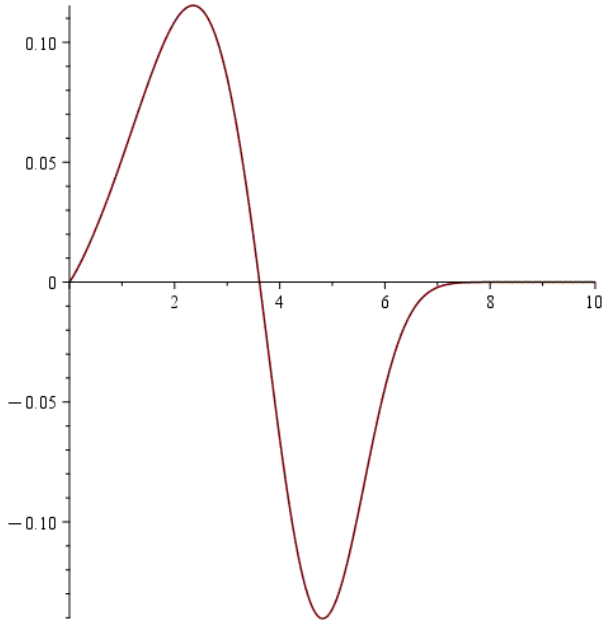

$$z(x) = 0$$

$$\frac{9.765\left(-13.95\left(-\frac{x}{0.15\,x-4.5}\right)^{3.1}+0.30\,x+9.45\right)\mathrm{e}^{-\left(-\frac{x}{0.15\,x-4.5}\right)^{3.1}}\,x^{1.1}}{(4.5-0.15\,x)^{5.1}} = 0$$

$\xrightarrow{\text{solve for x}}$

$$[[x = 0.], [x = 3.614985145], [x = -1.520524347 + 3.856479319\,\mathrm{I}], [x = -1.520524347 - 3.856479319\,\mathrm{I}]]$$

$$0., 3.614985145, -1.520524347 + 3.856479319\,\mathrm{I}, -1.520524347 - 3.856479319\,\mathrm{I}$$

3. Second Derivative (under development)

Most of our thermograms do not have two peaks and a valley. They have a 'hump' in one of the sides of the maximum. This induces inflection points, that can be identified numerically in the data.
In this case the second derivative can be used as the additional information to improve our knowledge about the parameters that we are fitting to the data.

$y2 := (a, b, c, DT) \to \frac{d}{dDT}(y11(a, b, c, DT))$

$$y2 := (a, b, c, DT) \to \frac{\partial}{\partial DT} y11(a, b, c, DT)$$

$y2(a, b, c, DT)$

$$\frac{1}{(-cDT+b)^{a+1}(-cDT+b)}\left(\left(\frac{1}{DT}\left(a^2 b\left(-\frac{DT}{cDT-b}\right)^a\left(-\frac{1}{cDT-b}+\frac{DTc}{(cDT-b)^2}\right)(cDT-b)\right)+2c\right)e^{-\left(-\frac{DT}{cDT-b}\right)^a} baDT^{a-2}\right)$$

$$+\frac{1}{DT(-cDT+b)^{a+1}(-cDT+b)}\left(\left(-ab\left(-\frac{DT}{cDT-b}\right)^a+2cDT+ab-b\right)\left(-\frac{DT}{cDT-b}\right)^a a^2\left(-\frac{1}{cDT-b}+\frac{DTc}{(cDT-b)^2}\right)(cDT-b)e^{-\left(-\frac{DT}{cDT-b}\right)^a} bDT^{a-2}\right)$$

$$+\frac{\left(-ab\left(-\frac{DT}{cDT-b}\right)^a+2cDT+ab-b\right)e^{-\left(-\frac{DT}{cDT-b}\right)^a} baDT^{a-2}(a-2)}{DT(-cDT+b)^{a+1}(-cDT+b)}$$

$$+\frac{1}{(-cDT+b)^{a+1}(-cDT+b)^2}\left(\left(-ab\left(-\frac{DT}{cDT-b}\right)^a+2cDT+ab-b\right)e^{-\left(-\frac{DT}{cDT-b}\right)^a} baDT^{a-2}(a+1)c\right)$$

$$+\frac{\left(-ab\left(-\frac{DT}{cDT-b}\right)^a+2cDT+ab-b\right)e^{-\left(-\frac{DT}{cDT-b}\right)^a} baDT^{a-2}c}{(-cDT+b)^{a+1}(-cDT+b)^2}$$

simplify

$$\frac{1}{(-c\,DT+b)^2\,DT\,(-c\,DT+b)^{a+1}}\left(e^{-\left(\frac{DT}{-c\,DT+b}\right)^a}\,b\,a\,DT^{a-2}\left(\left(\left(\frac{DT}{-c\,DT+b}\right)^a\right)^2 a^2\,b^2-3\,b\,((a-1)\,b+2\,c\,DT)\,a\left(\frac{DT}{-c\,DT+b}\right)^a+\left(a^2-3\,a+2\right)b^2+6\,c\,DT\,(a-1)\,b+6\,DT^2\,c^2\right)\right)$$

$$lix := (DT,a,b)\to DT^{a-3}\frac{\left(a^2-3\,a+2\right)a}{b^a}$$

$$lix := (DT,a,b)\mapsto \frac{DT^{a-3}\cdot\left(a^2-3\cdot a+2\right)\cdot a}{b^a}$$

This allows us to define the second derivative without going through Maple's derivative operator again, which was giving us an error.

$$y22(a,b,c,DT) := \frac{1}{(-DT\,c+b)^{a+1}\,(-DT\,c+b)^2}\left(DT^{a-3}\left(\left(\left(\frac{DT}{-DT\,c+b}\right)^a\right)^2 a^2\,b^2-3\,(b\,(a-1)+2\,DT\,c)\,a\,b\left(\frac{DT}{-DT\,c+b}\right)^a+b^2\left(a^2-3\,a+2\right)+6\,c\,DT\,(a-1)\,b+6\,DT^2\,c^2\right)a\,e^{-\left(\frac{DT}{-DT\,c+b}\right)^a}\,b\right)$$

$$y22 := (a,b,c,DT)\mapsto \frac{1}{(b-c\cdot DT)^{a+1}\cdot(b-c\cdot DT)^2}\left(DT^{a-3}\cdot\left(\left(\left(\frac{DT}{b-c\cdot DT}\right)^a\right)^2\cdot a^2\cdot b^2-(3\cdot b\cdot(a-1)+6\cdot c\cdot DT)\cdot a\cdot b\cdot\left(\frac{DT}{b-c\cdot DT}\right)^a+b^2\cdot\left(a^2-3\cdot a+2\right)+6\cdot c\cdot DT\cdot(a-1)\cdot b+6\cdot DT^2\cdot c^2\right)\cdot a\cdot e^{-\left(\frac{DT}{b-c\cdot DT}\right)^a}\cdot b\right)$$

$$z2(x) := 0.7\cdot y22(3.1,4.5,0.15,x)$$

$$z2 := x\mapsto 0.7\cdot y22(3.1,4.5,0.15,x)$$

→

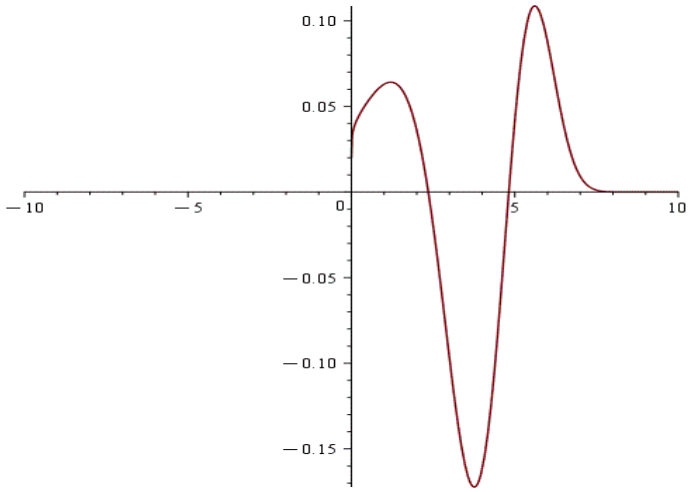

These are the other critical points of our thermogram. We use these together with those from the first derivatives to find a good initial estimate of the parameters, and to keep them within the basic shape of the thermogram data.

Additionally, we have the value of the thermogram function 'y' and its derivatives at each critical point. These extra pieces of information can be used to generate a set of starting values that are at least consistent with the data and the behaviour of the function.

The critical points can be used to differentiate two-event thermograms from three-event ones.

1. Single event: two inflection points and one maximum
2. Two events have four inflection points :
a) separated peaks: Two maxima, one minimum between peaks
b) hump peak: one maximum
3. Three events humps: one maximum and six inflection points

Appendix H: Fitting coefficients and second onset of LLL1, LLL2, LLL3

	LLL1	coeff								LLL2	coeff					
	a_bp	b_bp	b1_bp	a_a	b_a	b1_a	second onset		a_bp	b_bp	b1_bp	a_a	b_a	b1_a	second onset
25	4.2002	6.1895	0.0182	1.8536	4.6903	-0.0211	7.8922	25	4.7412	6.3148	0.0182	1.8001	3.8877	-0.0167	7.7693
25	4.0522	6.0216	0.0182	1.8018	4.1626	-0.0091	7.269	25	4.7229	6.5623	0.0182	1.7343	3.8015	-0.027	7.2518
25	3.9947	5.9445	0.0182	1.7508	4.285	-0.0254	7.2539	25	3.8513	7.9879	-0.0088	1.4897	5.4805	0.0278	9.9393
25	3.4495	5.3169	0.0182	1.7068	4.1977	-0.0186	7.1226	25	4.0825	6.1536	0.0182	1.7609	3.8609	-0.0195	7.0366
25	3.5328	5.4625	0.0182	1.7549	4.285	-0.0153	7.3251	25	4.3268	5.9252	0.0182	1.6977	3.7526	-0.0212	7.2061
25	3.5029	5.5531	0.0182	1.82	4.328	-0.0189	7.2595	25	4.0965	5.6455	0.0182	1.6884	3.6894	-0.0171	7.1335
25	3.583	5.5845	0.0182	1.7489	4.1994	-0.0214	7.0387	25	3.1839	4.6903	0.0182	1.6809	3.9426	-0.0274	7.2561
20	5.0151	7.5051	-0.0157	2.5281	5.6464	0.0278	10.7007	25	3.299	5.0234	0.0182	1.6607	3.8587	-0.0278	6.8686
20	4.6957	7.7597	-0.0107	2.2607	5.5666	0.0278	10.6048	20	4.5661	7.8048	0.0182	1.9285	4.4009	0.0278	10.4363
20	4.2578	7.8466	0.0047	1.7788	4.939	0.0278	10.3012	20	4.3336	8.0967	-0.0056	1.6554	4.7259	0.0278	10.4015
20	4.5943	7.8314	-0.0062	2.0287	5.3653	0.0278	10.4093	20	4.2819	7.9852	-0.007	1.746	4.977	0.0278	10.5084
20	4.6199	7.6191	-0.0026	2.0218	5.407	0.0278	10.4757	20	4.4191	7.5931	-4.73E-04	1.6697	4.732	0.0278	10.3782
20	4.0079	8.0185	0.0046	1.6325	5.4162	0.0103	10.576	20	4.9008	6.1182	0.0182	1.8558	3.0832	-0.0084	7.6048
17.5	5.0875	7.35	-0.0144	2.5058	5.3682	0.0278	10.8205	20	4.1179	7.346	-0.0071	1.5957	4.8129	0.0278	10.3017
17.5	4.6278	7.799	-0.0173	2.1259	5.4613	0.0278	10.8568	20	4.7565	5.9694	0.0182	1.7439	3.0605	-0.0172	7.4512
17.5	4.4572	7.4534	-0.0077	1.9584	5.1118	0.0278	10.6307	20	4.404	5.504	0.0182	1.7323	3.1097	-0.0176	7.4855
15	3.429	9.0259	-0.0182	2.9703	2.9665	0.0266	10.7082	17.5	4.6205	6.1178	-0.0163	2.4481	4.5096	0.0278	10.8456
15	3.4746	9.011	-0.0182	2.9968	2.9581	0.0278	10.7193	17.5	4.9907	8.072	-0.0182	1.8888	4.0225	0.0126	9.9506
15	3.4294	8.8411	-0.0064	3.0747	3.2234	0.0278	10.8045	17.5	4.8001	8.2895	-0.0156	1.8739	4.0855	0.0278	10.275
15	3.5052	9.1609	-0.0101	2.9141	3.3578	0.0278	10.9218	17.5	4.2509	8.2109	2.06E-04	1.9889	4.3192	0.0278	10.4704
15	5.3748	7.5028	-0.0041	2.5191	4.4794	0.0278	10.5852	17.5	4.5341	8.4902	-0.0182	1.8746	4.5049	0.0274	10.4103
15	5.1383	7.5212	-0.0182	2.2987	4.646	0.0259	10.656	17.5	4.7458	7.595	0.0182	2.0319	4.2483	0.0278	10.5483
15	4.7239	7.5382	0.0121	2.2942	4.5859	0.0278	10.7495	17.5	4.6984	7.7066	0.0182	2.1019	4.1757	0.0278	10.7579
15	4.9021	7.7797	-0.0177	2.3598	4.3197	0.0278	10.366	17.5	4.3685	7.4583	-0.0091	1.5843	4.473	0.0278	10.5579
12.5	3.5421	8.2384	-0.0023	3.6917	3.6754	0.0278	11.8303	17.5	5.1512	6.0826	0.0182	1.765	2.916	-0.0278	7.816
12.5	3.2007	9.1923	-0.0182	3.226	2.7743	0.0278	10.9688	17.5	5.0488	6.5151	0.0182	1.9238	2.8323	0.0054	7.7896
12.5	3.5692	8.9629	-0.0182	3.097	2.8088	0.0278	10.7965	15	3.2053	8.8285	-0.0057	2.9653	3.1617	0.0264	10.8664
12.5	4.2935	8.2199	-0.0182	1.5958	3.0346	0.0264	9.4578	15	3.6529	8.8529	0.0079	2.6999	2.8869	0.0278	10.6518
12.5	4.6092	7.8576	-0.0182	1.7899	3.2597	0.0278	10.0612	15	4.6261	8.3639	-0.0182	1.9825	4.1247	0.0072	10.3432
12.5	5.0321	8.0979	-0.0182	1.4541	3.7418	0.0278	9.4694	15	4.7397	7.9699	-0.0112	1.8048	4.1714	0.0278	10.7136
12.5	4.8461	7.7715	-0.0182	1.9637	3.4288	0.0278	10.0373	15	4.7096	7.5568	-0.0132	1.7515	4.2519	0.0278	10.6812
10	4.7434	5.4824	-0.0182	2.939	4.0005	0.0096	13.0481	15	4.8452	7.9759	0.0182	1.5924	6.1589	-0.0278	10.6018
10	3.0253	7.2124	0.0182	3.1668	4.7491	-0.0267	13.6174	12.5	3.3864	8.7711	-0.0182	3.1436	2.7335	0.0278	11.1912
10	2.7959	7.5401	0.0113	3.6459	4.4535	-0.0102	13.231	12.5	3.5103	8.9371	-0.0182	3.2914	3.2332	0.0278	11.2936
10	2.6128	7.7712	-0.0099	3.529	4.0264	0.018	12.7811	12.5	4.9668	7.4771	0.0044	2.3578	4.1333	0.0278	10.9855
10	3.7977	6.8103	-0.0182	2.2803	3.282	0.0084	11.5723	12.5	5.0225	7.6507	-0.0178	2.103	4.3465	0.0278	10.881
10	2.892	7.7023	0.0182	5.9343	7.8401	-0.02	15.7955	10	3.1389	6.9107	-0.0182	2.3887	4.1582	0.0231	13.5014
10	3.0465	7.4893	0.0182	4.4727	5.5587	-0.0224	13.9001	10	2.7836	7.6459	0.0085	5.7886	7.3369	-0.0105	16.2128
7.5	2.9182	6.1926	0.0182	2.6464	4.2981	-0.0276	14.0606	10	3.3115	7.5705	0.0142	5.25	6.9982	-0.0278	15.0731
7.5	2.6114	6.7961	-2.80E-03	3.1689	3.745	0.0278	13.8297	7.5	4.6149	5.5639	0.0127	2.9509	3.8375	0.0278	14.6905
7.5	3.5855	6.2598	-0.0182	2.4916	3.2023	0.019	12.9647	7.5	3.354	6.7233	0.0084	2.8232	4.255	-0.0278	13.6873
7.5	3.5067	6.2014	0.0134	2.7765	4.1509	-0.0278	13.4488	5	4.8542	7.1247	-0.0182	1.1314	3.4336	-0.0107	17.9979
7.5	3.1448	6.7224	0.0146	3.8297	4.9497	-0.0278	13.8692	5	2.5622	5.6447	-0.0075	2.3817	2.6038	0.0278	15.0569
7.5	3.1006	6.455	0.0134	3.6645	4.938	-0.0278	13.8919	5	4.5734	7.285	-0.0182	1.1838	3.5315	-0.0067	17.9965
5	3.366	5.2181	-0.0182	1.9525	2.6886	0.0278	15.2836	5	4.6167	7.9396	-0.0182	1.5836	3.2568	0.0213	18.4539
5	2.6786	5.7945	-0.0115	2.2646	2.7798	0.0278	14.969	5	2.6703	6.68	0.0182	4.0642	5.2522	-0.0146	18.4333
5	2.7366	5.8991	-0.0116	2.2679	2.7044	0.0278	14.675	5	5.1176	8.3726	9.87E-04	1.7303	3.3749	-0.0278	18.53
5	3.0646	5.7866	-0.0121	2.3599	2.9528	0.0278	14.0832	5	2.8723	5.5702	-0.0086	2.3132	3.4196	0.0278	14.7875
5	3.5003	5.8495	0.0163	2.4852	3.6003	-0.0278	14.0652	5	3.0541	5.7037	-0.0116	2.1451	3.116	0.0278	14.6557
5	3.2116	5.8924	-0.0167	2.2111	2.5459	0.0278	14.21	2.5	2.9478	4.1877	-0.0176	2.3587	1.8396	0.0278	16.9722
5	3.4062	6.2025	-0.0142	2.2898	2.6198	0.0278	14.1662	2.5	3.1271	4.4719	-0.018	2.6199	2.2953	0.0278	16.834
2.5	2.827	4.4777	-0.0071	2.483	1.9668	0.0278	16.6006	2.5	3.2632	4.5822	-0.016	2.7082	1.9958	0.0278	16.7037
2.5	4.8503	6.4987	-0.0144	2.08	1.8044	-0.026	19.1695	2.5	5.0277	6.6618	-0.0103	2.5934	2.4943	-0.0278	19.3522
2.5	4.3326	6.4344	-0.0139	1.8685	1.7207	-0.0278	19.1665	2.5	3.4436	4.7262	-0.0177	2.342	2.0196	0.0278	16.1342

		LLL3	coeff				
	a_bp	b_bp	b1_bp	a_a	b_a	b1_a	second onset
25	3.4128	4.3239	-0.0182	1.7525	3.3967	0.02	7.5945
25	3.5861	4.4419	-0.0182	1.7403	3.3978	0.0138	7.6778
25	4.1885	5.0558	-0.0182	1.6931	3.2115	0.0263	7.5072
25	3.9509	4.6736	-0.0182	1.6515	3.2314	0.0173	7.4996
25	3.8332	4.7181	-0.0182	1.7548	3.3926	0.0146	7.7743
25	3.7031	4.4353	-0.0182	1.7278	3.2577	0.0239	7.7162
20	4.8362	6.308	-0.0115	1.8166	2.8379	0.0278	7.5079
20	4.4951	5.6976	-0.0064	1.8122	2.8381	0.0278	7.6304
20	5.198	6.2218	0.0107	1.8175	2.7105	0.0278	7.6761
20	4.8024	5.9814	-0.0072	1.8271	2.8261	0.0278	7.7734
20	4.6772	5.8056	0.0182	1.7428	3.0421	-0.0148	7.5907
20	4.6429	5.8686	-0.0086	1.8462	2.8675	0.0278	7.7017
20	4.8995	5.9982	-0.0052	1.8093	2.7667	0.0278	7.7883
17.5	5.8515	6.4565	0.0161	1.9173	2.4853	0.0278	7.9849
17.5	5.4381	6.1371	0.0064	1.8986	2.5177	0.0278	7.9205
17.5	5.2022	6.3145	-0.0182	1.7417	2.5997	0.0265	7.8526
17.5	5.8399	9.6813	0.0182	1.4048	3.3566	0.0278	10.3818
17.5	5.4639	5.7713	0.0182	2.124	2.3085	0.0278	8.1502
17.5	5.4388	6.1577	0.0065	1.9044	2.5149	0.0278	8.0344
17.5	5.6802	6.542	-0.0093	1.8195	2.4706	0.0278	7.9229
17.5	5.7124	6.2016	0.0182	1.934	2.523	0.0278	8.0264
15	5.2695	8.0214	0.0018	1.2947	4.4279	0.0278	10.4332
15	4.8207	7.7347	0.0058	1.2844	3.9793	0.0278	10.382
15	5.0061	7.8479	-0.0108	1.3911	3.7633	0.0278	10.4238
15	4.9103	7.7865	0.0028	1.3531	3.7666	0.0278	10.4523
15	5.0776	8.3108	-0.014	1.3862	3.643	0.0278	10.4991
15	4.8217	7.7662	0.0085	1.2277	4.8997	0.0278	10.3894
12.5	4.6703	8.6796	-0.0182	2.3948	2.492	-0.004	10.8137
12.5	4.9796	8.0693	-8.61E-04	1.3	4.2112	0.0278	10.291
12.5	5.3537	8.087	-0.0084	1.3645	3.8367	0.0278	10.3064
12.5	5.2437	8.1674	-0.0179	1.3133	3.1365	0.0278	10.3525
10	3.8492	9.4323	-0.0182	2.7518	2.702	0.0029	11.0682
10	3.5659	8.8497	-0.0182	2.7771	2.6213	0.0226	11.1657
10	3.5146	8.4475	-0.0182	2.4102	2.5519	0.02	10.9429
10	3.5402	8.5284	-0.0182	2.4495	2.581	0.0212	10.9836
10	3.665	8.5336	-0.0182	2.6046	2.7309	0.0142	11.2327
7.5	3.2323	8.5114	-0.0182	3.5042	2.9512	0.0278	12.0073
7.5	3.2445	8.1725	-0.0182	4.4473	3.8409	0.0259	12.8755
7.5	3.1985	8.0966	-0.0182	4.1014	3.6481	0.0278	12.6475
7.5	3.5029	8.3192	0.0148	3.3358	3.2227	-0.0278	12.0321
7.5	4.2231	5.6618	-0.0182	2.7096	2.334	0.0109	11.0479
7.5	4.6752	7.5705	-0.0182	2.1003	2.2854	-0.0278	10.7018
7.5	3.2458	7.92	-0.0136	7.2152	7.0434	0.0106	16.3963
5	2.9683	6.7517	0.0139	7.5585	7.6552	-0.0278	17.5318
5	3.0831	6.7833	0.0101	7.9908	7.9983	-0.0278	17.7941
5	2.9284	6.4321	-0.004	4.4521	4.8401	-0.0278	14.6987
5	4.1787	6.5679	-0.0148	6.2078	7.6678	-0.0278	17.5951
5	3.0818	6.3966	-0.0027	2.8428	4.3	-0.0278	14.6286
2.5	3.14	4.8145	-0.0117	2.7197	2.8579	0.0278	15.7816
2.5	2.943	4.7012	-0.0097	2.3584	2.8387	0.0278	15.8926
2.5	3.1601	5.0194	-0.0126	2.5327	2.7325	0.0278	15.8048
2.5	3.8788	6.9748	-0.0084	1.9739	2.3259	-0.0278	19.0257
2.5	3.1737	4.8055	-0.0156	2.4491	2.3646	0.0278	15.7909
2.5	3.4153	5.168	-0.0159	2.2725	2.9978	0.0278	16.6107